SHEAR-BAND STRUCTURE IN METALLIC GLASSES

BY

CHAOYANG LIU

DISSERTATION

Submitted in partial fulfillment of the requirements
for the degree of Doctor of Philosophy in Materials Science and Engineering
in the Graduate College of the
University of Illinois at Urbana-Champaign, 2020

Urbana, Illinois

Doctoral Committee:

Assistant Professor Robert Maass, Chair and Director of Research
Professor Jian-Min Zuo
Professor Pascal Bellon
Professor Moonsub Shim

ABSTRACT

Metallic glasses (MGs) are amorphous alloys that possess exceptional mechanical properties compared to their crystalline counterparts. The fundamental problem that currently prevents the use of MGs as reliable structural materials is the lack of understanding of how their structure evolves as a function of macroscopic strain. At low homologous temperatures (e.g., operating temperatures of common structural materials), strain localization into shear bands make these defects play a decisive role in controlling the plastic behavior of MGs. However, the characterization of shear bands has not yet succeeded in connecting their structural evolution and damage accumulation with any macroscopic engineering strain or local shear strain parameters. This dissertation work aims to understand such connection by studying the structure of shear bands in Zr-based MGs from the nano-scale shear-band core to the micro-scale shear-band region.

First, the nano-scale structural properties, such as morphology, thickness, and density variation, of a single system-spanning shear band that has carried all plastic flow were sampled along its millimeter-length path with high-angle annular dark field scanning transmission electron microscopy (HAADF-STEM). It was found that those properties sensitively depend on the position along the shear band, offering a more complex view of shear-band structure than the commonly considered simple nano-scale planar defect.

Next, the origin of the nano-scale structural change was evaluated by correlative analytical methods, including TEM-based energy dispersive X-ray spectroscopy (EDX) and scanning electron nano-beam diffraction (SEND), as well as synchrotron-based nano-beam X-ray fluorescence (NB-XRF) and atom probe tomography (APT). These methods not only confirmed the validity of using the HAADF-STEM technique to quantify the shear-band density difference

with respect to the matrix material, but also unambiguously revealed the structural and compositional changes in the nano-scale shear-band core of the Zr-based MG alloys studied here.

Then the evidence of structural damage in shear bands was investigated as a function of shear strain. To this end, a large number of shear bands were extracted from bulk samples and analyzed with HAADF-STEM, revealing a general positive correlation between shear-band volume dilatation and shear strain. The structural dependency on shear strain suggested that the shear-driven disordering in shear bands dominated over thermally-activated relaxation during plastic flow at low homologous temperatures over the probed shear-strain regime.

Finally, extending studies beyond the nano-scale shear-band core on MG samples unloaded prior to fracture using synchrotron-based X-ray tomography (XRT) yielded the reconstruction of large amounts of micron-size cavities (internal micro-cracks) in the micro-scale shear-band region. The shear-band cavities significantly reduced the true load-bearing area, leading to an apparent strain hardening phenomenon in those samples. We proposed that the formation of internal shear-band cavities proceeded gradually during plastic straining, which questioned the meaningfulness of stress determinations that were solely based on externally measured dimensions of MG samples.

Overall, the experimental findings in this dissertation work are at the forefront of MG research and have expanded our knowledge on the structure of shear bands, which agree well with recent advances in molecular dynamics simulations work that strongly suggest the existence of structural heterogeneities in MG shear bands. The evolution of shear-band structure was proven here to have a strain dependency. Future work may include in-situ observations of such structural evolutions, and the challenge remains at linking the damage accumulation mechanism across different length scales both experimentally and theoretically.

ACKNOWLEDGEMENTS

I am very thankful to my PhD thesis advisor, Prof. Robert Maass, for his consistent guidance and support since I joined the Maass Research Group as a graduate student in 2015. I would not have learned and grown so much as a student, a researcher, and a colleague without his advice and encouragement over the past five years. I did not have any background knowledge about metallic glasses nor any transmission electron microscopy experience prior to joining his group, so it took me quite a lot of time to get started and learn everything from scratch. At times when there were unavoidable instrumental issues and time management problems that caused frustration, he has always given me constructive and optimistic feedback that helped me pull through struggles.

I would like to thank Prof. Jian-Min Zuo, Prof. Pascal Bellon, and Prof. Moonsub Shim for their valuable service on my doctoral committee. I would also like to thank Prof. Jian Ku Shang, Prof. Zuo, and Prof. Shim for their advice and discussions during my preliminary exam. Additionally, I thank Prof. Zuo, Prof. Pinshane Huang, Prof. Shang, and Prof. Bellon for serving as examiners on my qualifying exams. The questions and discussions during all the exams guided me to think more deeply about the background knowledge, experimental techniques, and my research results, thus building a solid foundation and more confidence for me to take on other scientific or engineering projects.

I appreciate the fun times spent together with my fellow colleagues, Dr. Stefan Kuechemann, Dr. Gregory Sparks, Amlan Das, Quentin Rizzardi, and Yuki Ikeda, and the fruitful discussions with them. They have always been supportive with their brilliant minds. I also appreciate the assistance from Scott Larson, Wuwen Wang, Xinbo Xia, Zan Hitchens, and Jeremy Shin on various projects, from experimental work to data analysis.

Special thanks must be paid to the dedicated staff scientists at the Materials Research Laboratories, especially to Dr. Chenchang Qiang, Dr. Honghui Zhou, and Dr. Jim Mabon, for teaching me how to operate the expensive and complicated instruments that generated the samples and results for my thesis.

I am very grateful to my research collaborators, Dr. Vladimir Rodattis (University of Goettingen), Dr. Zhonghou Cai (Argonne National Lab), Dr. Peter Kenesei (Argonne National Lab), Dr. Jon Poplawsky (Oak Ridge National Lab), Dr. Wei Guo (Oak Ridge National Lab), James Burns (Oak Ridge National Lab), Dr. Yimeng Chen (CAMECA), Prof. Peter Derlet (Paul Scherrer Institute), and Renliang Yuan (Prof. Zuo's group) for their generous experimental assistance and resourceful discussions.

I enjoyed working with Prof. Maass, Dr. Jessica Terbush, Dr. Joseph Flanagan, and Nicole Robards, and I must thank them for making my teaching assistantship experience fun and memorable. I also appreciate the support from Prof. Maass, Prof. Cecilia Leal, Prof. Renske Van der Veen, Carol Lin, and Jill Carbone during the Mid-GLAM camps, in which my interest to study Materials Science was always refreshed.

I am also grateful that the University of Illinois at Urbana-Champaign has provided excellent resources and facilities that made my graduate school experience enjoyable and well-balanced. I have made great friends here who constantly inspired me.

Last but certainly not least, I would like to thank my parents, Ying Liao and Daojing Liu, for their love and care throughout the years.

TABLE OF CONTENTS

LIST OF ABBREVIATIONS vii

CHAPTER 1: INTRODUCTION 1
1.1 Mechanical behavior of metallic glasses 1
1.2 Shear bands in metallic glasses 22
1.3 Research objectives 32

CHAPTER 2: EXPERIMENTAL METHODS 35
2.1 Metallic glass sample preparation 35
2.2 Transmission electron microscopy techniques 48
2.3 Synchrotron-based X-ray techniques 62
2.4 Atom probe tomography 67

CHAPTER 3: RESULTS AND DISCUSSION 70
3.1 Nano-scale shear-band morphology, thickness and density change 70
3.2 Chemical segregation and volume dilatation of shear bands 81
3.3 Shear-strain-dependent nano-scale shear-band structure 99
3.4 Micro-scale shear-band cavities and apparent strain hardening 108

CHAPTER 4: CONCLUSIONS 133

PUBLICATIONS 138

REFERENCES 139

APPENDIX A: CALCULATION OF CONTRAST THICKNESS 152

APPENDIX B: EXAMPLE HAADF-STEM IMAGE ANALYSIS CODE 153

APPENDIX C: UNUSED X-RAY TRANSMISSION AND DIFFRACTION DATA 157

LIST OF ABBREVIATIONS

ADF-STEM	Annular dark field scanning transmission electron microscopy
AE	Acoustic emission
APS	Advanced Photon Source at Argonne National Laboratory
APT	Atom probe tomography
BMG	Bulk metallic glass
EDM	Electrical discharge machining
EDX / EDS	Electron dispersive X-ray spectroscopy
FIB	Focused ion beam
FWHM	Full width at half maximum
GFA	Glass-forming ability
HAADF-STEM	High-angle annular dark field scanning transmission electron microscopy
MG	Metallic glass
MRO	Medium-range order
NB-XRF	Nano-beam X-ray fluorescence
ORNL	Oak Ridge National Laboratory
SEND	Scanning electron nano-beam diffraction
SRO	Short-range order
STEM	Scanning transmission electron microscopy
STZ	Shear-transformation zone
TEM	Transmission electron microscopy
XRD	X-ray diffraction
XRT	X-ray tomography

CHAPTER 1: INTRODUCTION

This chapter addresses the background, the proposed hypothesis, and the research objectives for this thesis work conducted to study shear-band structure in metallic glasses.

1.1 Mechanical behavior of metallic glasses

A new class of metals with amorphous structure was introduced around the 1960s predominantly by the work of Klement et al. [1]. The tightly packed glassy structure of these metals have granted them the name "metallic glasses" (MGs). Unlike conventional crystalline metals, the lack of long-range atomic order in MGs causes the absence of crystal defects and gives MGs different mechanical, chemical, and electrical properties compared to their crystalline counterparts [2-4]. The valuable properties have initiated growing development for real-world applications using MGs [5, 6]. Notably, high-temperature and high-pressure injection molding is currently being applied to produce MG parts with complex shapes [7], which are difficult to make with conventional crystalline alloys that also do not possess the desired properties existent in MGs. However, MGs are not yet widely used as structural materials due to their limited ductility and the lack of understanding of how their structure evolves towards failure as a function of macroscopic strain. This section briefly introduces the structure of MGs and summarizes the general macroscopic mechanical properties of MGs.

1.1.1 Formation and structure of metallic glasses

Due to the high cooling rate required during the formation of MGs, which does not leave enough time for crystallization, atoms are slightly less efficiently packed in MGs compared to crystals of the same composition. Consequently, MGs are usually found to be less dense than their

crystalline counterparts (~ 2-3% less dense [8, 9]). Starting from the elastic regime and moving on to yielding, plastic regime, and fracture in the following subsections, the differences in mechanical properties between MGs and crystals can be attributed to the discrepancies in their atomic structure. It is thus instructive to provide a condensed overview of the disordered atomic structure of MGs in this subsection, as well as the processing route that leads to the resulting glassy structure.

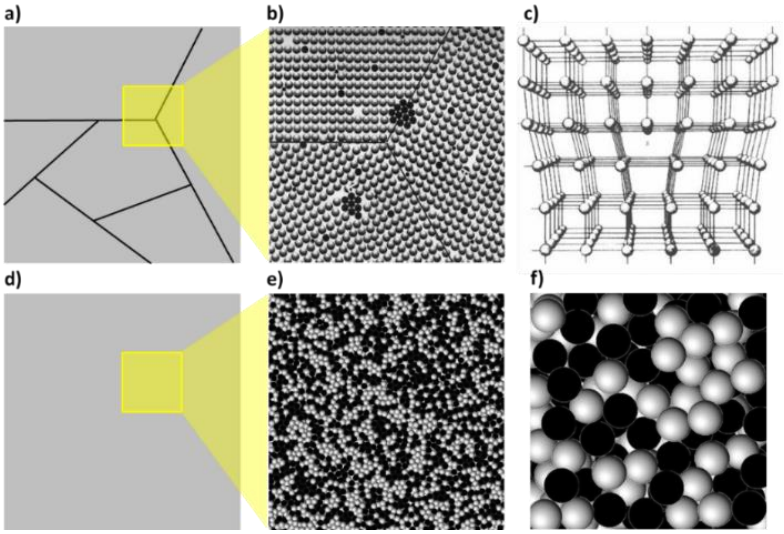

Figure 1.1. a)-c) Schematics of structural features in a traditional polycrystalline metal from the micro-scale to the atomic-scale, where a) is the most zoom-out view that only show grain boundaries, b) reveals various crystal defects in a zoom-in view, and c) is a typical 3D representation of a dislocation. d)-e) Schematics of MG structure on different length scales, where a) shows the homogenous continuum at or above the micro-scale, b) shows the disordered atomic structure that may include fluctuations that are different from those at the atomic-scale in c).

In crystalline metals, atoms have long-range periodic order, and the disruption of this order introduces crystal defects, such as vacancies, substitute and interstitial atoms, grain boundaries, and, most importantly, dislocations. The structural features of a typical polycrystalline metal in various magnifications is illustrated in Figures 1.1a-c, from the micro-scale to the atomic-scale. In crystals, plastic flow is well explained by dislocation theory [10], which describes the movement and interaction of dislocations, as well as their interactions with other crystal defects. Hence, the structural evolution that ultimately leads to failure of crystals as a function of macroscopic plastic strain can be visualized and predicted. On the contrary, defects are not defined in an amorphous

body since they do not stand out as disruptive features, at least in the microscopic view. As seen in the schematic representation in Figure 1.1d, on the micro-scale level, the structural heterogeneities in MGs are well averaged and considered as a continuum. However, below certain length scales, structural fluctuations (Figures 1.1e-f) [11] and short-range to medium-range atomic order are present in MGs [12], and they may play important roles in controlling the structure-property relationship in MGs.

To produce MGs, a race against thermodynamics must be won. One of the most commonly known first MGs was produced in 1960 by rapidly quenching a Au-Si alloy at a high cooling rate of ~10^6 K/s , and such high cooling rate was due to the low glass-forming ability (GFA) of the alloy, which restricted the thickness of the sample to the micrometer range [1]. Later in the decade, Chen and Turnbull developed Pd-based MGs with the smallest dimension of at least 1 mm, which were the first "bulk metallic glasses" (BMGs) [13]. Turnbull also developed an important empirical rule known as the Turnbull's criterion for determining the GFA [13], which is still used today to develop new MG alloys. It states that a metallic liquid with $T_g/T_m \geq 2/3$ can only crystallize within a very narrow temperature range and can thus easily bypass crystallization and be undercooled at a low cooling rate into a glassy state, where T_g and T_m stand for the glass transition temperature and the melting temperature, respectively. A list of density (ρ) and T_g values for representative MGs of various base elements can be found in Table 1.1. All samples used in this thesis work are millimeter-size and are called MGs for simplicity. Starting from the 1980s, Inoue and coworkers made a variety of MG alloys with cooling rates less than 100 K/s and reached the centimeter-scale in MG production. Three empirical rules were established by Inoue in the 1990s for the production of millimeter- to centimeter-size MGs: i) the alloy system should consist of three or more elements, ii) the difference in atomic sizes of the main constituent elements should

be greater than ~12%, and iii) the elements should have negative heat of mixing [14-16]. The lowest reported cooling rate for MG formation was ~0.10 K/s for the $Pd_{40}Cu_{30}Ni_{10}P_{20}$ alloy with maximum sample thickness of 10 cm [17].

To illustrate the route for glass formation, a state vs. temperature diagram, like the one shown in Figure 1.2, is widely used. Depending on the cooling rate of an alloy system, one either forms a crystal through a liquid-solid phase transition near the melting temperature (T_m), or, with high cooling rate, the liquid undercools and transitions at a quench-rate-dependent fictive temperature (T_f) into a glass [18], as shown in Figure 1.2. It should be noted that although T_f has been widely used in the literature to define different glassy states for MGs as well as polymers and metal oxides [19, 20], it is a measure that does not include any structural relaxation that can occur prior to reaching the glass transition temperature, T_g, during heating. Hence, T_g is the experimentally more accessible definition when one refers to a structural state that has a thermomechanical history, which is introduced after quenching and thereby offsets the structure from a quenched-only state represented by T_f.

Table 1.1. Density and glass transition temperature values for several MGs.

	$Zr_{55}Ti_5Cu_{20}Ni_{10}Al_{10}$	$Pd_{40}Cu_{30}Ni_{10}P_{20}$	$Ni_{45}Ti_{20}Zr_{25}Al_{10}$	$Cu_{46}Zr_{42}Al_7Y_5$	$Pt_{60}Ni_{15}P_{25}$
ρ (g/cm^3)	6.62	9.28	6.4	7.23	15.7
T_g (K)	620	593	791	713	488
Reference	[21]	[22]	[23]	[24]	[25]

The rejuvenation and relaxation of MGs are also labeled in Figure 1.2, which are determined by the stored enthalpy in the system resulting from its processing history. Due to the non-equilibrium (metastable) energy state of MGs, annealing or aging can also lead to structural

relaxation apart from using a slower cooling rate. Their effect on some macroscopic mechanical properties, such as hardness (H), Young's modulus (E), yield strength (σ_y), and plane strain fracture toughness (K_{IC}) are indicated schematically in Figure 1.6.

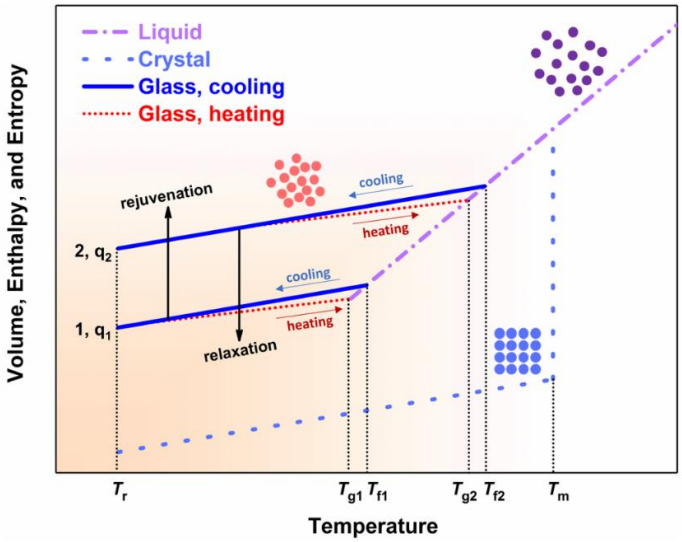

Figure 1.2. Schematic representation of a state variable (volume, enthalpy, and entropy) as a function of temperature for two glass-forming liquids (1 and 2) quenched at different rates (q_1 and q_2, $q_2 > q_1$), and for the corresponding crystal-forming liquid that undergoes a liquid-solid phase transition at T_m. Depending on the quench rate, T_f, which describes the structural state upon freezing, varies. In experiments, stored enthalpy is generally measured during heating, resulting in a relaxation signature prior to reaching T_g, which is also rate dependent. Since the cooling curves are parallel below T_f, different final states are obtained at room temperature, T_r.

Although MGs do not possess long-range structural order as in crystals, short-range order (SRO) and medium-range order (MRO) are present in these amorphous alloys, where SRO refers to nearest-neighbor shells below ~0.5 nm and MRO refers to a length scale beyond the average interatomic spacing in MGs up to 1-2 nm [12, 26]. Since MGs are only a few percent less dense than their crystalline counterparts [8, 9], which means that the atoms are still densely packed with rather high packing efficiency (just not as high as fcc or hcp lattice structures in crystalline metals), the local atomic arrangements in MGs cannot be completely random. The hard-sphere model proposed by Bernal in the 1940s stated that the basic packing unit in metallic liquids is a tetrahedral cluster of four atoms [27], but it is impossible to fill space with tetrahedra so geometrical

frustration is required. Such geometrical frustration is shown from simulations in different structural motifs, or preferred ways of packing tetrahedra, which are often termed "Z clusters" [12]. Variations in structural motifs can be achieved because metallic atoms are not hard spheres and the non-directional metallic bonding via delocalized electrons provide significant flexibility for the local arrangement (coordination) of atoms. A popular motif in MGs is the "icosahedron", in which 12 atoms are coordinated around a central atom, as shown in Figure 1.3a, which is a Cu-centered full icosahedral cluster from molecular dynamics simulation of a $Cu_{64}Zr_{36}$ binary MG system [28]. Another structural motif is shown in Figure 1.3b, which shows a Zr-centered cluster that can accommodate 16 near-neighbors [28]. Figure 1.3c shows eight interconnected or interpenetrating Cu-centered icosahedra that share vertices, edges, and faces [28]. It has also been proven through simulations that the addition of Al into the Cu-Zr system increases the number of icosahedral clusters, which enhances the glass-forming ability (GFA) of the alloy by slowing down the dynamics of atomic movement [29]. The works by Ma and coworkers suggest that an enhanced icosahedral order leads locally to higher stiffness and resistance to yield, while the geometrically unfavorable motifs, which are the less-efficient spacing-filling clusters that form due to fast cooling, have lower stiffness and higher tendency to undergo shear transformations [28, 30] that lead to local structural rearrangements. Such geometrically unfavored structural regions in MGs are also termed as soft spots [28]. Figure 1.4 shows a cross-sectional view of a binary MG system from molecular dynamics simulations with soft spots made of geometrically unfavored motifs that easily undergo local structural rearrangement under shear (shear transformation) and the icosahedron-rich regions that remain stiff during deformation [30]. Annealing that relaxes the system can also enhance the icosahedral order in a MG [31] and therefore change its mechanical properties, as indicated in Figure 1.6.

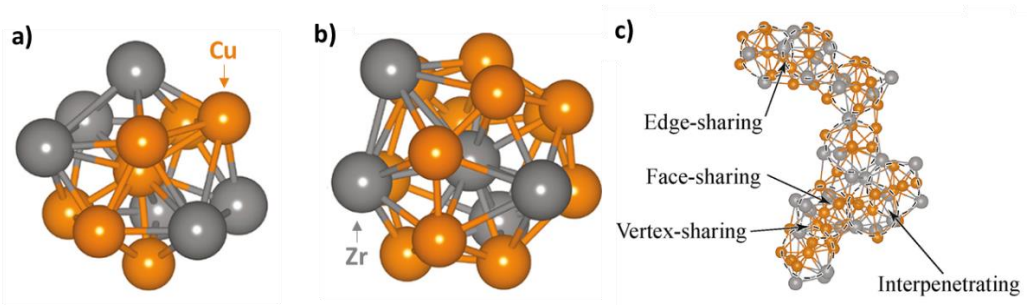

Figure 1.3. a) A full icosahedron, in which 12 atoms are centered around a Cu atom (Z12 in the Z-cluster notation). b) A Zr-centered cluster, in which the central Zr atom is accommodated by 16 near-neighbor atoms (Z16 in the Z-cluster notation). c) Eight interconnected or interpenetrating Cu-centered icosahedra that share vertices, edges, and faces [28].

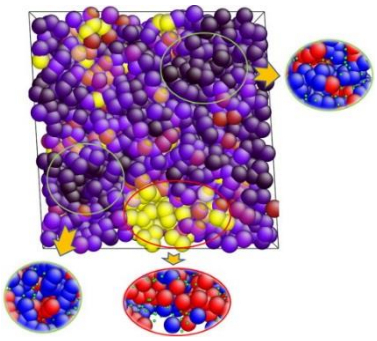

Figure 1.4. Cross-section of a sheared $Cu_{64}Zr_{36}$ MG. Only Cu atoms are shown. The dark purple regions are only elastically deformed while the yellow ones have been involved in shear transformations. Two elastic regions and one shear-transformation region are circled out with their local structures shown in the insets. For the elastic regions, full icosahedra (blue) are dominant, while in the shear-transformation region, more Cu atoms are embedded in low population polyhedra (red). To highlight full icosahedra and the low-population polyhedra, the neutral atoms (those embedded in the other types of polyhedra, are shown with much smaller green dots [30].

The next structural level beyond the nearest-neighbor SRO in MGs is the MRO. The efficient cluster packing model developed by Miracle [32, 33] states that the SRO clusters are arranged in bigger arrays that exhibit MRO to efficiently pack the overall space of the alloy system. As a result, structural heterogeneities may exist over larger length scales in MGs and locally induce fluctuations in mechanical properties. Recent experimental efforts have indeed provided evidence for such structural hierarchy beyond the SRO length scale [34] and even beyond the MRO length scale [11], covering length scales over four orders of magnitude in as-cast MGs, from a few nanometers [35, 36], tens of nanometers [37, 38], hundred nanometers [39], to tens of micrometers [40]. The spatial heterogeneities covering such a large spectrum of length scales (correlation length)

in MGs were mainly measured as elastic fluctuations, as shown in Figure 1.5 [11], which presents spatially varying elastic properties measured with atomic force acoustic microscopy [37] and nanoindentation [40] on two different glassy alloys. They have recently started to catch attention in the field of MG research to refine the understanding of structure-property relationship for amorphous metals. However, understanding the various hierarchical structures of MGs and their effects on mechanical properties is still very limited compared to the long-established knowledge on structure-property relationship for crystalline metals. A diagram that schematically rationalizes the complex structure-property relationship for MGs is shown in Figure 1.6.

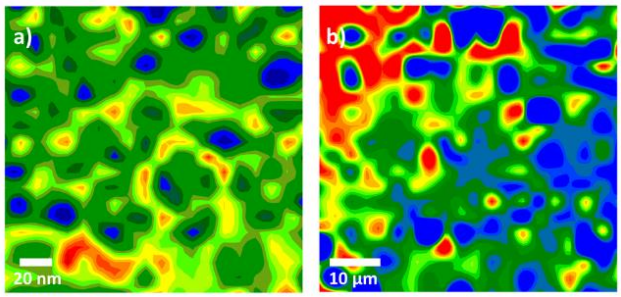

Figure 1.5. Spatially varying elastic properties measured with a) atomic force acoustic microscopy [37] and b) nanoindentation [40] on a) a $Zr_{50}Cu_{40}Al_{10}$ MG and b) a $Pd_{77.5}Cu_6Si_{16.5}$ MG. The color-scale ranges have been normalized, evidencing similar fluctuations at vastly different spatial length scales [11].

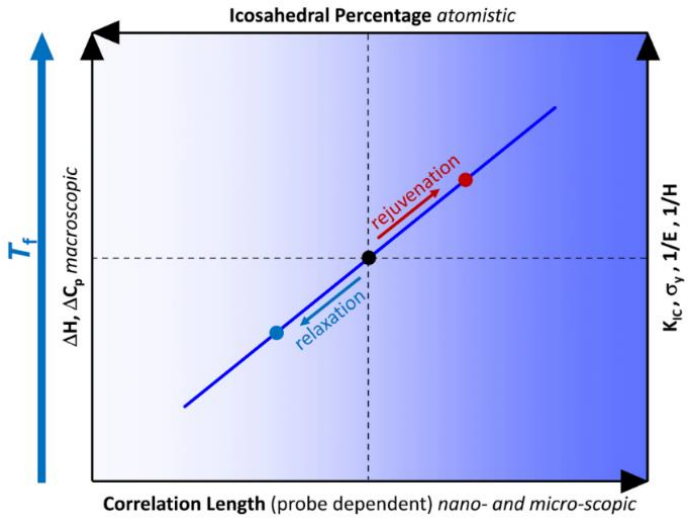

Figure 1.6. Plot that summarizes the current understanding of structure-property relationship in MGs.

1.1.2 Elastic behavior

MGs are usually taken as elastically isotropic on the macroscopic level, and isotropic materials have two independent elastic constants, the Young's modulus (E) and the Poisson's ratio (v). It is also practical to consider the shear modulus (G) and bulk modulus (B), which are dependent on E and v. At low homologous temperatures ($T < 0.6T_g$, which is the temperature range for most structural applications), the B values of MGs are typically ~5-10% smaller than those of crystalline metals with the same composition [41]. This can be explained by the larger atomic spacing in MGs with the assumption that the interatomic cohesive forces are not significantly different between the amorphous and crystalline structures [42]. Interestingly, the E and G values of MGs are ~20-30% lower than those of corresponding crystals [41], which cannot be explained alone by the difference in atomic spacing anymore. In this case, the difference in local atomic environments of MGs and crystals plays an important role [8]. In crystals, the displacement of each atom is directly related to the macroscopic strain. In MGs, the slightly less efficient packing allows extra local atomic displacements (non-affine displacements via anelastic reshuffling of near-neighbor atoms) that makes the elastic deformation of MGs much more complex than crystals [4, 43, 44]. Example elastic constants and the comparison with their crystalline counterparts are listed in Table 1.2 [43], where $\Delta X/X_a = (X_c - X_a)/X_a \times 100$ and the subscripts "a" and "c" stand for amorphous and crystalline, respectively. X can stand for E, v, G, or B.

MGs also have a strain of 2% or more at the elastic limit [43, 45, 46], which is an order of magnitude higher than their crystalline counterparts. The high elastic limit and low stiffness (high compliance) enables high elastic energy storage in MGs, which is proportional to the resilience (σ_y^2/E). Figure 1.7 [3] shows the yield strength (elastic limit) and Young's modulus for a variety of MGs and conventional metals in the bulk size, in which MGs are labeled with their compositions

in atomic percent. It is clear from Figure 1.7 that MGs have higher elastic limit values than conventional metals in general and, following the dashed contours of resilience, MGs have much higher resilience than conventional metals, as well. The elastic properties of MGs have attracted many commercial applications [47], such as springs in mechanical watches [48], pressure sensors in automobile industry [49], and fiber reinforcements in sporting goods like golf clubs [50].

Table 1.2. Comparison of various elastic constants of MG alloys to their crystalline counterparts with the data listed in Reference [43].

	$\Delta E/E_a$ (%)	$\Delta \nu/\nu_a$ (%)	$\Delta G/G_a$ (%)	$\Delta B/B_a$ (%)
$Zr_{53}Ti_5Cu_{20}Ni_{12}Al_{10}$	54	/	48	10.0
$Pd_{39.1}Ni_{10.1}Cu_{20.9}P_{20.9}$	25	-6.0	27.2	2.2
$Cu_{60}Zr_{20}Hf_{10}Ti_{10}$	21.9	-7.0	24.2	2.4
$Ce_{70}Al_{10}Ni_{10}Cu_{10}$	43.5	-9.9	47.0	22.9
$Mg_{65}Cu_{25}Tb_{10}$	20.8	-4.8	22.2	12.3

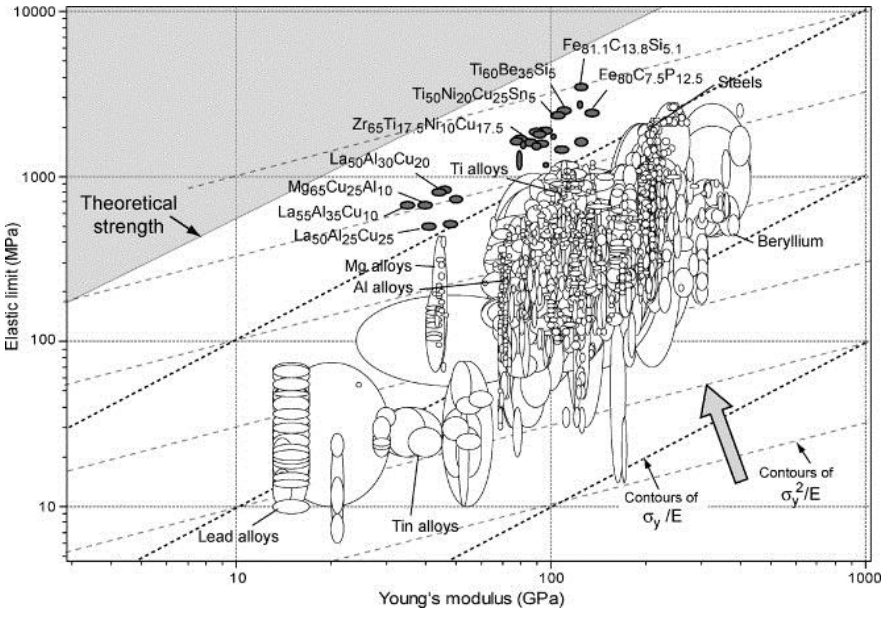

Figure 1.7. Materials-selection map (Ashby plot) reproduced from Reference [3] showing yield strength (σ_y at elastic limit) and Young's modulus (E) of MGs and conventional metals in the bulk size.

1.1.3 Yielding and plastic behavior

Plastic flow in MGs is different in different temperature regimes. The well-known deformation map summarized by Spaepen, as shown in Figure 1.8, shows that close to and above T_g (>0.6T_g [51]), plastic flow in MGs is homogeneous [52]. In this regime, plastic deformation is distributed rather equally in the sample volume. Homogeneous deformation makes thermoplastic forming of complex shapes possible for MGs, and this has been proven useful for manufacturing micro-electromechanical system devices [53, 54] that utilize many advantageous properties of MGs, such as high hardness, high wear resistance, and high corrosion resistance [3]. Homogeneous deformation is beyond the scope of this thesis because it is not applicable to most structural applications, which operate at low homologous temperatures, and more information on this topic can be found in Reference [55].

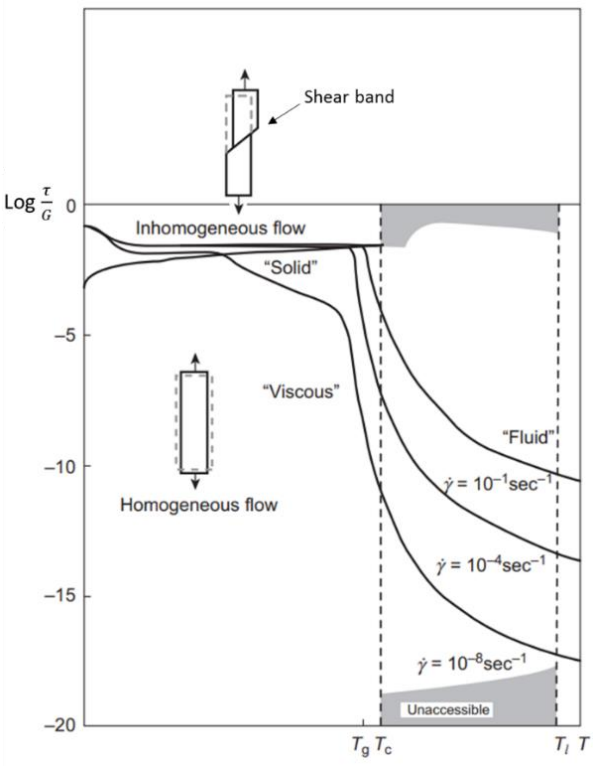

Figure 1.8. Deformation map of MGs reproduced from Reference [52] showing the inhomogeneous flow (low homologous T) and homogenous flow (close to and above T_g) regimes. τ, G, $\dot{\gamma}$, T_c, and T_l stand for shear stress, shear modulus, shear strain rate, crystallization temperature (or T_m), and the liquidus temperature of the alloy, respectively.

At low homologous temperatures (<0.6T_g), the yield strength of a MG is typically one order of magnitude (10-30 times) higher than that of the same alloy in the crystalline state [56]. In crystalline metals, the collective migration of dislocations results in macroscopic plastic strain in crystals. The energy barrier for dislocation migration, or the Peierls energy, is ~10^{-2} eV for cubic close-packed metals [57], which means that dislocation motion is relatively easy with such low barrier energy. In MGs, since lattice defects are not defined, plastic deformation is initiated by a different mechanism and thus requires much more energy to overcome the barrier that resists irreversible structural change.

Two most prominent theoretical models that aimed to describe the plastic behavior of MGs on the atomic level are: i) the free volume theory proposed by Spaepen [52] and ii) the shear-transformation theory proposed by Argon [51]. Spaepen's free volume model uses diffusion-like atomic jumps to nearby sites with available free volume (empty space) to explain the plastic deformation in MGs. It suggests that free volume is created by atomic movements, which, is mainly thermally driven near or above T_g and becomes increasingly stress driven at low homologous temperatures. Atomic jumps to the created free volume are promoted by shear stress. However, it is difficult to rationalize how single atomic jumps can accommodate much plastic strain in MGs, especially at low homologous temperatures. On the other hand, Argon's thermally activated shear-transformation theory pictures the onset of plastic deformation in MGs as cooperative shearing of atomic clusters, instead of single atomic jumps, to enable local relief of shear stress. Later, Falk and Langer [58, 59] proposed an athermal shear-transformation zone (STZ) theory, adding the concept of a localized and pre-existing atomic clusters that are prone to structural rearrangement due to shear, which had broader applicability. It is important to note here that STZs are transient and are not experimentally observable, so they should not be confused with

the nano-scale flow defects, called "shear bands", which are experimentally observable and can carry significant amount of shear strain in MGs. Shear bands are briefly introduced in the following paragraph and in more detail in Section 1.2. The activation energy of shear transformation can start from very low values, enabling reversible and irreversible shear transformations (β-relaxation) to operate in the elastic regime during deformation [60]. Such shear transformations would not lead to observable macroscopic yielding, as long as they are isolated in the elastic matrix. To observe macroscopic yielding and plastic deformation in MGs, much more energy is required to activate percolated shear transformations (α-relaxation, ~10^{-1} eV for ~100 atoms [61], one order of magnitude higher than the Peierls energy for activating dislocation motion in crystals). The high activation energy for collective and irreversible rearrangement of a large number of atoms in MGs may explain the high yield strength of MGs compared to their crystalline counterparts.

Looking back at Spaepen's deformation map for MGs in Figure 1.8, it is intuitive to suggest that the yielding criterion for MGs is thermally activated. Indeed, a well-known temperature-dependent yielding criterion was proposed by Johnson and Samwer in 2005 [45], by which experimentally obtained critical shear stresses of different MGs can be fitted well at low homologous temperatures. They started with the assumption that yielding occurs when the applied shear stress causes a critical density of minimal-energy-barrier STZs to become unstable. Then using a cooperative shear model inspired by Frenkel's calculation of theoretical shear strength in crystals [62] and a temperature-dependent scaling analysis, the expression for yielding in MGs has been derived as a function of $\left(T/T_g\right)^{2/3}$. However, this model does not address the strain-rate dependency for yielding. To eliminate the strain-rate effect, another thermal activation model proposed by Derlet and Maass in 2013 [63] successfully illustrated the macroscopic yielding of MGs linking the low homologous temperature and high homologous temperature regimes. It uses

the assumption that plasticity occurs via the thermal activation of α-relaxation processes (percolated STZs) mediated by multiple thermally activated STZ activities. As shown in Figure 1.9, where model curve fits well with the experimental data for various temperatures with an elimination of the strain-rate effect in the experimental data, at high homologous temperature, the shear stress at which pronounced plasticity occurs rises rapidly from zero, indicating a drop in both the barrier energy to structural change and the number of structural transformations. As temperature lowers, the number of structural transformations saturates due to the eventual kinetic freezing, and the transition from elastic to plastic deformation is abrupt with respect to the applied stress, pointing to a single dominant energy barrier for structural change.

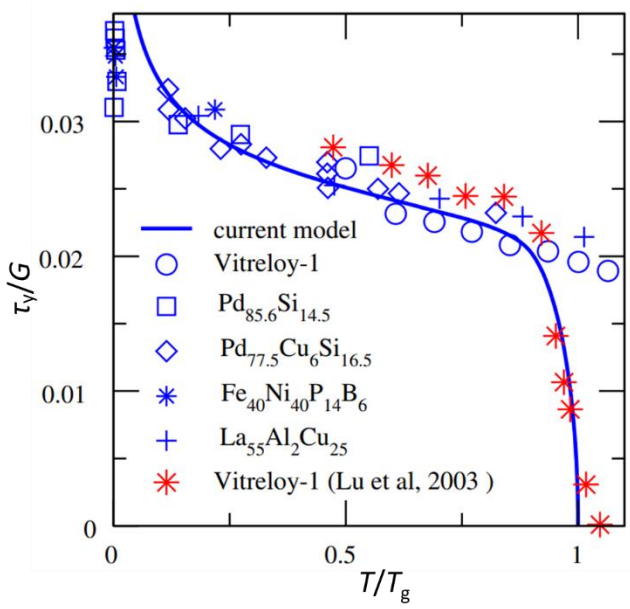

Figure 1.9. Plot reproduced from Reference [63] showing shear strength (τ_y) over shear modulus (G) as a function of homologous temperature for experimental data (blue and red scattered data) and the fit (smooth blue curve) using the thermal activation model proposed by Derlet and Maass [63]. The red Vitreloy-1 data [64] were collected using the same strain rate, eliminating the strain rate effect, and the other experimental data were taken using various strain rates [45].

Immediately after yielding, a macroscopically observable permanent deformation is caused by the initiation of one or more shear bands depending on the deformation mode and sample

geometry [65]. Shear bands are nano-scale flow defects that can carry a large amount of localized shear strain, which causes inhomogeneous deformation at low homologous temperatures. Example pictures of shear bands are shown in Figures 1.10, 1.14, 2.2b, 2.3b, and 3.1a-c. While shear bands enable plasticity in MGs, they are intimately linked to the fracture of the material (Section 1.1.4). To illustrate the extent and harsh consequence of strain localization, note that the failure of a MG sample can be solely attributed to one major system-spanning shear band, which is a plane that lies ~45° with respect to the loading axis, as shown in Figure 1.10b and 2.2b. Since the shear band is a 3D planar defect, it is also referred to as a shear-band plane. Further compression of that sample would lead to fracture on that major shear band. Therefore, it is of vast research value to study these defects in order to understand fundamentally the plastic behavior of MGs. More aspects of shear bands will be covered in Section 1.2.

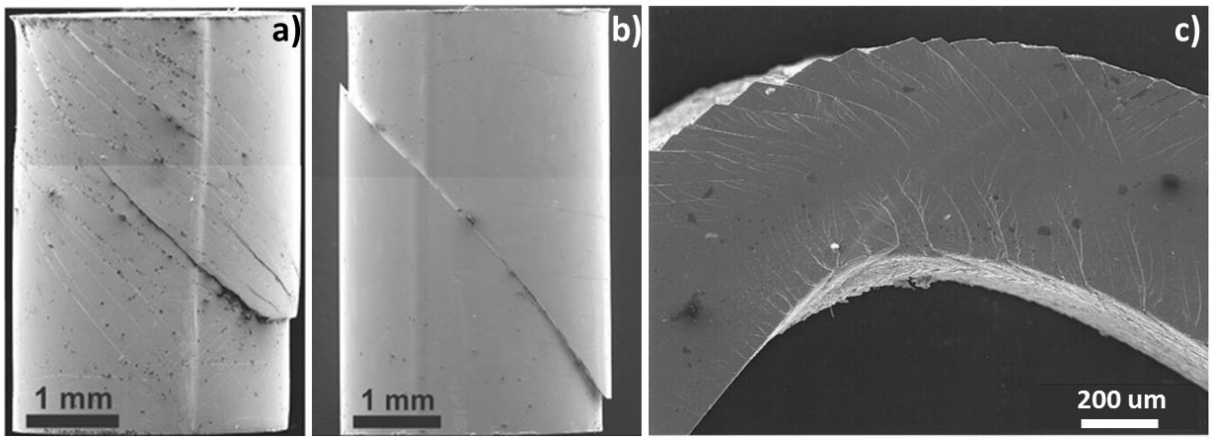

Figure 1.10. SEM images reproduced from References [66, 67] showing various shear-band morphologies. a) A misaligned Vit105 ($Zr_{52.5}Cu_{17.9}Ni_{14.6}Al_{10}Ti_5$) MG compression sample with a dense shear-band structure due to the nucleation of shear bands at the anvil-sample interface. b) A major system-spanning shear band in a Vit105 MG compression sample that did not nucleate from the anvil-sample interface, allowing for unconstrained plastic flow. c) A bent Vit106 ($Zr_{57}Nb_5Cu_{15.4}Ni_{12.6}Al_{10}$), MG sample showing shear bands on both the tensile and compressive sides of the ribbon.

In the context of structural applications that normally operate at low homologous temperatures, it should be noted that the yielding and plastic behavior of MGs deformed in tension are different compared to those deformed in compression [68]. For example, as seen in the

engineering stress and strain curves of a $Ti_{41.5}Zr_{2.5}Hf_5Cu_{42.5}Ni_{7.5}Si_1$ MG in Figure 1.11 [69], the yield strength measured in compression (2080 MPa) is slightly higher than in tension (2050 MPa). This MG alloy has no tensile ductility due to the abrupt rupture on the shear band, while some plastic strain can be carried by a shear band under compression before failure. Moreover, the plastic behavior of the same MG alloy with the same loading condition is usually not consistent. Factors that influence the macroscopic plastic behavior of MGs, besides the loading conditions (stress states) discussed above, include temperature [52, 70-72], strain rate [52, 66], setup stiffness [73], sample diameter [73-76], Poisson's ratio [77-79], and elastic constants [80, 81].

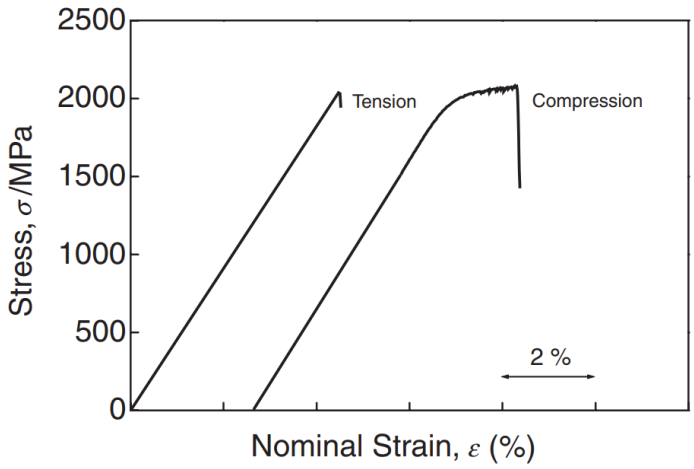

Figure 1.11. Engineering stress-strain curves reproduced from Reference [69] obtained from uniaxial tension and compression experiments on the same $Ti_{41.5}Zr_{2.5}Hf_5Cu_{42.5}Ni_{7.5}Si_1$ MG alloy.

It has been widely observed that the angles of the shear-band plane with respect to the loading axis in both uniaxial tension (θ_T) and compression (θ_C) are not exactly 45°, which is the plane of maximum shear stress. Example angles are shown in Table 1.3. This asymmetry phenomenon can be explained by the fact that the athermal yielding criterion for MGs is different from the classical Tresca [82] or von Mises [83] criteria used in crystals. It was suggested that MGs might follow the Mohr-Coulomb criterion [84, 85], $\tau_y = k - \alpha\sigma_n$, where τ_y is the effective shear yield stress, k is the shear resistance of the glass, σ_n is the stress normal to the plane of shear

yielding, and α dictates the strength of the normal-stress dependence similar to a friction coefficient. The Mohr-Coulomb criterion is used widely to describe yielding in polymers [86], soils [87], and rocks [88], in which a dependency on the stress normal to the plane of shear yielding (σ_n) is necessary due to the relative displacement of interlocking structural units to slide over one another normal to the shear plane in response to the shear stress [89]. The larger deviation from the plane of maximum shear stress in tensile deformation for MGs (>5°) implies that the effect of the stress normal to the shear-band plane is more significant than that in compression, which may lead to more immediate shear-band failure in tensile deformation. Other models have also been proposed to modify the explanation for the asymmetry in compressive and tensile plastic behavior, arguing that the Mohr-Coulomb criterion did not take into account the volume dilatation during the deformation of MGs [90, 91] and that the shear-band angles should also depend on the Poisson's ratio, the coefficient of internal friction, and the dilatancy factor, as a result of material instability [92].

Table 1.3. Angles of shear-band plane with respect to the loading axis in uniaxial tension (θ_T) and compression (θ_c), showing asymmetry in the two loading conditions for several MGs.

	θ_T	θ_C	Reference
$Zr_{59}Ni_8Cu_{20}Al_{10}Ti_3$	54	43	[68]
$Zr_{52.5}Ni_{14.6}Cu_{17.9}Al_{10}Ti_5$	54	44-46	[93]
$Zr_{63.2}Ni_{9.4}Cu_{13.4}Ti_{9.9}Be_{4.1}$	50-53	39.4-41.4	[94]
$Pd_{40}Ni_{40}P_{20}$	50	40	[84]

1.1.4. Fracture

In any deformation mode, fracture in MGs is caused by severe strain localization on shear bands accompanied by material dilatation [52, 95-99] and subsequent local heating [100, 101]. The established views on the structure and dynamics of shear bands are discussed in the next section. This subsection briefly summarizes the current observations on fracture surface morphology in MGs.

At present, the knowledge on the fracture mechanics of MGs is still very limited compared to the understanding of the elastic and plastic behaviors of MGs, the GFA, and the structure of MGs, as briefly discussed in the previous subsections. Consequently, the unrevealed fracture mechanism for MGs has recently attracted more research efforts. The consensus in the field is that the fracture mechanics of MGs are much more complicated than crystalline metals and ideal glasses [102, 103]. Experimentally, the complexity generally comes from i) the large range of fracture toughness values measured for different MGs that are affected by many experimental factors [104-106], ii) the different fracture morphologies observed for ductile and brittle MGs, and iii) the lack of advanced techniques to capture the crack initiation process in MGs. On the modeling and simulation side, the classical fracture criteria (Tresca and von Mises) are not applicable to predict the failure of MGs due to the distinctly different atomic structures in MGs and crystalline metals. The large variation of intrinsic toughness values measured for different MG alloys must be ascribed to the different structures among those alloy systems, such as SRO, MRO or structural heterogeneities over larger length scales.

The crack resistance (damage tolerance) of materials is measured by fracture toughness. Some reported fracture toughness (K_{IC}) values for as-cast MGs are 80 MPa$\sqrt{m}$ for Pt-based [107], 55 MPa$\sqrt{m}$ for Zr-based [108], and 0.5-15 MPa$\sqrt{m}$ for Fe- and Mg-based samples [109, 110]. The

former two are measured from ductile MGs, while the latter is from a brittle MG. A widely used criterion for determining whether a material is ductile or brittle is the solidity index $S = G/B$ [111], where G and B are the shear modulus and bulk modulus. In the case of MGs, which is an isotropic material on the macroscopic level, the solidity index can be expressed as

$$S = \frac{G}{B} = \frac{3(1-2\nu)}{2(1+\nu)}, \tag{1.1}$$

where ν is the Poisson's ratio. A MG is considered ductile when S < 0.41-0.43 or ν > 0.31-0.32 [77, 80, 107].

It has been widely observed that the fracture surface morphologies for ductile and brittle MGs are different. As shown in Figures 1.12a-b, the vein patterns and fishbone patterns were found on the fracture surfaces of ductile MGs from compressive deformation [112], and the combined veins with radiate cores are found on the fracture surface of ductile MGs from tensile deformation [68]. Zhang et al. has studied the difference between the compressive and tensile fracture mechanisms of a ductile Zr-based MG [68]. They proposed that the tensile fracture originated from the radiate cores induced by the stress normal to the shear-band plane and then propagated driven by shear stress (Figure 1.12c), while the compressive fracture of metallic glasses was mainly controlled by shear stress, leaving vein patterns (Figure 1.12a). The fishbone morphology (Figure 1.12b) was ascribed to the stable energy release on a shear-band plane that was constrained by the anvils of the machine during compression [112]. For brittle MGs, the fracture surface of either compressive or tensile deformation consists of the same hackle, mist, and mirror features commonly seen in brittle ceramics and non-metallic glasses [113], as shown in Figure 1.12d [114]. Periodic stripes of various nanometer-scale spacings are observed when zooming into the mirror region on the brittle MG fracture surface for both compressive and tensile deformation, and an example is shown in Figure 1.12e [115].

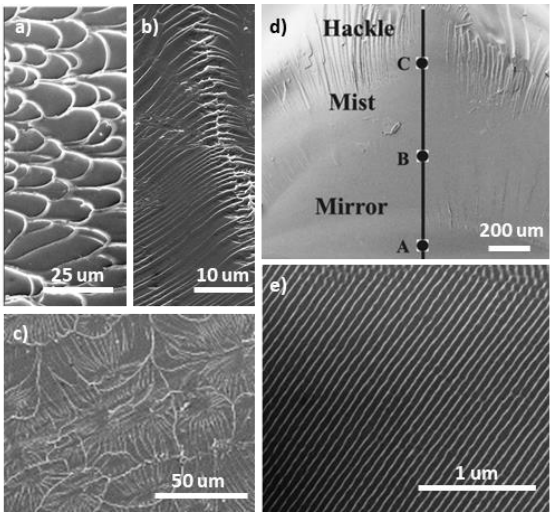

Figure 1.12. a) and b) show the typical vein patterns and fishbone patterns on the fracture surface of a ductile MG after compressive deformation, reproduced from Reference [112]. c) The typical vein patterns with radiate cores on the fracture surface of a ductile MG after tensile deformation, reproduced from Reference [68]. d) The hackle, mist, and mirror regions of a representative (compressive or tensile) fracture surface of a brittle MG, reproduced from Reference [114]. e) Periodic stripes found in the mirror region of a fracture surface in a brittle MG, reproduced from Reference [115].

The fracture mechanisms comparing various materials have been summarized in Figure 1.13 by Sun and Wang [102]. The dislocation-mediated plasticity in ductile crystalline metals causes dimple structures on the fracture surface, and for ideal oxide glasses, ceramics or brittle metals where no plastic flow is involved prior to failure, crack propagates by the cleavage mechanism of directly breaking atomic bonds, which leaves a very smooth fracture surface. The fracture of MGs is considered to include a combination of mechanisms from both ends of the fracture mechanism map shown in Figure 1.13, which gives a variety of fracture surface morphologies in MGs. Sun and Wang attribute the vein patterns on the fracture surface of ductile or tough MGs to the extension and deflection of multiple shear bands ahead of a crack tip. The shear bands form an inhomogeneous plastic zone ahead of a crack tip, different from the homogenous plastic zone ahead of a crack tip in ductile crystalline metals [102]. The nano-scale periodic structures on the fracture surface of brittle MGs may be due to the existence of an even smaller-scale plastic zone ahead of the crack tip, as estimated by Argon and Salama [116], instead

of large numbers of shear bands. Small cavities formed in this plastic zone propagate with the crack, giving rise to the periodic stripes on a fracture surface [110]. Although Figure 1.13 grouped the MGs in compositions to rank their fracture toughness, it should be noted that ductile MGs can be made brittle by inducing structural relaxation (annealing) [117].

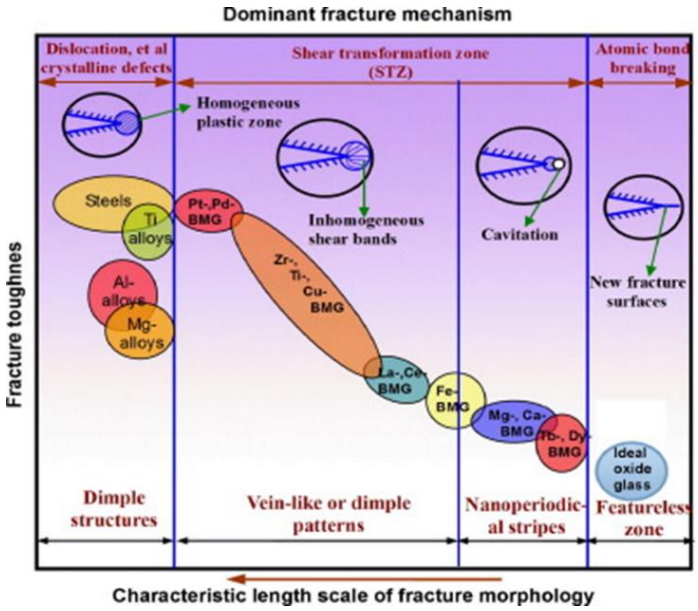

Figure 1.13. Schematic diagram reproduced from Reference [102] summarizing the correlation between fracture morphology and fracture toughness in ductile crystalline metals, ductile MGs, brittle MGs, and ideal oxide glasses in the order from left to right. The proposed fracture mechanisms are also illustrated in the top region of the diagram for the different materials.

To delay fracture (improve ductility and toughness) in MGs, intrinsic and extrinsic approaches have been made. The intrinsic toughening approach [43] uses MG compositions that yield high Poisson's ratio and therefore a low solidity index, as defined above in Equation 1.1. The extrinsic approach [118] introduces secondary crystalline phases as barriers to inhibit shear-band propagation and crack growth, and such alloys are termed "MG composites". Note that the work in this thesis only addresses monolithic MGs, and MG composites are beyond the scope of the discussion here.

1.2 Shear bands in metallic glasses

This section provides a general overview of the current understanding of shear bands in MGs, including the observed shear-band structure from the nano-scale to the micro-scale, shear-band dynamics, and the proposed shear-band-to-crack transition mechanism.

1.2.1 Nano-scale shear band core and micron-size shear zone

The macroscopically observable shear-band morphologies are shown previously in Figure 1.10, which are essentially the surface steps of shear bands. The first transmission electron microscopy (TEM) images of shear-band structure in MGs was reported by Masumoto and Maddin in 1971 in the early pioneering work to study the mechanical properties of MGs [119]. They called the distinct features that stood out in sharp contrast to the undeformed matrix material "deformation lines" at that time. Interestingly, the observed deformation-line thickness from their work was ~20 nm, as shown in Figure 1.14, which coincided with the shear-band thickness values measured much later from a variety of deformed MG samples [120], including those observed using high-resolution TEM (HRTEM), as listed in Table 1.4. After reporting the difference in chemical etching susceptibility between the shear-band material and the matrix material in a MG sample by Pampillo and Chen [121], it was evident that the atomic structure of shear bands should be different from the undeformed matrix. Recent studies using in-situ acoustic emission (AE) [122] and TEM techniques [95, 96, 123] have shown differences in density between the shear band and the matrix, ranging from -10% to +6%. These density differences have been attributed to local structural dilatation [95, 122], compositional differences [95, 124-126] and the inclusion of either nanocrystals [127-130] or sub-nanometer to nano-scale voids [131-134] in the shear band. However, no consensus has been reached yet on the origin and formation mechanism of such

structural differences between the shear-band and the matrix materials in MGs, due to experimental difficulties. Modeling approaches combining atomistic simulations and continuum approaches [135] may be ideal tools to investigate such fundamental properties.

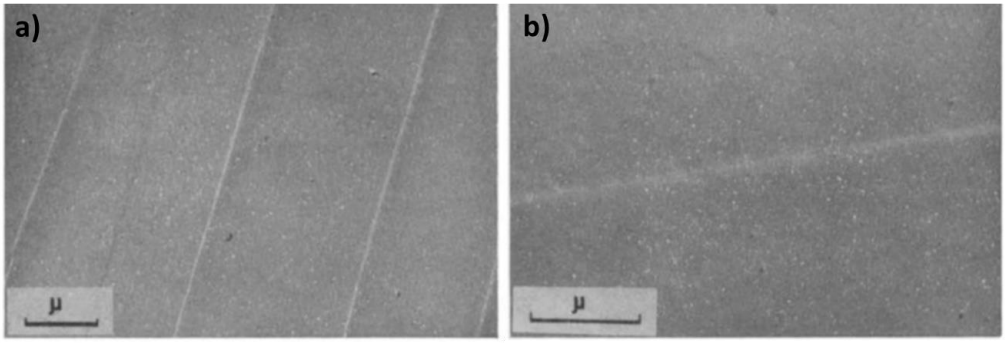

Figure 1.14. Two of the earliest reported TEM images of shear bands in MGs reproduced from Reference [119].

Table 1.4. A list of shear-band thickness values measured from different MGs, as summarized in Reference [120].

MG	Technique	Shear-band thickness (nm)	Reference
$Pd_{80}Si_{20}$	TEM	20	[119]
$Fe_{40}Ni_{40}B_{20}$	TEM	10-20	[136]
$Zr_{56.3}Ti_{13.8}Cu_{6.9}Ni_{5.6}Nb_{5.0}Be_{12.5}$	TEM	≤10	[137]
$Zr_{57}Ti_5Cu_{20}Ni_8Al_{10}$	HRTEM	≤20	[131]
$Al_{90}Fe_5Gd_5$	HRTEM	10-15	[128]
$Al_{86.8}Ni_{3.7}Y_{9.5}$	HRTEM	10-15	[128]

It is important to note here that beyond the nano-scale shear-band structure observable using the TEM, there is also a micron-size zone affected by the nano-scale strain localization, and it is not seen on the TEM but can be detected by indentation hardness or modulus variations [97, 99] and X-ray diffraction (XRD) techniques that map local strain fields [138-141]. To distinguish the two regions, the observable nano-scale shear band is termed as the "shear-band core", and the

micron-size shear-band vicinity is generally called the “shear-band region” or “sheared zone”. A first indication for a much larger length scale associated with shear bands than the characteristic nano-scale shear-band core is the work by Pan et al. [99] in 2011, who conducted lines of nanoindentation experiments across an isolated shear band in each of their Zr-based MG samples. A local hardness reduction around the shear band was reported, where the softening profile had a width that scaled with the macroscopic plastic strain of the investigated samples. Figure 1.15a displays the hardness profiles obtained after 2%, 4%, and 6% macroscopic plastic strains. The zone of structural softening extended over tens and up to ~150 μm and was explained with free volume diffusion away from the shear-band core into the surrounding matrix, which was suggested to be dependent on the plastic shear strain. Structural softening due to shear banding had been proposed [142, 143] prior to the experimental work reported in Reference [99], but the introduction and characterization of such unknown long-range signatures originating from nano-scale strain localization that was evident on isolated and system-spanning shear bands allowed much deeper insights than before. Subsequently, Maass et al. presented hardness fluctuations around an isolated and system-spanning shear band that had mediated all plastic strain of another Zr-based sample deformed by uniaxial compression [97]. An example of the hardness reduction around the single shear band is shown in Figure 1.15b, indicating the position-dependent nature of softening along the shear-band path that extended ~100 μm, as well. Different from Pan et al., this work prompted another interpretation, which is based on the nanoindentation hardness reduction (or increase) due to in-plane tensile (or compressive) stresses [144, 145]. It ascribed the softening to the internal stress fields within the long-range shear-band region. Reports using X-ray diffraction were also able to support the existence of the long-range shear-band region beyond the shear-band core by mapping out residual strain fields extending tens of micrometers away from the shear-band core

[138] or around shear bands in a damage zone ahead of a crack tip [139]. Further proof was provided by Vinogradov et al. [140], who experimentally determined a strain-distribution map that was in good agreement with theoretically predicted displacement fields known for dislocations, as well as by Binkowski et al. by local strain mapping [141]. Overall, with the distinction between a nano-scale shear-band core and a micron-size long-range signature into the surrounding matrix, the definition of a shear band has become more complex in recent years.

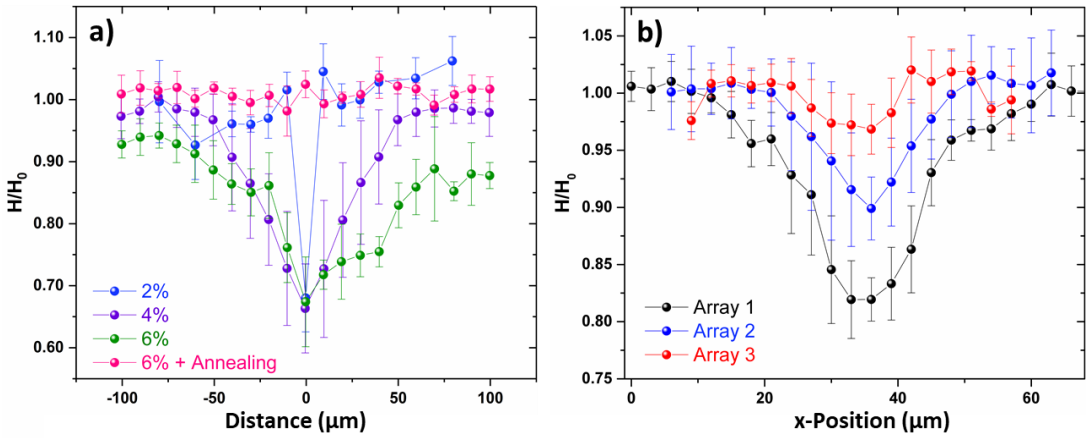

Figure 1.15. a) Hardness profiles normalized by the matrix hardness adapted from Reference [99], which were obtained by nanoindentation across an isolated shear band from three $Zr_{69.5}Cu_{12}Ni_{11}Al_{7.5}$ MG samples deformed in uniaxial compression to 2%, 4%, and 6% macroscopic plastic strain, and after annealing the 6% plastic strain sample at 593K (30K below T_g) for an hour. The width of the shear-band softening region scales with the amount of plastic strain. b) Nanoindentation hardness profiles normalized by the matrix hardness adapted from Reference [97], which were obtained across a system-spanning shear band produced by uniaxially compressing a Vit105 MG sample, revealing a position-dependent hardness reduction for the same shear band.

1.2.2 Shear-band initiation, propagation, and arrest

While shear bands are not unique to MGs, the structural origin and evolution are different for different materials. In granular media, shear bands initiate due to local density fluctuations and packing imperfections [146]; in crystalline metals, a number of grains turn to a texture favored for shearing; in amorphous polymers [147], the alignment of molecular chains results in shear thinning [148]. For MGs, the spatial (nano-scale core structure) and temporal (millisecond propagation time) confinements of shear bands make them very difficult to study experimentally. The majority of

research efforts focused on inactive or post-mortem shear bands, and only recently have the dynamic properties of shear bands been revealed with experiments, as summarized in Reference [66].

The plastic regime of a stress-strain curve in MGs either shows intermittent activation of shear bands (serrated flow) or an apparent smooth flow of shear bands (non-serrated flow), depending on the applied strain rate and testing temperature. For serrated flow, the shear-band velocity is higher than the applied strain rate (low strain rate and high temperature), and vice versa for non-serrated flow. Figure 1.16a shows the partial plastic regime of four different stress-strain curves from uniaxially compressing Vit105 MG samples, which illustrate the effect of strain rate and temperature on shear-band dynamics. As seen in Figure 1.16a, the stress drop magnitude ($\Delta\sigma$) or force drop magnitude (ΔF) decreases with decreasing temperature and with increasing strain rate (drive velocity). Kimura and coworkers demonstrated that the transition between serrated and non-serrated flow for MGs follows an Arrhenius-type equation, indicating a thermally activated structural mechanism that is rate-sensitive [149-151]. In other words, there is a competition between the applied deformation rate and the shear-band propagation velocity. The serrated flow of MGs resembles a stick-slip behavior, which is known for many other types of materials [152], where the base stress remains the same but the peak stress depends on the applied strain rate. It is suggested that this phenomenon in MGs is related to the time scales of competing processes within the shear band, which has less time to strengthen statically with increased drive rate, thus decreasing the peak stress or force [153]. Zooming in to one elastic loading and subsequent stress-drop cycle, as shown in Figure 1.16b, one can see the three dynamic stages of a shear band within the time scale of a few milliseconds: i) initiation (at peak stress), ii) propagation (generation of deformation displacement, Δu, or plastic strain), and iii) arrest (shear-banding stops).

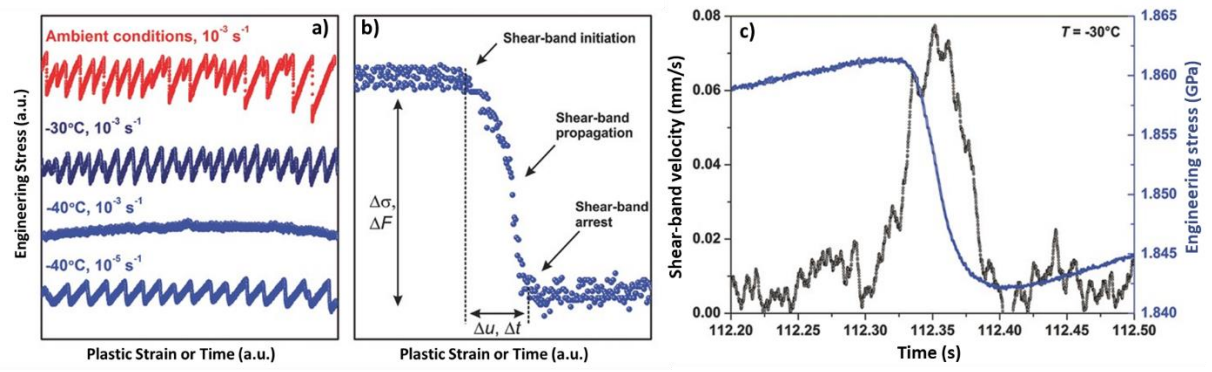

Figure 1.16. a) Serrated and non-serrated stress-strain curves of Vit105 MG samples deformed by uniaxial compression at various temperatures and strain rates. b) Zoom-in view of a typical stress drop with indications of the dynamic stages of a shear band and the corresponding change in stress or force and change in displacement or time. c) Shear-band propagation velocity calculated from the stress drop shown. a)-c) are reproduced from Reference [66].

The initiation of a shear band is not obvious from the stress-strain curves, as there is no feature that forecasts its initiation, so the time scale of shear-band initiation must be well below the millisecond range. Klaumünzer et al. [122] used an in-situ acoustic emission (AE) method with microsecond resolution to probe the shear-band initiation signal in a Vit105 MG sample during compression. Distinct AE pulses showed peak amplitude just before the stress drop when plotting the AE and stress-time curves together with time synchronization, serving as an indicator of the shear-band initiation process that had a duration of ~25 μs. Shear-band volume dilatation was derived from the AE pulses using the AE-pulse rise time (t_r) and amplitude (U_p): $\partial V \approx \frac{1}{2C} t_r U_p k_f$, where C is a constant and k_f is a sensor calibration factor. The measured shear-band volume dilatation using this AE method spanned from 0 to 8.5%, and these are the first reported in-situ measurement of dilatation values from the shear-band initiation process.

Three scenarios of shear-band initiation are possible. The first is the percolation of homogeneously activated STZs along the plane of maximum shear stress that causes softening of the material and therefore would concentrate shear strains. This scenario is referred to as the homogeneous nucleation of a shear band in MGs and is caused by structural fluctuations, as

observed in computer simulations [154], rather than extrinsic flaws (heterogeneous nucleation sites). The second scenario involves stress concentrators (surface defects from casting or notching or voids within the system) that preferentially initiate a shear band that, after reaching a critical size, would propagate and develop into a mature shear band, which have also been demonstrated with computer simulations [155-157]. The third scenario suggests that the formation of shear band consists of two consecutive stages: i) structural rejuvenation through activation of STZs along the shear band that softens the material, which can initiate from local stress concentration similar to the second scenario but has limited shear strain and no significant temperature increase, and ii) synchronized sliding along the rejuvenated and softened path, during which large plastic strain and local heating are possible. The third scenario has also been supported with simulation work [158-160]. The two-stage scenario can possibly explain the discrepancy in experimentally measured shear-band propagation speed by differentiating which stage the measurements are taken from. It suggests that the shear band propagates around the speed of sound in the first stage, while the synchronized sliding in the second stage is much slower (~mm/s) and depends on the loading conditions and sample size [161].

For shear-band propagation, three important points should be noted here. Firstly, a single stress drop in the serrated stress-strain curve during uniaxial compression of a MG sample with an unconstrained shear band has been verified to be exclusively related to the activation of this shear band [162, 163]. The verification is necessary for studying the dynamics and structure of this one shear band that has carried all the plastic strain during deformation. Secondly, high-speed imaging has allowed the observation of shear-band propagation that occurs in the millisecond time range at room temperature and in a simultaneous way across the entire shear plane (continuous sliding of two surfaces) instead of a progressive moving front [163, 164]. Thirdly, shear-band propagation

is a thermally activated process, and the shear-band velocity decreases with decreasing temperature in an Arrhenius way [162, 165].

Shear-band velocity could be calculated using a single stress drop, and a typical shear-band velocity profile is shown in Figure 1.16c [66]. The message from a concave-down velocity profile is that deceleration clearly takes place before the shear band reaches its maximum velocity. This deceleration behavior indicates that the shear band does not lead to detrimental run-away propagation but eventually comes to an arrest before accommodating more plastic strain during deformation. The underlying structural mechanism that allows shear-band arrest is structural re-strengthening, or aging, which has been modeled by effective temperature dynamics based on the STZ theory [166] and can be understood as a process that involves reforming broken bonds of certain atomic clusters from molecular dynamics simulations [167].

1.2.3 Shear-band-to-crack transition

Since shear bands in MGs induce failure, it is instinctive to ask: what is the exact mechanism behind this? The first evidence of micron-size cavity (crack or void) formation in shear bands was reported by Pampillo and Chen in 1974 [121], who presented multiple cavities along a major shear band in a uniaxially compressed $Pd_{77.5}Cu_6Si_{16.5}$ MG sample deformed to 40% total axial strain, as shown in Figure 1.17a. The fact that those cavities exceeded 100 μm in length implies that they were intimately connected to the failure of the sample. However, these cavities were not discussed further in Reference [121] and they have received very little attention. Since then, the predominant focus of void formation in shear bands has been in the nanometer range.

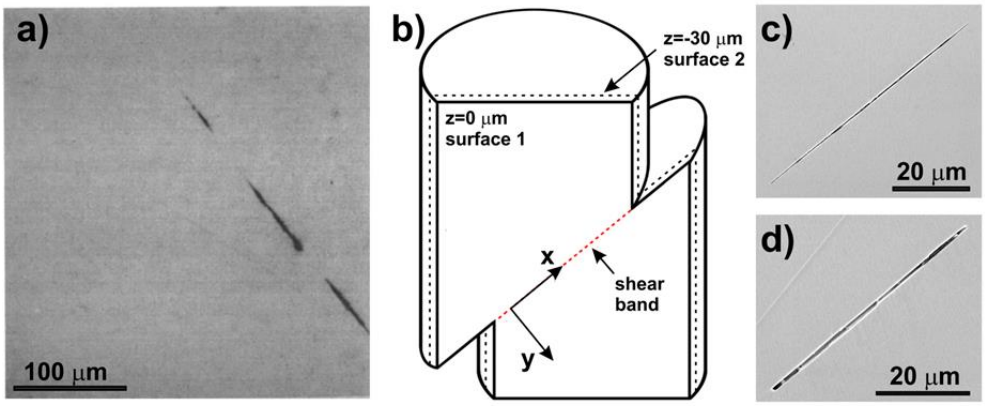

Figure 1.17. a) First-reported micron-size cavities along a shear band in a compressed $Pd_{77.5}Cu_6Si_{16.5}$ MG, reproduced from Reference [121]. b) Schematic of a cross-sectional surface after mechanically polishing a compressed Vit105 MG rod, reproduced from Reference [97]. The major shear band is indicated by the dotted line in the x-direction. Micron-size cavities along this shear band were imaged with SEM and displayed in c) and d), which show similar plate-like shape as those reported in Reference [121].

Using HRTEM in combination with Fourier filtering and thresholding techniques [168], Hufnagel and coworkers resolved nano-scale regions that had significantly different density than the average matrix material in a deformed Zr-based MG. In addition to these structural variations, they also revealed a large concentration (1/100 nm^3) of voids with a size of ~1 nm [131]. These voids were only found in the material that was inside a shear band, and it was thus proposed that the coalescence of excess free volume in the shear band after the removal of stress led to the formation of nano-scale voids in the shear bands. A more complex view emerges when comparing results obtained from bending Al-based MGs, which were analyzed with the same HRTEM techniques [128]. This work showed that on the compressive side in both the undeformed region and inside the shear band of an $Al_{90}Fe_5Gd_5$ MG sample, only a few nano-scale voids ($\leq$1 nm) were found without significant difference between the deformed and undeformed regions. On the tensile side, a clear and uniform distribution of nano-scale voids was observed inside the shear-band core close to the interface with the matrix. Such a difference in void population indicated a sensitivity of free volume coalescence to the stress state. Furthermore, in another Al-based MG sample

($Al_{86.8}Ni_{3.7}Y_{9.5}$) studied also in Reference [128], nano-scale voids were found to distribute evenly throughout the shear band but with a lower density than in the $Al_{90}Fe_5Gd_5$ MG. The $Al_{86.8}Ni_{3.7}Y_{9.5}$ MG also showed a higher degree of nano-crystallization, indicating a negative correlation between crystallization and void formation inside the shear band. This work suggested that only the availability of enough excess free volume not coalesced into nano-scale voids would allow atomic transport and thus crystallization. Yet other studies were not able to confirm the existence of nano-scale voids in shear bands of bent $Zr_{66.7}Cu_{33.3}$ [133] or compressed $Pd_{40}Ni_{40}P_{20}$ [123].

The aforementioned works using HRTEM methods focused on the scale of ~1 nm or less, while other TEM investigations have imaged voids in shear bands that range ~5-100 nm [132, 169]. Such voids were directly observable from TEM specimens without applying Fourier analysis. It was hence concluded that a cavity forms via excess free volume coalescence to nano-scale voids [132, 169-172]. The voids can then grow and connect to form micron-size cracks, causing the proposed shear-band-to-crack transition, which provides a mechanistic view on how a developed shear band can induce fracture in a MG. Although this mechanism is plausible, it should be noted here that the shear-band-to-crack transition mechanism is proposed solely on the basis of TEM investigations that are not able to capture the entire process from nano-scale void coalescence to micron-size cavity formation, which spans a significant length scale. In other words, the evidence of nano-scale voids from TEM studies can only be used in a very early stage of the proposed shear-band-to-crack transition mechanism.

Recently, Maass and coworkers reported on micro-scale cavities similar to those presented in Reference [121] by cross-sectional polishing of a uniaxially compressed Vit105 MG sample [97], as shown in Figures 1.17 c and 1.17d with a schematic of the sample shown in Figure 1.17b. All macroscopic plastic strain in this sample was carried by a major system-spanning shear band.

Careful mechanical polishing along the z-axis shown in Figure 1.7b revealed a complex 3D arrangement of micron-size cavities with ~200-300 μm in length and ~1-6 μm in width. The length to width ratio indicated that the cavities were planar, and the summed length of micron-size cavities along the shear-band path on a given x-y-plane could be as high as 20%. The relative misorientation of the major cavity axis on each cross-sectional surface suggested that the shear-band plane was not exactly planar, assuming that the formation of such cavities is a result of the nano-scale void formation process inside the shear band as discussed above. It is thus suggested that the non-planar shear band can develop off-axis stress components relative to the shear direction that can cause long-range stress fields around the nano-scale shear-band core. Cavities are expected to form at locations with high tensile stress components, leading to local fracture on the shear band. This finding supports the idea that cavities should form way before the fracture point of a MG.

1.3 Research objectives

This dissertation work aims to expand the current knowledge on shear-band structure from the nano-scale to the micro-scale. Three key questions are addressed in this thesis, which are discussed in the following subsections.

1.3.1 Is the structure of the nano-scale shear-band core dependent on shear strain?

A large body of current research work on shear-banding behavior in metallic glasses has in common that it essentially does not address any strain-dependent properties. In other words, it implicitly assumes structural consistency with strain, prompting us to ask the question: would the structure of an active shear band change during strain accumulation? If so, what is the influence of strain on the shear-band dynamics and plastic flow? There is extremely little experimental data

available that characterizes and quantifies how plastic strain and thus structural damage accumulates in MGs. This situation stands in stark contrast to crystalline metals, for which textbooks can be filled with the detailed description of structural evolution as a function of plastic strain. Part of the work in this thesis attempts to address this fundamental shortcoming in MGs. The hypothesis is based on the earlier reported observation that the shear-band velocity can increase as a function of strain [173], raising the suspicion that this is caused by some structural damage accumulation in the nano-scale shear-band core. The results of the experimental work that aimed to solve the strain-dependent structural properties of the shear-band core in MGs are presented in Section 3.3 (submitted) with the necessary foundational work summarized first in Section 3.1 (published in Reference [98]).

1.3.2 What is the origin of density change in the nano-scale shear-band core?

There are two important reasons to addressing this question. Firstly, in our attempt to probe the structural properties of the nano-scale shear-band core, a TEM-based technique (Section 2.2.1) was used to measure the density change of the shear band with respect to the matrix material. The measured density change could depend on structural and compositional variations. To this end, experimental methods that probed the chemical composition (Sections 2.2.3, 2.3.1 and 2.4) of the shear bands must be conducted to validate the TEM-based density change measurements. Secondly, we would like to contribute to the inconclusive and scarce literature on shear-band chemistry for non-crystallized shear bands. The experimental results for addressing this question are presented in Section 3.2 (published in Reference [174]).

1.3.3 Are there any other damage signatures in the long-range shear-band region?

The distinction between the nano-scale shear-band core and the long-range shear-band region has been discussed in Section 1.2.1, with the observation of micron-size cavities that indicate a non-planar shear band causing long-range stress fields around the nano-scale shear-band core reported in Section 1.2.3. Having so far relied on classical metallography, the purpose of this work is to further study these cavities and their relation to the shear band in 3D prior to sample failure. An X-ray tomography technique (Section 2.3.2) was used to reconstruct MG samples compressed to different macroscopic plastic strains before fracture, aiming to find internal cavities. With the reconstruction of cavities in the shear-band region, further questions can be raised and addressed, which involve the evolution of these cavities and their effect on the stress-strain curves of MGs. The results are summarized in Section 3.4 (published in Reference [175]).

CHAPTER 2: EXPERIMENTAL METHODS

This chapter describes the experimental methods used for the preparation and characterization of MG samples and the analysis methods used for the data collected from the experiments.

2.1 Metallic glass sample preparation

Two compositions of Zr-based MG samples were used: Vit105 ($Zr_{52.5}Cu_{17.9}Ni_{14.6}Al_{10}Ti_5$) and $Zr_{65}Cu_{25}Al_{10}$ (at.%). The Vit105 samples were either cast in-house or commercially purchased from Liquidmetal, and they were used for the TEM and X-ray fluorescence (XRF) experiments described in Section 2.2 and Section 2.3.1, respectively. All the $Zr_{65}Cu_{25}Al_{10}$ samples were cast in-house, and they were used for the X-ray tomography (XRT) and atom-probe tomography (APT) experiments described in Sections 2.3.2 and 2.4, respectively. These two compositions were selected based on their good GFA for in-house casting, known plastic straining capability at room temperature in compression, and readily available comparison in mechanical properties to large base of literature data [165, 176, 177].

2.1.1 Casting of metallic glass samples

To cast the MG samples in-house, commercially purchased raw materials from Alfa Aesar (Zr with 99.8% purity; Cu, Ni, Al, and Ti with 99.999% purity) were first etched to remove surface oxide contamination and weighed in proper mass proportions to produce pre-alloy lumps that were later heated and quenched to amorphous cylindrical samples. The etchants were: a mixture of nitric acid, hydrofluoric acid and water in volumetric ratio of 1:1:10 for Zr, Al and Ti [176], and a mixture of hydrochloric acid, nitric acid and water in volumetric ratio of 10:33:67 for Ni [178],

and concentrated nitric acid for Cu [176]. The raw materials were placed in target mass proportions in an Edmund Buehler mini-arc melter, as shown in Figure 2.1a, with high-purity Ar atmosphere (99.9997% Ar from Airgas) and formed into a ball-shape pre-alloy lump.

About 0.8-1.2 g of the pre-alloy lump was used each time to cast MG rods that were 2 mm in diameter and 32 mm in height. The piece of pre-alloy lump was placed in the mini-arc melter chamber together with a piece of high-purity Ti, which was used as an oxygen getter when heated. After achieving high-purity Ar atmosphere with a slight over-pressure (~0.1 bar) in the chamber and an under-pressure (-0.1 to -0.5 bar) in the reservoir, the piece of pre-alloy lump was heated by the electric arc to a temperature above its T_g (shown in Figure 2.1b) and suction cast into a Cu mold when the entire body of the lump glowed uniformly in an orange color. The setup was water cooled, and the suction casting process quickly quenched the heated pre-alloy lump into an amorphous rod, as shown in Figure 2.1c. More detail about the mini-arc suction casting process can be found in Reference [176].

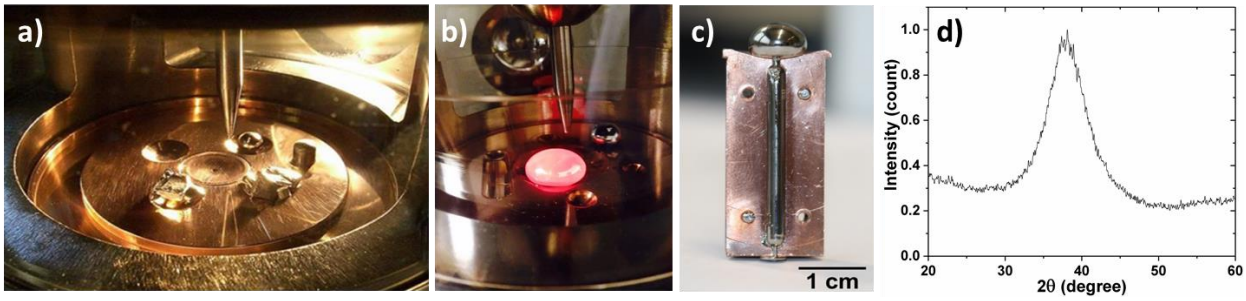

Figure 2.1. a) Edmund Buehler mini-arc melter chamber with the raw metals for making the pre-alloy lump. b) A glowing piece of $Zr_{65}Cu_{25}Al_{10}$ pre-alloy lump ready to be suction-cast into an amorphous sample. c) A $Zr_{65}Cu_{25}Al_{10}$ rod cast from the mini-arc melter sitting in its Cu mold. d) A representative XRD plot of a Vit105 MG.

To verify the amorphous structure of the rods, discs about 1 mm in height were cut off from the rods using a Buehler diamond saw, polished for smooth surface finish, and tested using X-ray diffraction by a PANalytical Phillips X'pert XRD system. Figure 2.1d shows an example XRD plot from a Vit105 MG cast in-house. The broad peak without sharp crystalline peaks

confirms the amorphous structure of the MG, and its 2θ value of ~37° is equivalent to q ≈ 2.6 $Å^{-1}$, which is the first peak of the structure factor, that is in agreement with other X-ray diffraction and neutron diffraction data for MGs of this composition [179, 180].

2.1.2 Deformation of samples to produce shear bands

The MG rods cast in-house were cut with a diamond saw into shorter cylindrical rods with diameter-to-height aspect ratios of 0.5-0.6. The top and bottom surfaces of the shorter rods were ground parallel and then notched on the side using an electrical discharge machine (EDM) with 50 μm diameter brass wire. Each notch was 45° with respect to the vertical axis of the cylinder, about a quarter of the height away from one of the parallel surfaces of the rod, and approximately 0.5 mm in depth, as shown in Figure 2.2a. The reason for grinding the two surfaces parallel on each rod was to ensure uniaxial compression during deformation between parallel anvils. The small notch initiated shear banding exactly on the free lateral surface instead of at the sample-anvil contact, thus producing a system-spanning shear band on each rod upon plastic deformation, as shown in Figure 2.2b. Note that notching was not required, but it made it experimentally easier to initiate a system-spanning shear band at a target location [181]. The compressed sample in Figure 2.2b was polished to a cuboid shape for extracting TEM specimens that contained the shear band, and a schematic of the 3D shape is shown in Figure 2.4a.

Plastic deformation of the Vit105 and $Zr_{65}Cu_{25}Al_{10}$ rods was conducted uniaxially in compression using an Instron 5900R machine (model 4507) with a strain rate of 10^{-3} s^{-1} at different temperatures in either the non-serrated flow regime (high strain rate and low temperature, e.g. -60 °C) or the serrated regime (low strain rate and high temperature, e.g. room temperature), as discussed earlier in Section 1.2.2. It should be noted that the shear-band morphology does not

depend on the flow mode (serrated or non-serrated flow) in uniaxial compression, as supported by previous studies [66]. Low-temperature compression was done inside the environmental chamber attached to the Instron machine, which led liquid nitrogen in for cooling. The samples were unloaded prior to failure so they remained intact for experiments described in Sections 2.2-2.4. Examples of the engineering stress and strain curves for the compressed rods are shown in Figure 3.27 in Section 3.4.1 with the correction for machine compliance. The method for correcting machine compliance is by subtracting the displacement of the Instron machine in the elastic regime from the elastic displacement of the compressed sample. The corrected sample displacement was then used for calculating its strain.

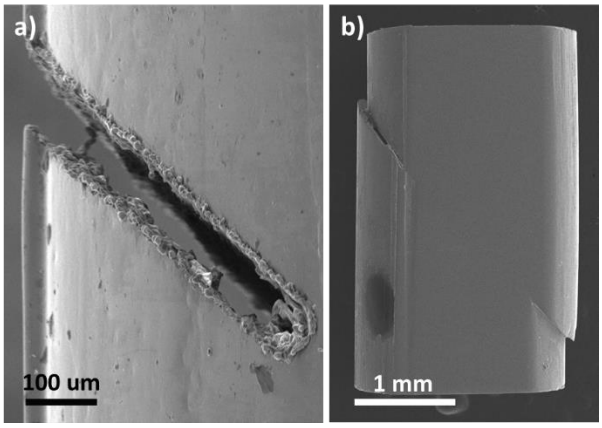

Figure 2.2. a) SEM image of an example EDM notch on a MG rod prior to compression. b) SEM image of a notched and compressed MG rod that contains a system-spanning shear band and polished to a cuboid shape, viewed normal to the polished flat side.

Another way to produce shear bands in this work was by bending. A Vit105 plate commercially purchased from Liquidmetal was cut into a bar (0.5 mm × 1.5 mm × 45 mm) using EDM. The heat-damaged zone from EDM cutting was ground off. This bar was bent at room temperature using a 3-point bending setup, as shown in Figure 2.3a. Shear bands are seen on the surface of the bending bar as surface offset steps, and the magnitude of the surface step decrease to zero at the end of the shear band when measuring from the edge of the bar to the inner region, as shown in Figure 2.3b. TEM specimens were extracted from these shear bands with measurable

surface offsets, allowing the calculation of local shear strain (shear strain = surface offset / shear-band thickness).

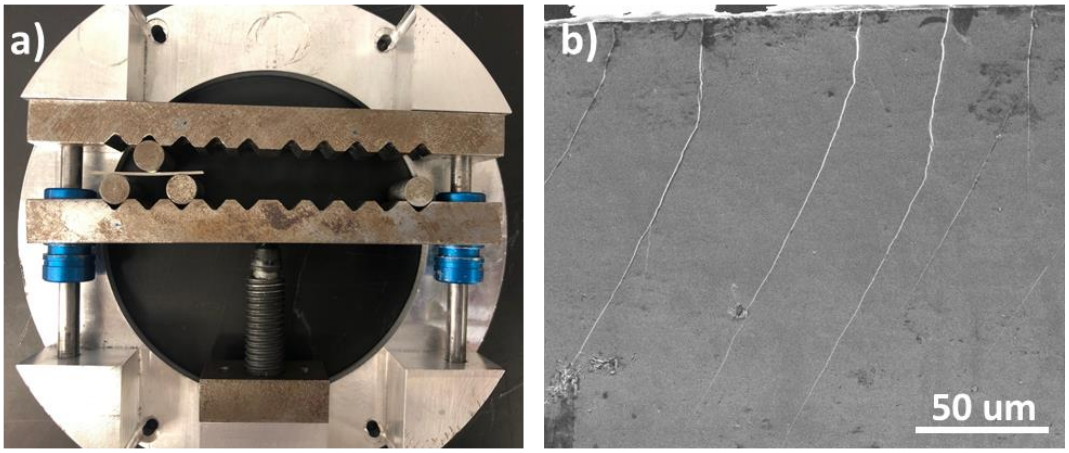

Figure 2.3. a) The 3-point bending setup that has a MG bar loaded prior to bending. b) SEM image showing shear-band surface steps on the tensile side of the bending bar.

2.1.3 Transmission electron microscope lamella preparation

TEM specimens were extracted from compressed Vit105 rods, bent Vit105 bar, and compressed $Zr_{65}Cu_{25}Al_{10}$ rods and polished to thin lamellae of ~100 nm thickness using a Helios 600i focused ion beam (FIB) machine for electron transparency. Note that when extracting TEM lamellae from the compressed rod samples, it was not obvious to find the exact location of the shear band as the sample was polished to a mirror finish, removing the surface step of the shear band, as shown in Figure 2.2b and Figure 2.4a. In this case, the micron-size cavities along the shear-band path that were revealed on the sample surface after polishing were used as reference marks on the shear band. Examples of these cavities are shown earlier in Figures 1.17a, 1.17c, and 1.17d, which were scarcely reported in the literature [97, 121] prior to this work. An imaginary line connecting the cavities was used to locate the shear band, as shown in Figure 2.4b. This method did not always work, especially when trying to locate the shear band far away from visible surface cavities and not being able to connect two cavities in the viewing window. Multiple FIB-

liftout attempts must be made to include a shear band on a TEM lamella. On the other hand, it was much easier to locate shear bands on the bending bar sample, since the surface steps were readily visible.

To make a TEM lamella, a 2 μm × 2 μm × 12 μm Pt protection layer was first deposited perpendicular to the shear band using 30 kV 80 pA Ga ion beam with the sample surface perpendicular to the ion beam (52° stage tilt). The shear band was placed roughly in the middle below the Pt layer, as shown in Figure 2.4c. Then two rectangular trenches (approximately 14 μm × 7 μm × 5 μm) were milled on either side of the Pt layer using 30 kV 21 nA ion beam. After formation of the trenches, a 30 kV 2.5 nA ion beam was used to clean both sides of the still-thick TEM specimen protected by the Pt layer on top. Then a partial U-shape cut was made by a 30 kV 2.5 nA ion beam with the sample surface perpendicular to the electron beam (0° stage tilt) to ensure the bottom of the TEM specimen was fully detached from the rest of the bulk sample and remained attached on one side. The TEM specimen was welded to an Omniprobe tip (tungsten needle) with Pt using 30 kV 80 pA ion beam, and the U-shape was fully cut so the TEM specimen was free to be lift out from the bulk sample, as shown in Figure 2.6a. Note that after liftout, the Omniprobe was rotated 180° manually so that the specimen flipped 90°. This step allowed the shear band to span horizontally in the middle of the specimen. It was necessary as the shear band was then perpendicular to the ion-milling direction during specimen thinning, which prevented the curtaining effect in the direction of the ion beam to interfere with the visibility of the shear band. As seen from the HAADF-STEM images in Figure 3.1, the shear bands in all the images lie perpendicular to the alternating bright and dark contrast caused by the curtaining effect.

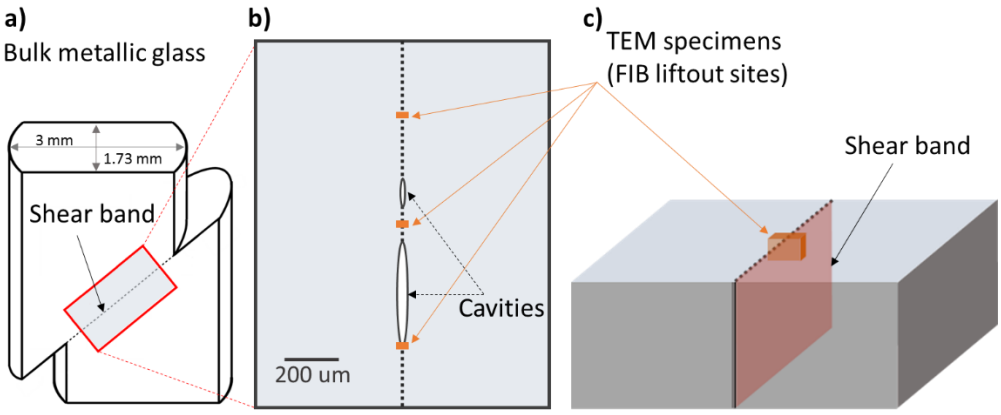

Figure 2.4. a) Schematic of a compressed and polished MG specimen where the dashed line within the red box indicates the location of the major shear band. b) Schematic of polished surface showing two surface cavities along the shear band, around which several TEM specimen were extracted using FIB. c) A 3D representation of where the shear band intersects a TEM specimen.

The rotated TEM specimen was transferred and welded to a Ted Pella PELCO FIB lift-out TEM grid made of Cu and then detached from the Omniprobe tip. Two types of TEM grid geometries were used: single wide-post grids and 4-narrow-post grids, as shown in Figure 2.5. The advantage of using the wide-post girds was that the TEM specimen could be attached to the post on more than one side of the v-shape part for more security. The disadvantages were that only one specimen at a time could be mounted to the grid and the appropriate size to fit the particular specimen had to be ion milled each time, taking much longer to weld a specimen to a wide post than to a narrow post. On the other hand, the 4-narrow-post grids had the advantage of mounting multiple TEM specimens at a time, which was especially useful for making atom probe samples, as described in Section 2.1.4. More caution was needed when handling the 4-narrow-post grids since the TEM specimen was only welded to the post on one side.

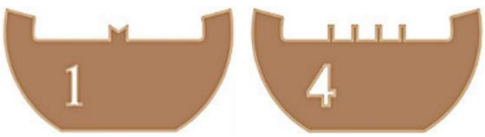

Figure 2.5. Ted Pella PELCO FIB lift-out TEM grids: wide post (left) and 4-narrow-post (right).

For specimen thinning, firstly, the specimen was tilted ±1.5^{o} from the incoming ion beam direction every time during the 30 kV 0.79 nA thinning process until the wedge-shape specimen was ~100 nm thick. The ion beam current could be reduced to 80 pA when approaching the 100 nm thickness. Then a 5 kV 41 pA ion beam cleaned each side of the specimen for 2 minutes with the specimen tilted ±3° from the incoming ion beam. The final step used a 2 kV 23 pA ion beam to clean each side of the specimen for 1 minute with the specimen tilted ±5° from the incoming ion beam. Representative TEM lamellae are shown in Figure 2.6b and Figure 2.6c, mounted on a wide-post grid and on a narrow-post grid, respectively. The TEM lamella in Figure 2.6b was lift out from the polished side of a compressed rod sample, where the shear-band surface step was removed due to polishing. After the 90° lamella rotation, the surface step would lie on the vertical side of the lamella if it was still existent, serving as a shear-band marker. Since it was no longer present after polishing, it made no difference whether to mount it on a wide-post grid or a narrow-post grid. The shear band located roughly in the middle of the lamella in Figure 2.6b with no clear indication of its exact location, making it difficult to find in the TEM. In comparison, the TEM lamella in Figure 2.6c was lift out from the bending bar sample where shear-band surface steps were not removed by polishing. The lighter area on the left side of the lamella in Figure 2.6c is the Pt protection layer, and the surface step is made obvious by the interface between the Pt layer and the MG, which served as a clear and accurate indication of the nano-scale shear band, not visible in the SEM image. A TEM image that displays a shear band connected to the surface step in this type of lamella is shown in Figure 3.17c.

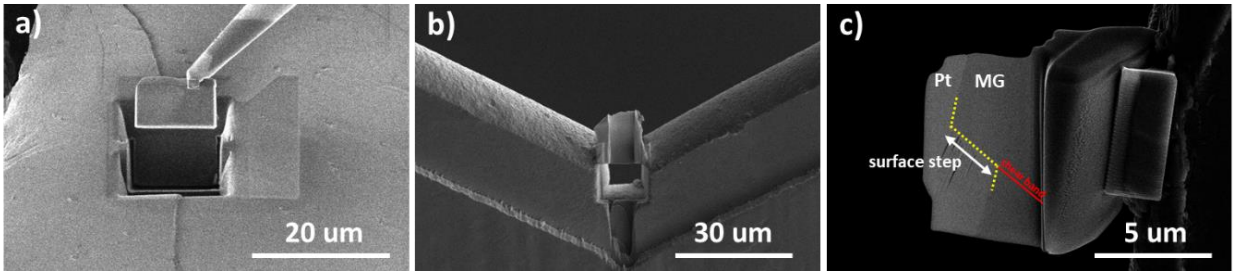

Figure 2.6. a) TEM specimen lift out from the bulk sample. b) SEM image of thinned TEM lamella mounted on a wide-post TEM grid. c) SEM image of a thinned TEM lamella mounted on a narrow-post TEM grid.

Overall, 28 lamellae lift out from the Vit105 compressed rods (9), Vit105 bending bars (14), and $Zr_{65}Cu_{25}Al_{10}$ compressed rods (5) were confirmed in the TEM to contain shear bands, and most of those TEM images were used for shear-band thickness and density change analysis, as described in Section 2.2.1. One TEM lamella was also used for TEM-based nano-beam diffraction experiments and synchrotron-based X-ray fluorescence mapping as described in Section 2.2.3 and 2.3.1, respectively. This lamella was kindly made by Dr. Vladimir Roddatis at the University of Goettingen. Ten of the specimens extracted from the Vit105 bending bars were intentionally left thick for making atom probe samples, as described in Section 2.1.4.

2.1.4 Atom probe tomography sample preparation

Two methods were used to prepare the needle-shape atom probe tomography (APT) samples. The standard site-specific wedge lift-out method outlined in Reference [182] was used first because it allowed batch production of APT needles from a single FIB lift out. A schematic of the wedge lift-out method is depicted in Figure 2.7. Firstly, the shear band must be identified on the surface of an MG sample, which involved drawing an imaginary line that connected two nearby surface cavities, as shown in Figure 2.4b. Then a Pt protection layer was deposited on top of the shear band, along the direction of this shear band, which was different from the TEM lamella preparation method (Section 2.1.3). The approximate orientation of the shear band in the wedge

sample is shown in Figure 2.7a, and it might not be exactly vertical to the sample surface. After the wedge-shape sample was lift out, it was rotated so that the shear band lied roughly horizontal, as shown in Figure 2.7b and Figure 2.7c. It was then moved to the APT post, and a section was attached to the flat APT post by Pt welding. Then the section attached to the APT post was detached from the rest of the wedge, and the same procedure was repeated to weld more sections of the wedge to other APT posts. Since the shear band remained unobservable throughout the FIB preparation process, this standard method did not provide the exact location of the shear band. In the case where the shear band orientation was not exactly horizontal on the rotated wedge, as shown in Figure 2.7b, it was possible to mill the shear band away when sharpening the APT needle. A very rare case where a cavity was found on a sample is shown in Figure 2.8a, which is a side view of the cut-off section of a lift-out wedge like the schematic shown in Figure 2.7a, and the shear band should lie on the same line as the cavity.

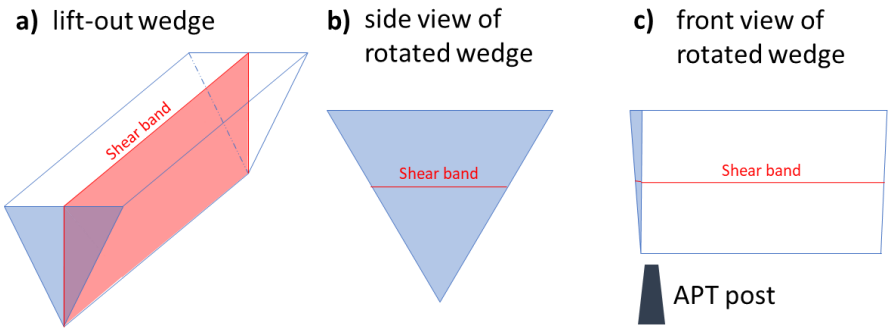

Figure 2.7. a) Shear-band location relative to the wedge-shape lift-out sample. b) Approximate shear-band orientation after rotating the lift-out wedge. c) Front view of the rotated wedge before welding a section of it on an APT post.

An alternative method was developed to better target the shear band location but could only produce one or two APT needles from each lift-out sample. This alternative method started with the same FIB lift-out technique described in Section 2.1.3, having the shear band roughly lying perpendicular to the ion beam and welding the lift-out sample to a narrow-post grid. Then part of the lift-out sample was thinned to an electron-transparent lamella, and the other part was

left thick for making one or two APT needles, as shown in Figure 2.8b. The thinned part was used first for TEM imaging to confirm the existence and location of the shear band, which should extend to the thick part of the sample at the same location. Then the part used for TEM was milled away, and the thick part remained on the APT post for sharpening.

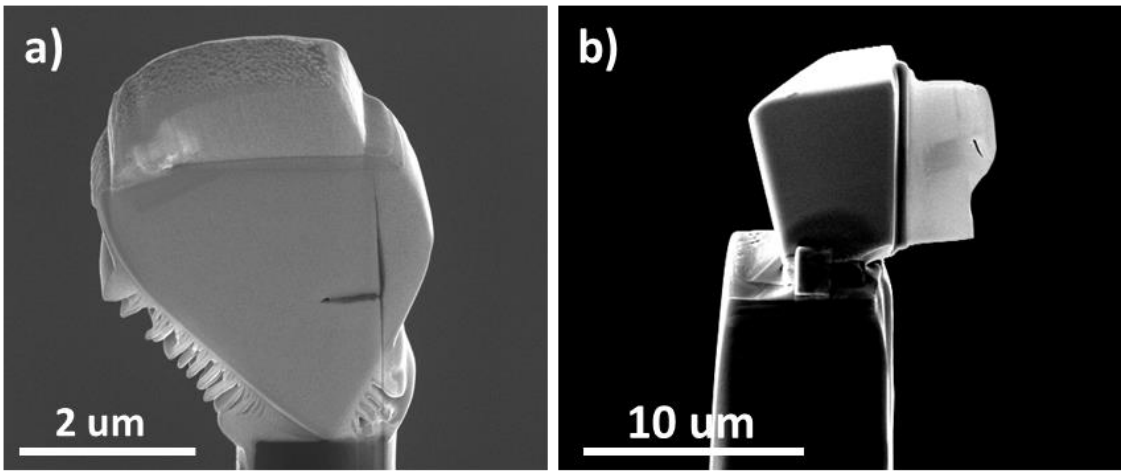

Figure 2.8. a) Side view of the cut-off section from a FIB wedge liftout welded to the APT post. A cavity is visible lying horizontal in the middle of the sample, serving as a shear-band location marker. b) A MG sample mounted to the APT post with one side thinned for TEM imaging of the shear band and the thick part left for APT needle sharpening.

Two types of APT posts were used in this work. The first type was a thin W wire wrapped in a Cu holder, which was custom made by Dr. Wei Guo at Oak Ridge National Laboratory [124]. This type of APT post held one APT needle at a time and required a custom-design TEM holder for viewing the APT needle in the TEM. An SEM image of the W wire holder is shown in Figure 2.9a, and the design for its TEM holder is shown in Figure 2.9b. The APT sample was mounted on top of the W wire by first milling the top of the wire flat. The TEM holder was manufactured by the School of Chemical Sciences Machine Shop at the University of Illinois at Urbana-Champaign using stainless steel and was used successfully to mount all the W wire APT post in the TEM. The other type of APT post was developed after the first set of APT experiments were finished and commercially sold by Hitachi [183], which was made of Si and could hold up to five APT needles on one grid. An image of the Hitachi Nanomesh APT grid is shown in Figure 2.10.

The Hitachi grid was compatible with standard TEM holders since its shape was similar to the Cu TEM grids shown in Figure 2.5. In comparison to the W wire holders, it was easier to transfer the Hitachi grid between the FIB, TEM and APT holders without much risk of damaging the APT needle. For the second set of APT experiments, the newly developed Hitachi grids were used. An additional step before transferring the samples to the Hitachi posts was to mill the posts to a thinner shape (~5-10 µm) for a consistently sharp needle, as shown in Figure 2.11a.

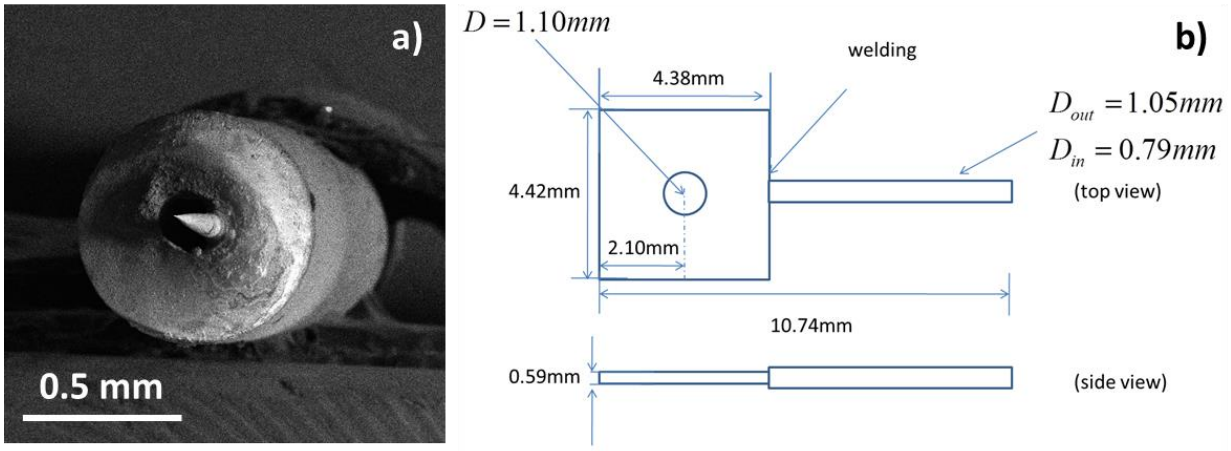

Figure 2.9. a) SEM image of a custom-made W wire APT post wrapped in Cu. b) Design of the stainless-steel holder that was used to hold the W-Cu APT post in the TEM.

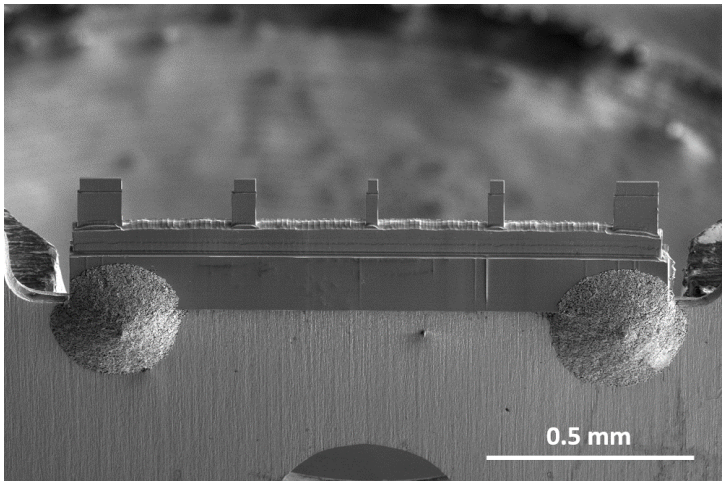

Figure 2.10. SEM image of Hitachi Nanomesh grid for correlative TEM and APT applications.

After the sample was attached on the APT post from both sides by Pt welding, it was ready to be sharpened into an APT needle using the ion beam. A circular milling pattern was used throughout the sharpening process, and it was critical to align the sharpest point of the needle with the center of the circular pattern at each milling step to avoid getting multiple peaks on a needle. A 30 kV 0.92 nA Ga ion beam was used to coarsely sharpen the sample into a shape similar to Figure 2.11a. Then the current was changed to 48 pA, and the circular milling pattern was set to have an outer diameter of 1.5 μm, an inner diameter of 0.17 μm, and milling depth (z) to 1.5 μm. The milling ion beam was kept this way until the shear band was roughly within 100 nm to 200 nm from the tip of the needle. A final 2 kV 89 pA beam was used to clean the APT needle until the shear band was 20 nm to 100 nm away from the tip. The final tip dimeter should be about 50 nm in order to initiate the field-evaporation process. An example of a sharpened APT needle is shown in Figure 2.11b, and the shear band is not visible in the SEM image. It was necessary to have the shear band within 100 nm from the tip, because there was increasing chance of fracturing the APT needle as ions farther away from the tip were extracted by the electric field during the evaporation process and the shear-band region should be evaporated before fracturing the needle. Also, note that the tip of the needle was constantly being milled away, so the shear band position must be measured using an unchanged reference marker, and the Pt-MG interface due to welding was the best reference.

Overall, three sets of APT experiments were conducted: one at CAMECA, with the help from Dr. Yimeng Chen, and the other two at Oak Ridge National Laboratory, with the help from Dr. Jonathan Poplawsky, Dr. Wei Guo, and Mr. James Burns.

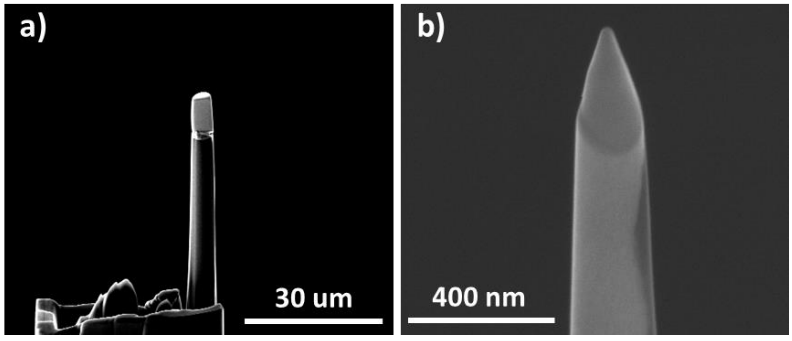

Figure 2.11. a) SEM image of a coarsely sharpened APT needle mounted on a Hitachi APT post. b) SEM image of a sharpened APT needle.

2.2 Transmission electron microscopy techniques

The TEM lamellae and APT specimens were imaged via the high-angle annular dark field scanning transmission electron microscopy (HAADF-STEM) technique. HAADF-STEM provided mass-thickness contrast that was used to quantify the density change ($\Delta\rho$) between the shear band and the MG matrix material [95, 96, 98]. Shear-band thickness (w) values were also extracted from the HAADF-STEM images. The insensitivity to imaging conditions were verified, and the effect of tilting the shear band relative to the direction of the incident electrons in the TEM were also analyzed and minimized. Additionally, scanning electron nano-beam diffraction (SEND) and energy dispersive X-ray spectroscopy (EDX or EDS) were used as complementary characterization methods to probe the structural and compositional differences between the shear band and the matrix. This section introduces the basic theoretical background for the HAADF-STEM, EDX, and SEND techniques. The experimental results obtained using the HAADF-STEM, EDX, and SEND techniques are presented in Sections 3.1, 3.2.1, and 3.2.2, respectively.

2.2.1 High-angle annular dark field scanning transmission electron microscopy

When electrons pass through an electron-transparent TEM lamella, the electron wave can change its amplitude and its phase. Both types of change will create image contrast, and the

selected imaging condition determines the type of contrast that dominates, which allows the TEM image to provide details on the material structure of interest. The contrast controlled by the change of electron phase is mainly useful in high-resolution TEM for atomic-scale imaging, which is not used in this work. On the other hand, amplitude contrast can result from variations in mass or thickness or a combination of both, and such mass-thickness contrast is the primary source of contrast in amorphous materials [184, 185]. Another form of amplitude contrast is diffraction contrast, which is used to study the structure of crystalline materials and is not applicable to amorphous materials. Therefore, mass-thickness contrast was the selected contrast mechanism to observe the shear bands in MGs [95, 96, 98].

Mass-thickness contrast can be understood taking electrons as particles. The electrons are scattered off by elastic nuclear interactions, or Rutherford scattering, as they pass through the TEM lamella. Consequently, high-mass regions, which are regions with heavy elements (high Z, so mass-thickness contrast is also called Z-contrast), high density, high thickness, or a combination of those, will scatter more electrons by elastic nuclear interactions. Out of these scattered electrons, the ones that are scattered to high angles (semi-angle > 50 mrad), which are incoherently and elastically scattered, can be collected by the high-angle annular dark field (HAADF) detector, and the intensity of these scattered electrons are only dependent on the mass and thickness of the material [184], which explains the reason for using the HAADF-STEM technique to obtain mass-thickness contrast images.

Moreover, what was the advantage of using the HAADF-STEM technique in comparison to other imaging techniques? Dark field images taken in the STEM mode are formed by collecting the elastically scattered electrons in the annular dark field (ADF) detector (10-50 mrad) or the HAADF detector (50-150 mrad), depending on the collection semi-angle. ADF-STEM and

HAADF-STEM images are less noisy than TEM dark field images, because an objective lens is not used to form the STEM image. A TEM dark field image is formed by permitting only a fraction of the scattered electrons to pass the objective aperture and suffers from aberrations, while STEM images do not suffer from aberrations. Also, STEM mode offers the flexibility to vary camera length, which changes the collection angle of the dark field detector, similar to varying objective apertures in the TEM but with more options. This variation in camera length allows the operator to maximize the ratio of the number of scattered electrons hitting the dark-field detector to the number of electrons passing the hole in the center of the detector. Dark field images in STEM mode thus give better contrast than those in TEM mode. For quantitative analysis of mass-thickness contrast, only electrons collected by the HAADF detector are used in order to exclude any coherently scattered electrons that land in lower angles. HAADF-STEM was thus the most accurate imaging technique for studying the density difference between the shear band and the matrix material using mass-thickness contrast. A schematic of the HAADF-STEM technique is illustrated in Figure 2.12 with α_0 > 50 mrad. Another method to cross check the density change is by nano-beam diffraction, which is described in Section 2.2.3. However, that technique would involve collecting and analyzing much more data if the same size of area was measured.

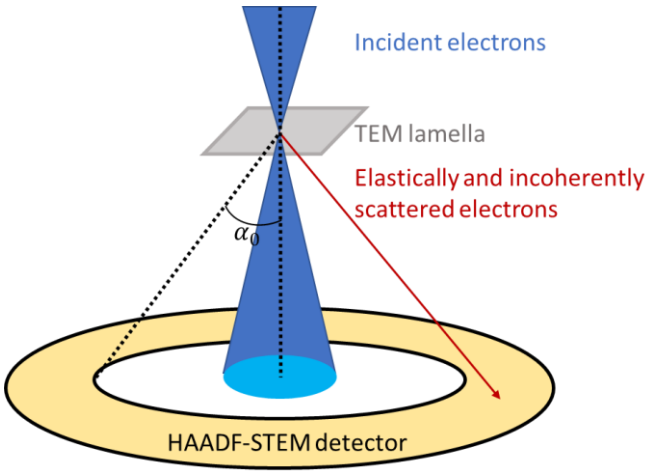

Figure 2.12. Schematic of the HAADF-STEM imaging technique.

To calculate the density change between the shear band and the matrix, start by assuming that n_0 electrons are incident on the TEM lamella, n electrons are transmitted through the center hole of the HAADF detector without being detected, and dn electrons are collected by the HAADF detector. After passing through dx amount of material, the reduction in the number of electrons going through the hole is expressed as

$$\frac{dn}{n} = -N\sigma dx, \tag{2.1}$$

where $N = N_A/A$, N_A is Avogadro's number, A is the average atomic weight of the probed area on the TEM lamella, σ is the total Rutherford scattering cross section, and $x = \rho t$, which is the mass-thickness of the lamella, where ρ is the density and t is the lamella thickness. Integration of Equation 2.1 gives

$$\ln n = -N\sigma x + \ln n_0, \tag{2.2}$$

and rearranging yields

$$\frac{n}{n_0} = e^{-N\sigma x}, \tag{2.3}$$

which would create a bright field image. The number of scattered electrons that form the HAADF-STEM image is then

$$1 - \frac{n}{n_0} = 1 - e^{-N\sigma x}. \tag{2.4}$$

Therefore, the HAADF-STEM image intensity can be written as

$$\frac{I}{I_0} = 1 - e^{-\frac{\rho t}{x_k}}, \tag{2.5}$$

where x_k is the contrast thickness defined as $A/(N_A\,\sigma)$ and can be calculated using

$$\frac{1}{x_k} = \frac{4}{Zx_{el}}\left[\frac{Z-1}{4\left[1+\left(\frac{\alpha_0}{\theta_0}\right)^2\right]} + ln\sqrt{1+\left(\frac{\theta_0}{\alpha_0}\right)^2}\right]. \tag{2.6}$$

The derivation of Equation 2.6 can be found in Reference [185] and the calculation of x_k is written in detail in Appendix A, where Z is the average atomic number of the probed alloy, x_{el} is the elastic contrast thickness, θ_0 is the characteristic angle of the scattered electrons (electron trajectory change due to elastic interaction with the nucleus) , and α_0 is the minimum scattering angle for the inner ring of the HAADF detector at a given camera length (shown in Figure 2.2.1). For Vit105 MG, x_k is ~650 μg cm^{-2}, ρ is ~6.6 g cm^{-3}, and t is ~100 nm. The value of $\rho t/x_k$ is thus very small (~0.1), so Equation 2.5 can be simplified using small-argument approximation:

$$\frac{I}{I_0} \approx \frac{\rho t}{x_k}. \tag{2.7}$$

The relative density change between the shear band and the matrix material can be calculated using Equation 2.7 as

$$\Delta\rho = \frac{\rho_{SB} - \rho_M}{\rho_M} = \frac{I_{SB} t_M x_k^{SB}}{I_M t_{SB} x_k^M} - 1, \tag{2.8}$$

where the subscripts "SB" and "M" stand for shear band and matrix, respectively. Since the variations of lamella thickness (t) and contrast thickness (x_k) between the shear band and the surrounding matrix are negligible, the above equation can be simplified to

$$\Delta\rho = \frac{I_{SB}}{I_M} - 1, \tag{2.9}$$

in which only the shear-band intensity (I_{SB}) and matrix material intensity (I_M) on a HAADF-STEM image contribute to the calculation of the shear-band density change compared to the matrix.

Representative HAADF-STEM images taken using a JEOL 2010F TEM are shown in Figure 2.15, Figure 2.17, and Figures 3.1a-d. The shear bands appear darker than the matrix in these HAADF-STEM images because the shear bands scattered less electrons to high angles. Since the lamella thickness and average atomic number of the shear bands and their surrounding matrix

areas were approximately the same, the shear bands must have a lower density than the surrounding matrix.

To efficiently extract the thickness and density change data, scripts were written in MATLAB, where a box was first defined around a shear band and then scanned along the shear-band path. Examples of defined boxes are shown in Figures 3.2a and 3.2c. Note that the images of shear bands were always rotated orthogonal to the scanning direction of the defined box so that the measured shear-band thickness was not projected from an angle. An example of the intensity profile averaged in the scan direction of a box is depicted in Figure 2.13. The typical intensity profile plotted as blue crosses in Figure 2.13 was smoothed using the locally weighted linear regression method (the *lowess* method in MATLAB *smooth* function with a smooth parameter of 0.1, which means the number of local data points used to compute each locally weighted linear regression is 10% of the total number of data points). The smoothed data are shown in red dots in Figure 2.13. The average maximum intensity and average minimum intensity were taken from the smoothed intensity profile. The maximum and minimum intensities correspond to the matrix material and the shear-band intensities (I_M and I_{SB}), respectively, which allowed the calculation of density change from the matrix to the shear-band material using Equation 2.9. Halfway between the maximum and minimum intensities is the intensity at FWHM (full width at half maximum), as shown in Figure 2.13. The intersection of the smoothed intensity profile and the intensity at FWHM defined the thickness of the shear band.

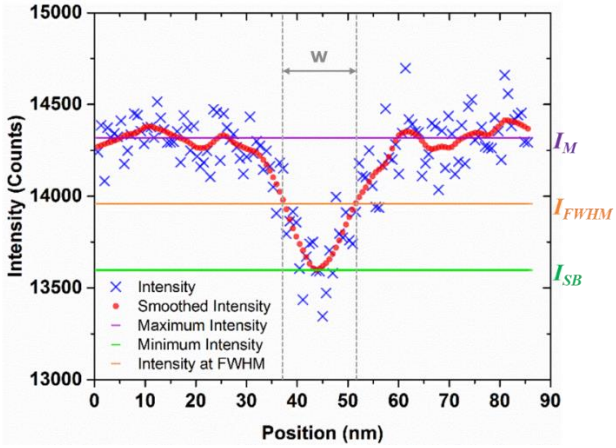

Figure 2.13. A typical HAADF-STEM intensity profile across a shear band.

The error bars for shear-band thickness and density change resulted from the mismatch between the smoothed and the raw intensity profiles. As seen in Figure 2.13, the intensity at the FWHM (I_{FWHM}) intersects the two intensity profiles at different positions, causing uncertainty in the actual thickness of the shear band. To calculate the difference in intersection position, the ideal method would require using the raw data and the smoothed data at the exact FWHM. However, the two scattered datasets (raw and smoothed) often did not intersect with the FWHM line, and the FWHM was also an estimated value involving errors. Trials involving fitting both datasets with Gaussian and polynomial functions and calculating the difference in intersection with the FWHM line were tested without having success on all the images and needed adjusting the fitting parameters manually during each loop, which slowed down the process significantly. The most efficient way to define the thickness error that worked for all the images and roughly matched the difference in intersection position was to define a range in the smoothed dataset within 3 to 5 data points above and below the FWHM line, and subtract the left-most point from the right-most point on each side of the intersection. The average of the two values on each side was used as the shear-band thickness error.

Similarly, the maximum and minimum intensities of the raw intensity profile did not always overlap exactly with the averaged intensities of the smoothed data, which resulted in errors in the density change values. The maximum and minimum values of the smoothed intensity data were identified (*max(ys)* and *min(ys)*), and a range of a few data points above and below those values were used to calculate the average maximum and average minimum of the intensity data. Those average values represented I_M and I_{SB}. Then the maximum and minimum values of the raw intensity data were identified (*max(y)* and *min(y)*), and the difference between *max(ys)* and *max(y)* along with the difference between *min(ys)* and *min(y)* were used in the error propagation equation below to define the error bar for $\Delta\rho$:

$$\text{error}(\Delta\rho) = |\Delta\rho|\sqrt{\left(\frac{\max(\text{ys})-\max(\text{y})}{I_M}\right)^2 + \left(\frac{\min(\text{ys})-\min(y)}{I_{SB}}\right)^2}. \tag{2.10}$$

In addition, different box heights were defined and tested to scan along a shear band, since the box height determined the number of pixels used to compute the average HAADF-STEM intensity values. An example of such test consisted of 4 box heights: 410 pixels, 256 pixels, 205 pixels, and 171 pixels, labeled in order as "box size 1" to "box size 4" in Figure 2.14. The test showed that the shear-band thickness values and the density change values did not depend much on the defined box size, so it was not necessary to unify the box size for all the shear-band images.

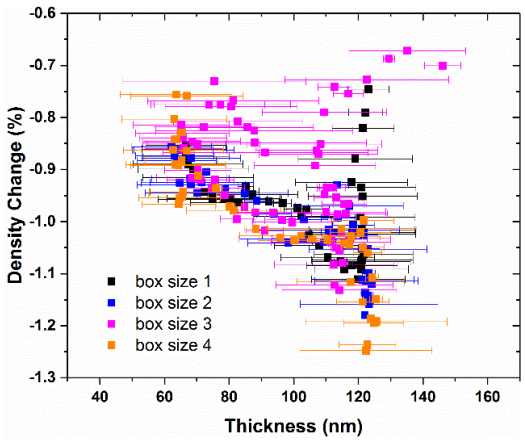

Figure 2.14. Plot showing that the calculated shear-band thickness and density change data do not depend on the defined box heights in the analysis.

2.2.2 Imaging condition tests

Although the calculation of shear-band density change only depends on the HAADF-STEM image intensity values on the shear-band and the matrix regions (I_M and I_{SB}), shown in Equation 2.9, variations in imaging conditions were tested to confirm the insensitivity to these conditions and to minimize their effect for the most accurate results. The tested imaging conditions were: camera length, acquisition time, and stage tilt.

A TEM specimen containing a shear band extracted from a Vit105 sample was imaged using three camera lengths and the same acquisition time. The HAADF-STEM images are shown in Figure 2.15. To exclude beam damage effect, the images were taken chronologically with camera length of 12 cm, 15 cm, and 10 cm. The density change values measured at different camera lengths plotted in Figure 2.16 show no significant difference within error margins, which confirms their insensitivity to camera length variations using the HAADF-STEM imaging technique. Camera lengths of more than 15 cm were not tested because they approached the ADF imaging condition.

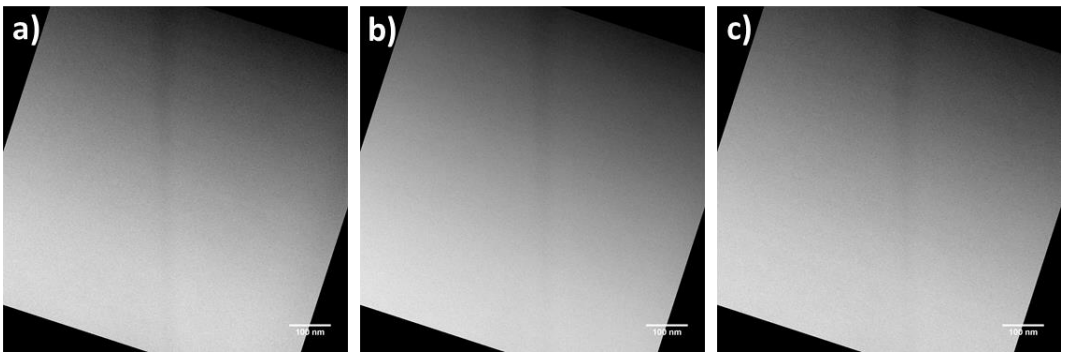

Figure 2.15. HAADF-STEM images taken on the same shear band at different camera lengths: 10 cm, 12 cm, and 15 cm in the order from a) to c).

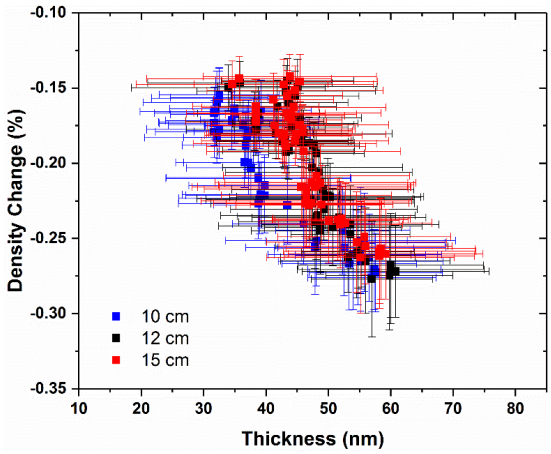

Figure 2.16. Density change and shear-band thickness values measured at different HAADF-STEM camera lengths.

Another Vit105 TEM lamella containing a shear band was imaged using 15 cm camera length with different acquisition times, or time per pixel. Variations from 10 second/pixel to 50 second/pixel were used. These HAADF-STEM images are shown in Figure 2.17. The density change values in relation to the thickness of the shear band are shown in Fig 2.18. Since the density change values from all acquisition times fall within the -0.6% to -1.2% range, these values were not affected by the variation in image acquisition time.

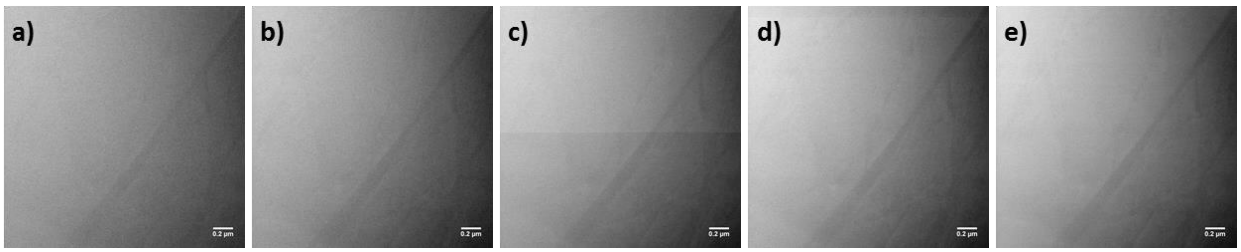

Figure 2.17. HAADF-STEM images of a shear band taken at the same camera length for different amounts of acquisition time: 10 second/pixel to 50 second/pixel in the order from a) to e).

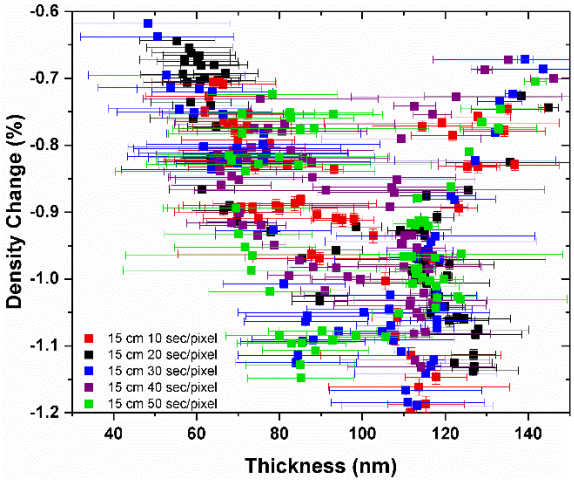

Figure 2.18. Density change and shear-band thickness values measured with different acquisition times.

The TEM lamellas were also imaged at different stage tilts, and the maximum contrast between the shear band and the surrounding matrix material was identified as the edge-on imaging condition. Figure 2.19 shows the variation in shear-band thickness and density change for different tilting conditions of a TEM lamella. With increasing misalignment between the incoming electron beam and the shear-band plane, the magnitude of density change decreased and the thickness increased while the error bars increased significantly. This was the expected trend, because a tilted shear band relative to the viewing axis would appear thicker in a projected 2D image and the HAADF-STEM contrast would blur out as more matrix material was included in the projection of the tilted shear band. A tilt with respect to the incoming electron beam direction resulted in a less well-defined shear band and therefore larger error bars for the shear-band thickness. In the particular case depicted in Figure 2.19, a zero tilt angle was found as the optimum stage tilt condition.

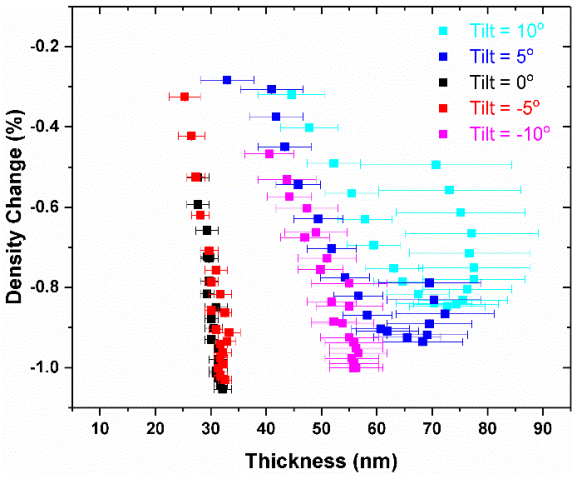

Figure 2.19. Density change as a function of shear-band thickness derived from the HAADF-STEM images. Different stage tilts for the TEM lamella are shown, indicating that a zero tilt corresponds to an edge-on view onto the shear band.

2.2.3 Scanning electron nano-beam diffraction and energy dispersive X-ray spectroscopy

The average interatomic spacing of a MG sample can be measured by diffraction techniques, providing structural insights of the material. Limited by the large probe size, most diffraction techniques, like lab-based XRD, can only average over a bulk volume of the sample. For example, the XRD data shown previously in Figure 2.1d that was used to verify the amorphous structure of an as-cast MG had a millimeter probe size, which could not at all resolve the structural difference between the nano-scale shear-band core and the matrix. Using a TEM-based scanning electron nano-beam diffraction (SEND) technique, which could generate a probe size (at its FWHM) as small as ~2 nm, the shear-band material (>10 nm in thickness) and the matrix material could easily be mapped separately, allowing for structural differentiation of the two materials that can also validate the results obtained using the HAADF-STEM method (Section 2.2.1). Nevertheless, the underlying mechanism to probe the average interatomic spacing in MGs is the same for the XRD and SEND techniques. For crystalline materials, their long-range periodic structure of atoms allows strong scattering of particles (X-rays, i.e. photons, and electrons) that generate intense diffraction peaks corresponding to specific atomic planes. The exact interplanar

spacing can be calculated directly using the well-known Bragg's Law [186]: $q = |\vec{q}| = \frac{4\pi sin\theta}{\lambda} = \frac{2\pi}{d_{hkl}}$, where θ is the half angle between the incident particles and the diffracted particles (usually expressed in the full angle 2θ on XRD plots), λ is the wavelength of the incident beam of particles, and d_{hkl} is the interplanar spacing that can also be expressed in reciprocal space using the magnitude of the scattering vector $\vec{q}$. For amorphous materials, which lack long-range atomic order, scattering is weak and spread out, so no sharp peaks are seen in their diffraction data (e.g., only a broad peak in the MG XRD data shown in Figure 2.1d). Instead, all values of $\vec{q}$ (or 2θ) are present on a MG diffraction plot, which means there is no distinguishable d_{hkl} that comes from constant interatomic spacing like in crystals. Therefore, to quantify the atomic structure of MGs, only an average value can be used. The average interatomic spacing (i.e., average spacing of the first coordination shell) is quantified using the first peak of the structure factor, which can be found as the q-position of the first broad peak in a q-dependent intensity plot. In the case of TEM-based electron diffraction, the first broad peak of a q-dependent intensity plot is found by summing electron diffraction ring patterns along the full azimuth (360°). A broad diffraction ring, instead of sharp intensity spots from crystal diffraction, serves as an indication of the amorphous atomic structure. Examples of TEM-based diffraction rings taken from Vit105 MG samples are shown in Figures 3.1d and the inset of 3.12, and the averaged intensity profiles are shown in Figure 3.13. Similar to the calculation of crystal interplanar spacing using the Bragg's Law, the average interatomic spacing of a MG can be estimated by $\frac{2\pi}{q}$, where q is at the first broad peak in a q-dependent intensity plot and sometimes also written as q_1 [179]. The experimental results using the TEM-based SEND technique are presented in Section 3.2.2.

In addition to the local structural information collected using the SEND technique, local chemical information can also be mapped in the TEM using energy dispersive X-ray spectroscopy (EDX or EDS), which is a common and standard method in SEM and TEM machines to identify and quantify the elemental compositions of a sample. EDX works by letting high-energy electrons ionize atoms, during which an inner-shell electron is ejected from an atom, leaving a hole in the shell [184]. The ionized atom prefers to return to its ground state, so a cascade of electron transition takes place, with each transition filling the hole with an electron from an outer shell. The last electron eventually falls into a hole in an inner shell from the conduction band. Each transition either emits a characteristic (fluorescent) X-ray or an Auger electron, depending on the fluorescence yield. The characteristic X-rays have a well-defined energy for each element and are detected by an energy dispersive detector, which is a solid-state device that discriminates among X-ray energies. Since the characteristic X-rays are unique to each element, they can be used to identify the elemental composition in a sample, and the intensity of the characteristic X-rays is directly related to the quantity of the identified element that has emitted it. A representative spectrum showing characteristic X-ray peaks from a Vit105 MG TEM lamella is shown in Figure 3.7b.

It is interesting to note here that a TEM lamella should be thinner for obtaining high quality SEND data and thicker for obtaining enough EDX signal, especially when using a nano-scale electron beam which does not ionize a large number of atoms to give sufficient counts of the characteristic X-rays. Hence, prioritizing one technique for the same TEM lamella and the same shear-band location on it would affect the data quality for the other technique, unless extra FIB thinning could be done, which would increase the risk of damaging the lamella and permanently losing the area of interest. For this work, the priority was to obtain structural information using the

SEND technique so that the density difference between the shear band and the matrix measured using the HAADF-STEM method could be verified. Therefore, the TEM lamella that generated useful SEND data was not thick enough to create sufficient EDX signal, and the EDX results should only serve as a qualitative indicator of the compositional difference between the shear band and the matrix. In other words, when using TEM-based EDX, it is not realistic to achieve good spatial resolution and high characteristic X-ray intensity (high signal-to-noise ratio) at the same time. However, only a TEM lamella could precisely show the location of the nano-scale shear-band core, so it was reasonable to use TEM-based EDX for qualitative compositional observation in this work. The EDX results are summarized in Section 3.2.1. A more quantitative description for understanding the EDX method can be found in Section 2.3.1, where a similar X-ray fluorescence technique was used to obtain much higher signal-to-noise ratio for quantitative data analysis.

2.3 Synchrotron-based X-ray techniques

Synchrotron-based nano-beam X-ray fluorescence (NB-XRF) experiments were conducted to study the difference in elemental distribution between the nano-scale shear-band core and the matrix in a Vit105 MG lamella. Phase-contrast X-ray tomography (XRT) was used to reconstruct internal shear-band cavities into full 3D view from deformed $Zr_{65}Cu_{25}Al_{10}$ samples that were unloaded prior to fracture. This section gives a brief overview of the NB-XRF and XRT techniques. The experimental results obtained using the NB-XRF and XRT methods are presented in Sections 3.2.1 and 3.5, respectively.

2.3.1 X-ray fluorescence

A 1 μm × 1 μm area (Figure 3.8) including both matrix and shear-band materials was mapped with NB-XRF at Beamline 26-ID at the Advanced Photon Source (APS), Argonne National Laboratory. A 9 keV monochromatic X-ray beam with a spot size of 30 nm was used to map the area. The combination of a nano-scale probe size and the high photon flux from the synchrotron source was the key reason for using this technique. As discussed earlier in Section 2.2.3 for TEM-based EDX, good spatial resolution and high fluorescence yield (characteristic X-rays) are both desired at the same time in order to resolve the nano-scale shear band and obtain high signal-to-noise ratio for quantitative compositional analysis. Although the spot size of the NB-XRF technique was an order of magnitude larger than the probe size used in the TEM-based EDX technique, it was small enough to resolve thick shear bands (~100 nm). On the other hand, the high photon flux from synchrotron-based NB-XRF that went through the sample was able to generate characteristic X-rays several orders of magnitude more than those obtained from TEM-based EDX, as readily seen when comparing the intensities on Figure 3.7b (EDX spectrum) and Figure 3.9 (NB-XRF spectrum).

NB-XRF and EDX follow the same mechanism. An atom irradiated with X-rays that have enough energy to knock out an inner-shell electron will generate a hole, and an outer-shell electron undergoes de-excitation to fill the hole in the inner shell, emitting fluorescent (characteristic) X-rays that corresponds to the energy difference between the two shells and are unique to each element. The possible electron transition between two shells (energy levels) is determined by the selection rules of quantum mechanics. Figure 2.20a shows a schematic of an energy-level diagram for various electron shells of an atom. When the incident X-ray creates a hole in the K (L) shell, the resulting fluorescent X-rays are the K- (L-) series X-rays. The K-series X-rays are commonly

used for their conveniently reachable energies and high emissions, except for high-Z elements (e.g., for Zr in this work, L-series fluorescent X-rays are used). The fluorescent X-ray intensity $I_{j,k}^{i}$ from element *i* for monochromatic incident X-rays is given by [187]:

$$I_{j,k}^{i} = \varepsilon F_{j,k}^{i} C_i [1 - \exp(-\rho t A)] \frac{\mu_{i\lambda} I_0(\lambda)}{A \sin\alpha}, \tag{2.11}$$

where $A = \frac{\mu_{S,\lambda}}{\sin\alpha} + \frac{\mu_{S,\lambda i}}{\sin\beta}$, $I_0(\lambda)$ is the incident photon flux, λ and λ_i are wavelengths of the incident X-ray and fluorescent X-ray, respectively, $F_{j,k}^{i}$ is the emission probability of the *k*th fluorescent X-rays in the *j*th shell, C_i is the mass concentration of the probed sample, ρ is the sample density, α and β are the incident and exit angles of incident and fluorescent X-rays, respectively, t is the sample thickness, ε is the geometrical factor of the detector, $\mu_{i\lambda}$ is the mass absorption coefficient of the element i at wavelength λ, and $\mu_{S,\lambda}$ and $\mu_{S,\lambda i}$ are the mass absorption coefficients of the matrix at wavelength λ and λ_i, respectively. Figure 2.20b summarizes the parameters in Equation 2.11 in a schematic sample. Equation 2.11 shows that the fluorescent X-ray intensity is linearly proportional to C_i and $I_0(\lambda)$, so it is essential to use a high $I_0(\lambda)$ synchrotron-based probe. The non-destructive, high-precision NB-XRF technique can be used for quantitative analysis for almost all the elements from Na to U, and the elements of interest in this work are Zr, Cu, Al, Ti, and Ni. The NB-XRF results are presented in Section 3.2.1.

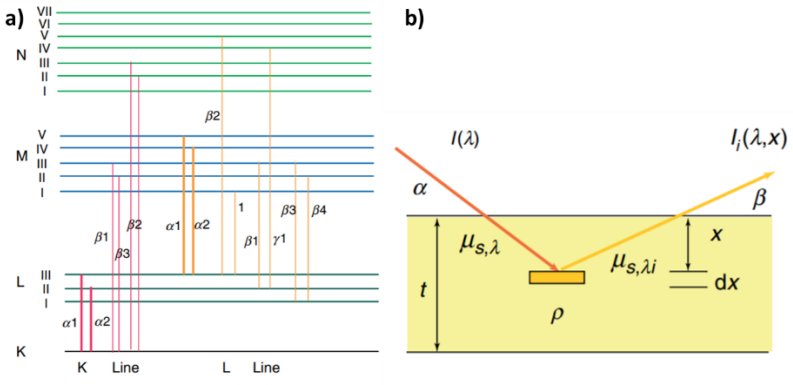

Figure 2.20. a) Energy level diagram for the K and L emission spectra. b) Schematic sample parameters for the calculation of fluorescent X-ray intensity using Equation 2.11. a) and b) are adapted from Reference [187].

2.3.2 X-ray tomography

Synchrotron-based XRT was performed at beamline 1-ID at the APS to observe the distribution of internal cavities that locate in the shear-band region in compressed MG samples prior to failure. The micron-size internal cavities could be detected with a phase contrast mechanism [188-190]. The behavior of X-rays as they pass through a material can be described using a complex index of refraction: $n = 1 - \delta - i\beta$, where *n* deviates only slightly from unity, β describes the absorption of X-rays by the sample, and the phase-shift term δ is related to refractive effects. As high-energy X-rays pass through a sample, the phase-shift term can be several orders of magnitude higher than the absorption term, making it possible to observe phase contrast when absorption contrast is undetectable. When X-rays pass through regions in the sample with abrupt changes in refractive index (i.e., boundaries between regions of different electron densities), the wave front of the X-rays will become distorted and cause interference patterns on the detector plane placed a given distance behind the sample. Therefore, interfaces between shear-band cavities and the MG-matrix could be detected and visualized in the bulk sample. As opposed to absorption-contrast, phase contrast only relies on the refraction of X-rays, so imaging can be done at higher energies, reducing the absorbed dose and providing a non-destructive internal observation to a given sample.

A 90.524 keV monochromatic X-ray beam was defined by a series of slits to form a 1.5 mm (horizontal) × 0.8 mm (vertical) rectangle incident on the sample, which is the size of the field of view. This high X-ray energy ensured enough transmitted intensity for detection through the samples and sufficient intensity resolution to provide the best phase contrast between the matrix material and shear-induced deformation features. The pixel resolution of the imaging detector was 0.75 μm/pixel, and the theoretical optical resolution is 1.5 μm. Taking into account the chosen

beam energy, scintillator blooming, optical distortions, detector distance, beam divergence, and mechanical instability, the estimated true spatial resolution was ~2 µm. Since the samples used in this work were several times larger than the field of view, separate segments were scanned first, one field of view at a time, with some overlap in between for reconstruction alignment, as shown in Figure 2.21. The sample was rotated over 360° during each scan and then translated either vertically or horizontally for another scan. The X-rays transmitted through the sample then passed through a scintillator and were imaged onto the charge-coupled device (CCD) by a long-working distance objective, and in addition to the probe size and detector resolution, the distance of these downstream components relative to the sample also govern the resolution of this technique. Further details on the XRT method used here are provided in References [191-194]. The XRT scans from each field of view were stitched together and reconstructed into 1152 slices of 2D images per sample using the GRIDREC algorithm [191, 192]. The stitching and reconstruction were done at the APS by Dr. Peter Kenesei. Examples of the reconstructed 2D images are shown in Figures 3.23a-d. The 2D images for each sample was then processed to remove reconstruction artifacts and stacked into 3D, with the details and results presented in Section 3.4.1.

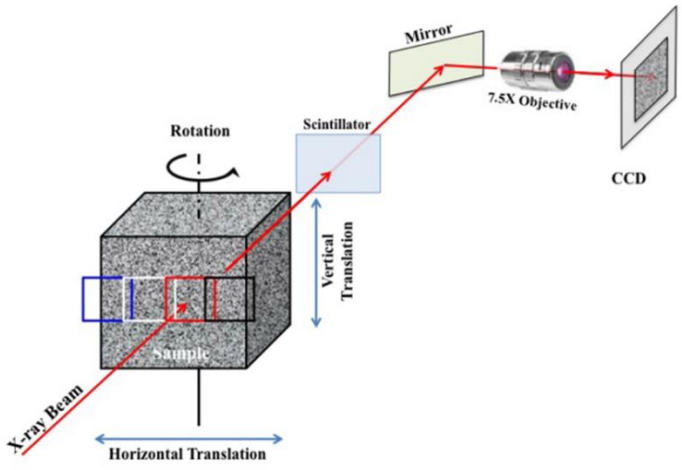

Figure 2.21. Schematic from Reference [193] of the XRT setup used at Beamline 1-ID at the APS.

2.4 Atom probe tomography

Atom probe tomography (APT) is an atomic-level materials characterization technique that collects atomic coordinates and mass-to-charge-state ratio atom-by-atom, allowing the reconstruction of atomic distribution in a solid specimen in 3D [195]. Since APT is a 3D structural and chemical imaging technique, it is complementary to the HAADF-STEM and X-ray fluorescence techniques described in Section 2.2 and Section 2.3.1, which used averaged 3D signals into 2D.

APT evolved from a field ion microscope equipped with a time-of-flight mass spectrometer in order to chemically identify each atom [196]. In order to extract the atoms one at a time, the atom must be removed from the apex (tip) of the specimen in the form of ions using field evaporation [197], during which the atom first transitions to an escape charge state and then to a higher final charge state through post-field ionization before reaching the detector. The escape step is considered to be a thermally activated process that depends on the temperature (T) and the atom-probe operating field (evaporation field) at the tip of the specimen (F), so the evaporation rate (k_n) is given by $k_n(F,T) = Ae^{-\frac{Q_n(F)}{k_B T}}$, where Q_n is the barrier for escape, k_B is the Boltzmann constant, and A is a constant often taken as equal to the surface-atom vibration frequency. The field evaporation emission equation for the effective operating flux is thus [195]:

$$R = nk_n(F,T) = nAe^{-\frac{Q_n(F)}{k_B T}}, \tag{2.12}$$

where n is the count of surface atoms at the tip of the specimen that are highly prone to be evaporated. Note that $F = \frac{V}{kr}$, where V is the total applied voltage (usually constant), k is a geometrical factor (usually ~3-5), r is the radius of the specimen tip (increasing as more atoms are removed from the specimen apex) [198]. To achieve a high F at constant V at the tip of the

specimen, a small tip radius is required, but r will keep increasing during an experiment until F is not large enough to evaporate ionized atoms and the experiment comes to a stop, assuming no fracture occurs due to mechanical stress induced during the process. Specimen fracture is quite common for brittle materials and not so problematic for the MG specimens used in this work, unless an APT specimen is not well made during the FIB process or large voids exist in a specimen.

The first generation 1D atom probe evaporated atoms from a sharp needle specimen as ions by applying a positive voltage in high vacuum, and the second generation, developed in the 1980s, introduced a position-sensitive single atom detector that drastically increased the lateral field of view to 10-20 nm, containing millions of atoms. The latest generation of APT uses a local electrode atom probe (LEAP), commercially introduced in 2003, adding a local electrode close to the specimen. A schematic of LEAP is shown in Figure 2.22, where a positive voltage is applied to the cryogenically cooled sharp needle specimen and the pulsed laser triggers the evaporation of atoms. Laser pulsing has the advantage of applying less mechanical stress to the specimen to delay fracture for a longer evaporation process, because field evaporation is only enabled during the heat pulse. The local electrode enables lower amplitude standing voltages and further increases the field of view. The large microchannel plates embed fast delay line single atom detectors. In an APT dataset, the x and y atomic coordinates are given by the impact position of each ion, which are derived from the delay lines $x = t_2 - t_1$ and $y = t_4 - t_3$, respectively (Δt is the time from the evaporation pulse to the recorded impact time), as shown in Figure 2.22. The z coordinate is the order of atoms collected on the detector. A high pulse repetition rate (>200 kHz) should be used in order to minimize acquisition time and preferential evaporation on the standing voltage [199].

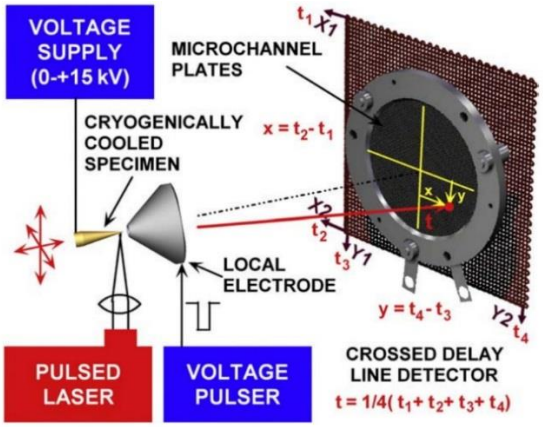

Figure 2.22. Schematic from Reference [199] of an APT (LEAP) system.

APT data from $Zr_{65}Cu_{25}Al_{10}$ and Vit105 MG specimens were collected by a CAMECA-LEAP 4000XR 3D microscope operated at a voltage pulse mode of 200-250 kHz pulse rate and 15-75 pJ pulse energy with a detection rate of 0.3-0.5% at a base temperature of 25-60 K. The APT reconstruction for compositional analysis was conducted by Dr. Jon Poplawsky at Oak Ridge National Laboratory and Dr. Yimeng Chen at CAMECA. The APT results are summarized in Section 3.3.

CHAPTER 3: RESULTS AND DISCUSSION

This chapter presents the results of the experimental work and the corresponding analysis and discussion of the results. The order of the sections in this chapter flows from the structure and chemical composition analysis of nano-scale shear bands to the visualization of micron-size cavities on shear bands and a discussion of their effect on the mechanical properties of MGs. This chapter contains the works published over the course of this research, which are listed in References [98, 174, 175] with Reference [200] to be submitted.

3.1 Nano-scale shear-band morphology, thickness and density change

The foundational work started with probing the nano-scale thickness variation and volume dilatation along a major system-spanning shear band in a Vit105 ($Zr_{52.5}Cu_{17.9}Ni_{14.6}Al_{10}Ti_5$) MG that has carried ~6% macroscopic plastic strain in uniaxial compression. Four representative HAADF-STEM images are shown in Figures 3.1a-d, and Figure 3.1e shows a diffraction pattern over an area where an HAADF-STEM image was taken. The diffuse diffraction rings confirm the amorphous state of the MG TEM specimens. The shear bands appear darker than the matrix in these HAADF-STEM images because the shear bands scattered less electrons to high angles, implying that the shear bands have a lower density than the surrounding matrix. Based on the observations from the six TEM specimens, two kinds of shear-band morphologies were defined ad hoc purely based on this experimental work. The first kind had a diffuse morphology, where many shear bands branched out in various directions as shown in Figure 3.1a. The second kind was a single and isolated shear band, as shown in Figures 3.1c and 3.1d. Figure 3.1b displays a shear-band segment on the transition from a diffuse morphology to an isolated band. The diffuse shear bands located near a cavity, while the isolated single shear bands located farther away from

cavities. This agreed with earlier observations that reported time-dependent formation of diffuse shear-bands structures near cavities as a result of plastic processes that relieved internal residual-stresses [97].

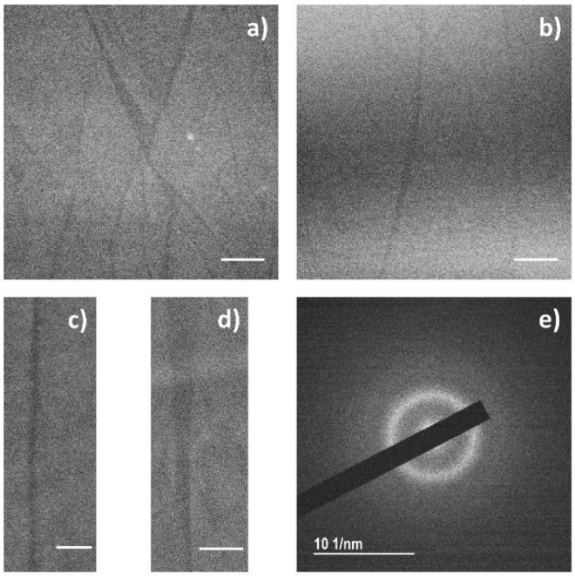

Figure 3.1. a) - d) HAADF-STEM images of shear bands. e) Representative diffraction pattern taken from one of the TEM specimens. Scale bars: a), b), c) are 100 nm, and d) is 300 nm.

To acquire the shear-band thickness values and density changes with respect to the surrounding matrix material, image analysis was done using MATLAB, and an example MATLAB script is presented in Appendix B. Consecutive boxes were defined in MATLAB and scanned along shear bands, as shown in Figure 3.2a and 3.2c, and each scan generated an intensity profile similar to that in Figure 2.13. Each intensity profile from a box gave the thickness and density change of a small segment along a shear band, and consecutive boxes generated plots like Figure 3.2b and 3.2d that tracked the thickness and density change along subsequent positions of a shear band. The data in Figure 3.2b and 3.2d were extracted from the shear bands in Figure 3.2a and 3.2c, respectively. While the shear-band thickness fluctuates up and down along the shear band in Figure 3.2a, the absolute amount of density change in percentage also fluctuates but

generally decreases, as shown in Figure 3.2b. On the other hand, while the thickness in Figure 3.2c decreases, the amount of density change fluctuates up and down, as shown in Figure 3.2d. Hence, no distinct correlation could be drawn between the thickness and the density change within several hundred nanometers length along a shear band.

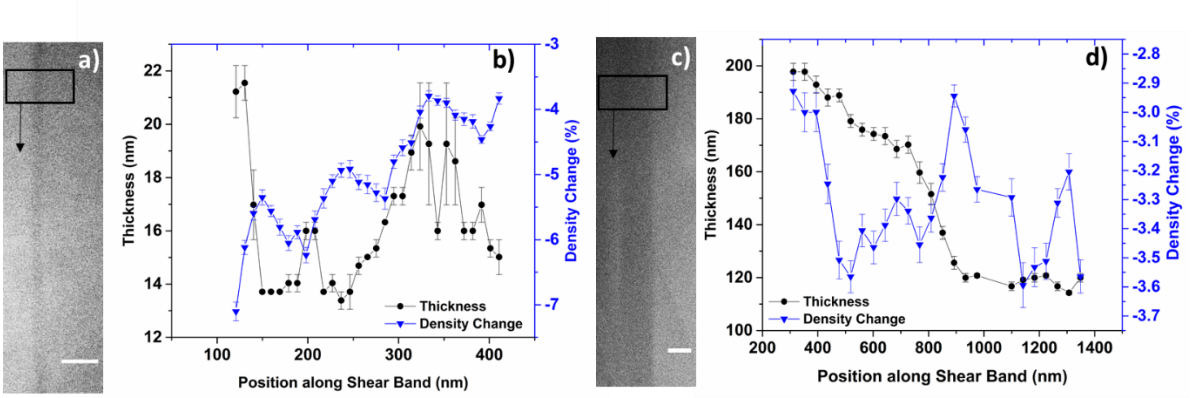

Figure 3.2. a), c) Representative shear bands with analysis boxes scanning in the vertical direction along the shear band to extract the data shown in b) and d), respectively. Scale bars: a) and c) are 100 nm.

A collection of TEM specimens made from the single system-spanning shear band in a uniaxially compressed Vit105 MG rod was analyzed to produce statistical distributions of shear-band thickness and density change relative to the matrix material, as shown in Figures 3.3a-b. The highest count of shear-band thickness belongs to the bin spanning 0-20 nm, as shown in Figure 3.3a, where the histogram has 11 bins of 20 nm each. However, much thicker shear bands also exist in non-negligible numbers within a bulk sample, with the thickest shear band of about 215 nm. With 12 bins of 1% density change each, Figure 3.3b shows that the highest count of density change was around -3% to -4%. Considerably higher values of -11% to -12% also existed. In addition, a density change vs. shear-band thickness plot summarizes all data in Figure 3.3c, where each color represents a different shear band. The diffuse and isolated shear bands are marked as triangles and filled circles, respectively. This summary plot further confirms that there was no correlation between shear-band thickness and density change for an individually analyzed shear-

band segment. In other words, a 20 nm thick shear band could range from being 4-7% less dense than the matrix (yellow circles in Figure 3.3c), and a shear band that was 3% less dense than the matrix spanned from 120 nm to 200 nm in thickness (red circles in Figure 3.3c). However, a global trend was observed from this summary plot, where the shear bands were drawn from locations several hundred micrometers apart. Although a thick shear band of more than 100 nm did not always achieve a large density change, they could be much less dense than the matrix (~12%), whereas thin shear bands never reached such a large density change. The highest density change of -12% was observed on a 165 nm thick shear band, and shear bands less than 100 nm thick did not exceed -9% density change for the sample investigated here. Moreover, although the diffuse and isolated shear bands had the same thickness range, the isolated shear bands never reached the extreme values of density change in this study. The fact of larger observed density changes near cavities may reflect a sensitivity to local tensile stresses or stress gradients that can have a similar character as in mixed mode I and II crack tips [97, 201].

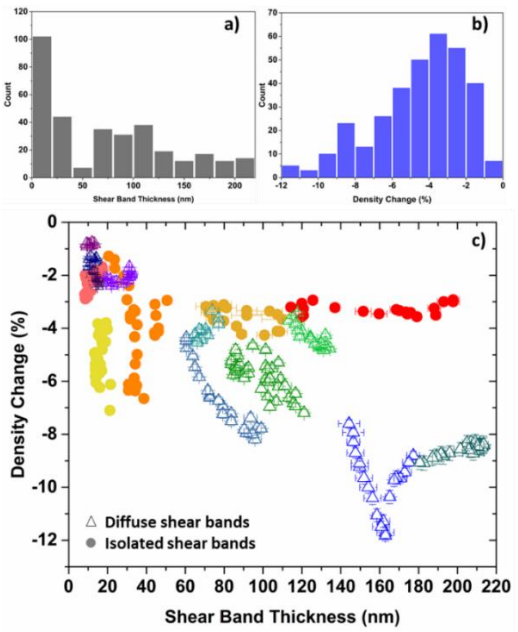

Figure 3.3. a) Histogram of shear-band thickness distribution. b) Histogram of shear-band density change distribution. c) Summary plot of density change vs. shear band thickness from 15 different shear-band segments in the same Vit105 MG sample.

Two nanoindentation arrays were used to generate hardness maps around the major system-spanning shear band, shown in Figures 3.4b and 3.4c. The hardness data are shown relative to the matrix value of H_0 = 8.45 GPa. Significant reductions in indentation hardness were seen along the shear-band path, and the apparent softening was attributed to residual stresses. More details of the nanoindentation hardness mappings can be found in Reference [97]. The shaded boxes in Figure 3.4a indicate where the nanoindentation arrays were taken relative to the shear band (dotted line) and visible surface cavities are also indicated in Figure 3.4a. After nanoindentation, a TEM specimen was extracted from each array location to observe the structure of the shear band. The two TEM specimens from both nanoindentation arrays were used to take the HAADF-STEM images shown in Figures 3.1a and 3.1b.

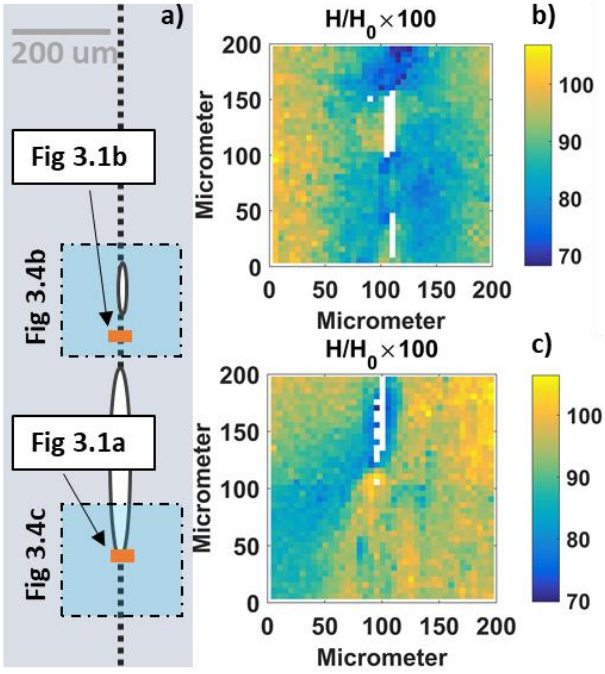

Figure 3.4. a) The two dashed boxes indicate the locations of two nanoindentation arrays that generated the hardness maps in b) and c), which correspond to the upper and lower dashed boxes, respectively. The locations of two TEM specimens, which were used to take HAADF-STEM images shown in Figures 3.1a and 3.1b, are also indicated as small orange rectangles in a). White areas in b) and c) correspond to the location of cavities shown in a).

There is a clear difference between the shear bands in Figures 3.1a and 3.1b in that Figure 3.1a contains many diffuse shear bands that branch out in all directions and vary in length and thickness while Figure 3.1b displays the transition to a distinct singe shear band, as displayed in Figures 3.1c and 3.1d. This was a consistent observation made for the studied sample, indicating that the major shear band was interrupted by cavities, and a complex diffuse shear-band structure formed at the end points of these cavities. The diffuse shear-band structure around cavities has been ascribed to time-dependent stress relaxation via strain localization that was triggered by internal stresses [97, 202]. Further away from the cavities, the major shear band appeared as a single line contrast in HAADF-STEM (Figures 3.1c and 3.1d).

Errors on shear-band thickness, shown in Figure 3.3a, could come from both data smoothing and experimental uncertainties. The errors from data smoothing are included in error bars for all the shear-band thickness data and discussed in Section 2.2.1. The TEM lamellae were also tilted at the best edge-on imaging condition to minimize projection error, as discussed in Section 2.2.2. However, another possible source of error was shear-band tilt in a different geometry during FIB liftout from the one mentioned in Section 2.2.2. Although it is shown in the schematics of Figure 2.4b and Figure 3.4a that the FIB lift-out sites for making the TEM lamellae are perfectly perpendicular to the shear-band line on the bulk sample surface, it is possible that the TEM lamella was slightly tilted by an angle α from the direction normal to the shear band, as drawn in the top-view schematic of the sample surface in Figure 3.5, where the horizontal orange areas indicate the FIB lift-out sites and the gray vertical stripe is the shear band. In this case, the projected shear-band thickness (w_p) from TEM imaging would not equal to the actual thickness (w_a) of the shear band. Note that the major shear band in the compressed Vit105 rod was confirmed to be perpendicular to the sample surface as shown in Figure 2.4c by imaging several cavities along the

shear-band line after milling trenches on the FIB. Therefore, the main source of shear-band tilt from the compressed rod sample could only come from the angle α from FIB lift-out orientation. On the other hand, the shear-band plane was not always perpendicular to the surface in the bending bar samples, so TEM stage tilt was always performed to obtain the most accurate shear-band thickness and density change values. In either case, the error generated from a possible misalignment in FIB lift-out is defined below with the schematic shown in Figure 3.5, where t is the TEM lamella thickness:

$$\frac{w_p(\alpha) - w_a}{w_a} = \frac{w_p(\alpha)cos\alpha}{w_p(\alpha) - t\ tan\ \alpha} - 1. \tag{3.1}$$

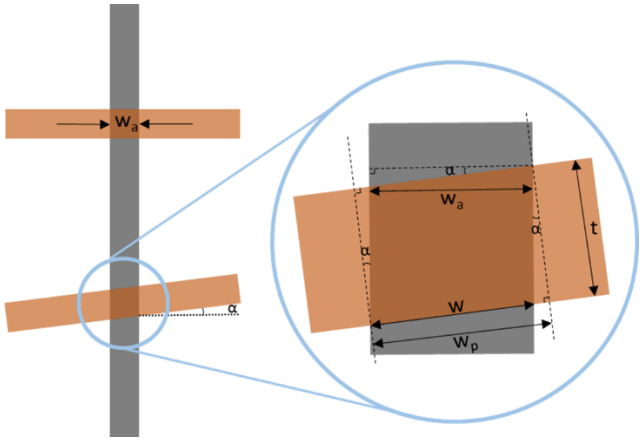

Figure 3.5. Schematic of a possible FIB lift-out misalignment with an angle α tilted from the shear band.

All the TEM lamellae used had ~100 nm thickness (t), and the maximum offset angle (α) from FIB liftout was observed to be less than 5°. Due to this offset angle, the actual shear-band thickness could only be smaller than the measured thickness projected on the TEM. On the low-value side of the shear-band thickness distribution, a TEM image showing a 20 nm thick shear band would have approximately 80% error if the offset angle were as large as 5°, which would make the real thickness of the shear band only 4 nm. Such small thicknesses were not seen in this work, but the possibility of their existence cannot be excluded if there was such an offset angle. On the high-valued side of the shear-band thickness distribution, a shear band with a 200 nm

projected thickness only had a 5% error for α=5°, which would make the actual thickness about 190 nm. Although a possible offset angle from sample preparation would lead to thicker shear bands in TEM projection, the 200 nm thick shear bands observed quite accurately determined the upper limit of the studied TEM specimens. Furthermore, since the TEM lamellas were ~100 nm thin, it was not possible to project a 20 nm thick shear band to 200 nm thick. The errors from the possible offset angle were also mitigated by taking the FWHM of the intensity profile instead of the projected thickness at the maximum intensity, as discussed in Section 2.2.1 (Figure 2.13). Since such small offset angles could not be precisely measured for each TEM lamella and the shear-band thickness was already reduced from the projected thickness to the FWHM of the intensity profile, no error bars relating to any potential offset angle were added to the shear-band thickness data. The offset angle could also affect the accuracy of the density change between the shear band and the matrix. Since the HAADF-STEM intensity was projected from 3D to 2D, having an offset angle would include some projection of the matrix material in the shear-band region. All shear bands revealed a negative density change, which means the surrounding matrix was denser. Any overlapping signal from both the shear band and the matrix would thus decrease the magnitude of the measured density change. It was therefore concluded that the density change values contained were at the lower bounds if such tilt was considered, which would be similar to the specimen tilt effect shown in Figure 2.19.

A large distribution of shear-band thicknesses was observed in this work, as summarized in Figure 3.3a, ranging from ~10 nm to 210 nm. This was quite a remarkable range compared to the aggregation of previously reported results, which had the general consensus of shear-band thickness values in the range up to 20 nm [120, 136], extracted from monolithic MGs deformed via uniaxial loading, bending, or cold rolling. Selected other studies involving high-pressure

torsion, high-strain, or other highly constrained deformation report values that extend beyond the 20 nm regime [169, 203, 204], but in those cases the broad shear bands had a fine structure of contrast, which makes their classification unclear. In the sample studied here, a single major shear band was introduced via compression, and it should be emphasized that the defect was well-developed, meaning that the distributions of properties (Figure 3.3) did not capture potential strain-dependencies, which is discussed later in Section 3.3. In fact, at the very early stage of shear-band nucleation and shearing, the spread found in shear-band thickness might be reduced and more in agreement with current computational insights. During deformation, the shear band underwent local detachment that led to the formation of cavities, as introduced in Section 1.2.3. Near the resulting cavities, a dense shear-band structure was observed, which was typical for a non-uniform stress state. Away from the cavities, the shear band appeared as an isolated line. However, along the probed segments of the isolated shear band away from the cavities, a similar large spread in shear-band thickness was found. That meant the shear-band thickness was position-dependent and might fluctuate considerably (here between 10 nm and 200 nm) along its path (Figures 3.2 and 3.3c), irrespective of the proximity to a cavity and its morphological distinction. Therefore, the measure of shear-band thickness was not a single value, but one must consider larger fluctuations of which the origin remains unclear. One important aspect of this position-dependent shear-band thickness is that any material property calculated on the basis of a shear-band thickness will sensitively depend on the very local measure of this value. Examples of such calculations may be temperature profiles [205], shear-band dilatation [66, 206], the maximum shear strain or flow rate [207], shear-band viscosity [165, 208] or the critical stress for shear-band nucleation [209, 210]. With the results presented here, such approaches will need to consider larger bounds, ascribing strongly varying properties to a well-developed shear band.

In addition to the large spread in shear-band thickness, the shear bands studied here revealed density changes ranging between -1% and -12%, as seen in Figure 3.3b and 3.3c. With the method of aligning the ion beam normal to the shear band, any potential TEM lamella thickness variations along the shear band was minimized. As in earlier work using the TEM [136], this density change was ascribed to a structural change imparted into the shear-band during inhomogeneous flow. Figure 3.3c suggests that a diffuse shear-band structure near cavities exhibit larger density changes covering the entire range to -12%, whereas isolated shear bands reach -7%. Since the overall range is well in agreement with earlier studies on both an $Al_{88}Y_7Fe_5$ MG [95] and Vit105 [122], there probably is not any specific density-change limit to the two types of shear bands, which reminds us that the shear-band morphology was anyhow an ad hoc classification.

How can such large changes in density at the nano-scale be understood? Assume that the determination of the density change is correctly represented by Equation 2.9. In this context, it is instructive to map the derived density changes on a volume-temperature graph, which is shown for Vit105 in Figure 3.6 based on literature values [211]. In Figure 3.6, the volume has been normalized to room temperature and represents the reference state. The two horizontal lines mark the normalized volume values at T_g and the transition between the supercooled liquid and the liquid regime (or the melting temperature).

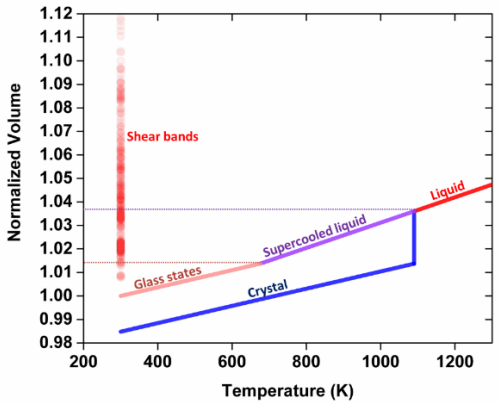

Figure 3.6. Graph comparing the obtained shear-band density changes with the normalized temperature-dependent volume of Vit105 based on literature values [211]. Constant mass is assumed.

Adding the data obtained from the HAADF-STEM images, which were all measured at room temperature, it is seen that some of the data points lie above T_g, extending above the transition to the liquid regime. About 43% of the shear-band density change values fall below the melting temperature. The representation in Figure 3.6 implies that the now structurally-frozen material resides in a state that volumetrically is similar to the supercooled liquid or the liquid. Clearly, this is hard to reconcile, and other reasons for such values need to be sought of. One possibility is the formation of sub-nm and nm-sized voids that are averaged over when recording the HAADF-STEM images. Evidence for such small voids was reported in References [128, 131], but other reports have not been able to confirm this [123, 133]. Of particular interest are the findings of Atzmon and coworkers [128] that show how the formation of low-density defects, interpreted as nanovoids, depend on the type of stress state under which the shear band had formed, as well as the type of glass. Since the TEM specimens studied here are ~100 nm thick, it is possible that (sub-) nm voids [131, 132, 169, 212] are actually hidden in the shear band, and probed in the direction of the electron beam. This could be one explanation of the sometimes strongly fluctuating density change seen along the shear-band path (Figure 3.2). Another reason could be chemical segregation, where the lighter elements replace higher Z-elements in the shear band. Since the HAADF-STEM methods fundamentally evaluates a mass contrast, chemical segregation in shear bands, as reported in Reference [95] via EDX, could also lead to an effective reduced density relative to the matrix. Experimental results that resolved nano-scale shear bands using chemical methods (EDX, NB-XRF and APT) are discussed in the following section.

3.2 Chemical segregation and volume dilatation of shear bands

As discussed at the end of the previous section, two possible reasons could explain the decreased density on the shear bands compared to the matrix material measured by the HAADF-STEM technique: i) chemical segregation and ii) structural dilatation. The difference in chemical composition between the shear band and the matrix material was probed by TEM-based EDX (Section 2.2.3), synchrotron-based NB-XRF (Section 2.3.1), and APT (Section 2.4). The structural difference between the shear band and the matrix was probed by SEND in the TEM (Section 2.2.3). This section provides the results collected by the techniques mentioned above and the relevant discussions relating to the origin of the decreased shear-band density. Since the resolution of the EDX, NB-XRF, and SEND methods are on the same nanometer length scale and the data collected using these methods average over the same TEM lamella into 2D, these results are presented first in Sections 3.2.1 and 3.2.2. The APT experiments had an atomic resolution and used different sets of samples, so the APT results are presented last in Section 3.2.3.

3.2.1 Compositional difference between the shear-band core and the matrix

The limited literature on shear-band structure and chemistry via direct experimental observation relies mainly on TEM techniques. While clear structural and chemical changes have been observed with crystallization inside shear bands [127, 129, 130], the available data for non-crystallized shear bands is limited to a few reports, that contain some indications for changes in chemistry [95, 126] or no change in chemistry [123, 125]. Much clearer is the situation for volumetric changes of the shear-band material relative to the matrix, which, dependent on the position along the shear band, reduce or increase in density [95, 96, 98]. The HAADF-STEM technique we used provides image contrast based on the average atomic number in the probed

volume. It is thus possible to obtain a contrast variation due to either a local change in density at constant chemistry, or due to a local change in shear-band chemistry. The primary objective of this study is thus to i) contribute to the inconclusive and scarce literature on shear-band structure and chemistry, and to ii) corroborate if density changes obtained with the HAADF-STEM method are unaffected by changes in average atomic number due to a local change in chemistry.

EDX was conducted using a FEI Themis Z advanced probe aberration corrected analytical STEM to measure the compositional difference between the shear-band and matrix materials using one of the Vit105 TEM lamellae analyzed in Section 3.1 that contained >100 nm thick shear bands. The EDX maps were scanned over 18 nm × 18 nm areas on the shear-band material and the matrix material separately using a probe size (FWHM) of ~2 nm with a scan rate of 5.1 second/pixel. The areas (A1 and A2) mapped with EDX are shown in Figure 3.7a, and the corresponding EDX energy spectra are shown in Figures 3.7b. The compositional difference between the two mapped areas was calculated by first subtracting the background, integrating the Ni-K_α and the Zr-L peaks in each spectrum, and then taking the difference of the integrated values for each element. EDX results revealed that the Ni and Zr concentrations at the probed shear-band region have reduced by 3.6% and 3.9%, respectively, compared to the matrix. The other elemental peaks, which are labeled in light blue in Figure 3.7b, were not used in the calculation. The reasons were: i) the TEM sample holder made of Cu might have contributed to the Cu signal, and ii) Al, Ti and Zr-K signals had low signal-to-noise ratio. Due to the limited overall signal-to-noise ratio of the EDX data, as discussed back in Section 2.2.3, NB-XRF was conducted to allow for quantitative analysis of the chemical segregation in the nano-scale shear band using the same Vit105 TEM lamella.

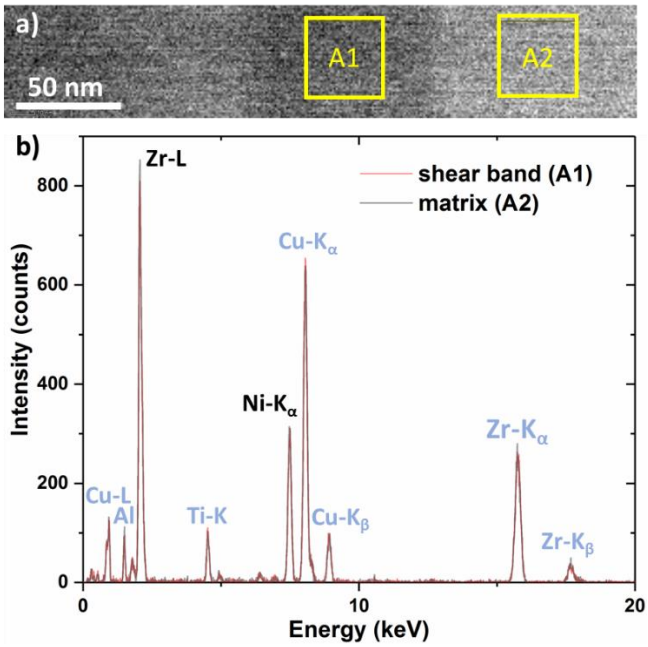

Figure 3.7. a) ADF-STEM image containing shear-band (dark) and matrix (bright) materials. A1 and A2 indicate the areas scanned to obtain EDX data. b) Background-subtracted EDX spectra of the shear-band and the matrix regions. The Zr-L and Ni- K_α peaks were used to calculate the compositional difference between the two regions.

A 1 µm × 1 µm area including both matrix and shear-band materials, as shown in the dashed box in Figure 3.8, was mapped with NB-XRF at Beamline 26-ID at the APS using a 9 keV monochromatic X-ray beam with a spot size of 30 nm. The full fluorescence map contained 41 × 41 positions, leading to an approximate 5 nm overlap in probed area from point to point. The signal was integrated for 95 seconds at each point, resulting in a total scan time of about 44 hours. The long scan time led to unavoidable stage drift that was corrected for during data analysis. The fluorescence signal was collected using a SII Vortex-ME4 SDD EDS 4-element detector. In addition to the NB-XRF signal, powder diffraction patterns with a *q*-range from 1.7 $Å^{-1}$ to 3.7 $Å^{-1}$ and the direct transmitted beam were collected at each scan position. Due to the insufficient scattering volume of the thin amorphous TEM lamella, the signal-to-noise ratio did not allow any further processing of those data, which are presented in Appendix C.

Figure 3.8a shows the color-enhanced HAADF-STEM image of a diffuse shear-band structure near the end-point of a shear-band cavity, and the dashed box indicates the area mapped

with NB-XRF. Color-enhancing was chosen to improve the visibility of the shear bands. The appearance of numerous shear-band segments near a shear-band cavity has been attributed to local plastic deformation due to a time-dependent relief of internal residual stresses [97, 202]. Figure 3.8b displays a zoom-in image of Figure 3.8a, where the area enclosed with dashed lines identifies the same area in both images. The wide vertical shear-band segment has a position-dependent width between ~100 nm and ~200 nm and was chosen for NB-XRF measurements because thinner shear bands were not resolvable using the 30 nm X-ray probe.

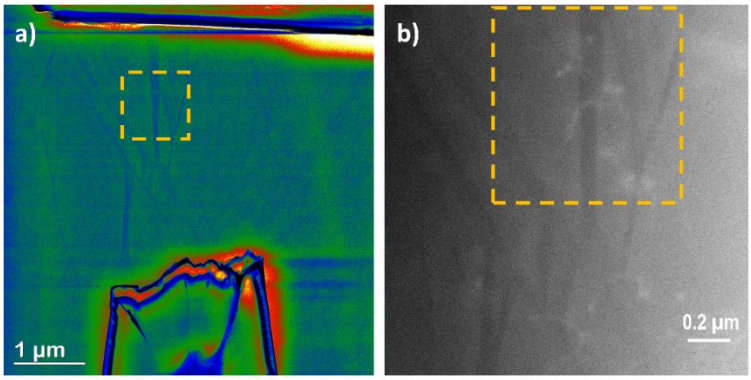

Figure 3.8. a) Color-enhanced HAADF-STEM image containing shear bands near a Pt-filled cavity. The color-scale ranges from blue to red, with red being the highest intensity of the image. b) Zoom-in HAADF-STEM image of a). The box on each images a) and b) indicates the area that is mapped with NB-XRF.

At each position of the NB-XRF map, a background-corrected fluorescence spectrum was obtained, as depicted in Figure 3.9. This representative XRF spectrum contains the X-ray emission peaks from all the elements in the TEM lamella, which are labelled above each peak. The peak generated by incident photons is also indicated at high emission energies. After background correction, the Ti, Ni, and Zr peaks were fit with a Gaussian function using MATLAB. Overlapping of neighboring fitted peaks was subtracted, and the remaining signal for individual elements was integrated. Al was not considered due to the poor signal to noise ratio, and the Cu-signal was discarded because of possible contributions from the Cu TEM grid (sample holder shown in Figure 2.5) used to mount the TEM lamella.

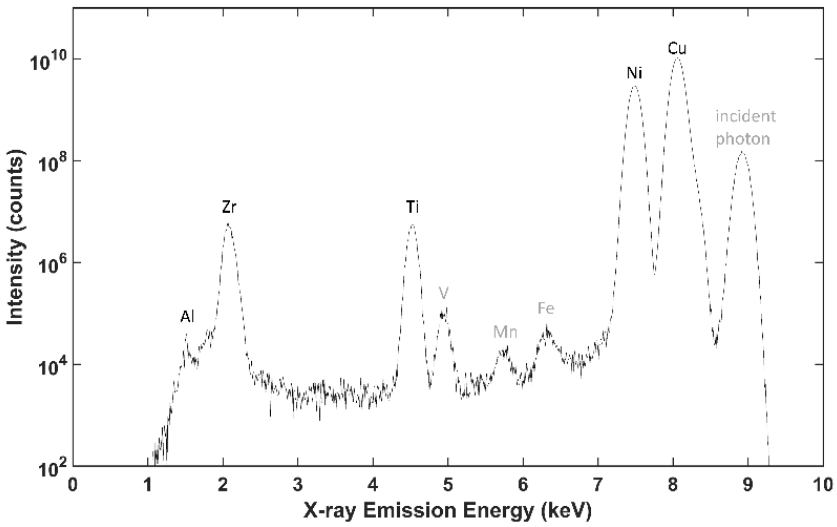

Figure 3.9. A representative X-ray fluorescence spectrum from a point measurement in the scanned area shown in Figure 3.8.

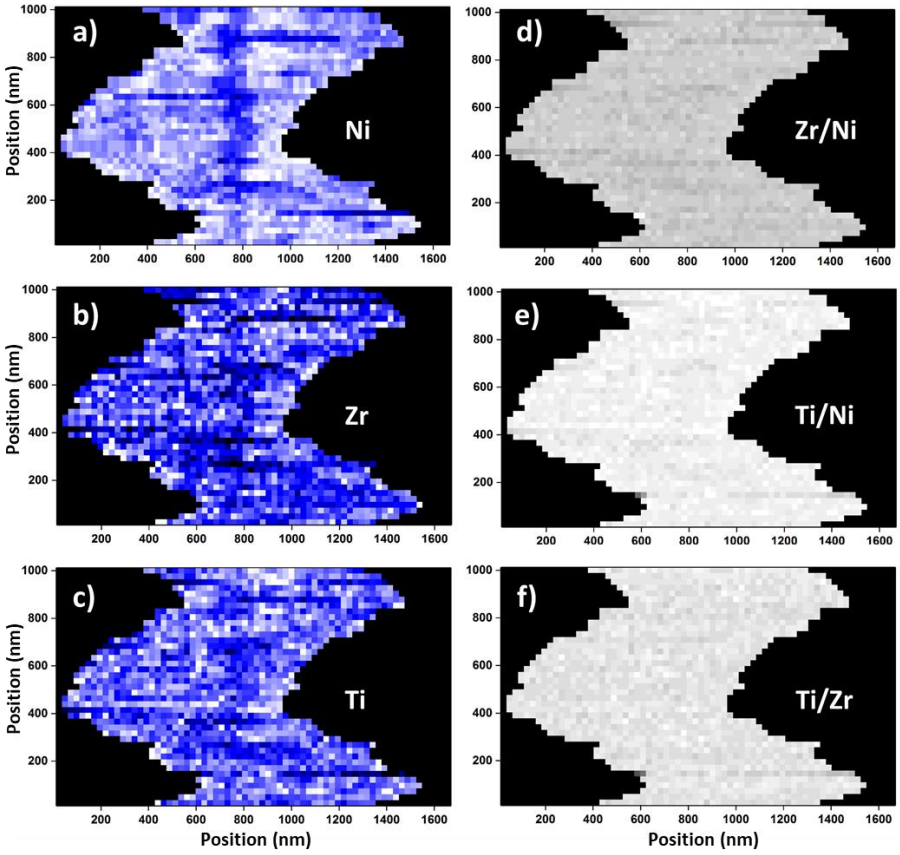

Figure 3.10. a) – c) Drift-corrected NB-XRF maps for individual elements, showing depletion of each element in the shear band. d) – f) XRF intensity ratio maps showing no chemical segregation.

The integrated intensities of each analyzed element were subsequently plotted in drift-corrected 2D maps, as shown in Figure 3.10a-c. The shifting left- and right-hand side border of the fluorescent maps is a consequence of the applied drift correction so that the shear band is adjusted to a straight line, based on its shape from the TEM image shown in Figure 3.8. In good agreement with the TEM-imaged shear-band segment displayed in Figure 3.8, the XRF contrast is oriented vertically. A clearly visible, but weak signal change is located in the central part of the XRF maps, which indicates chemical depletion in the region of the mapped shear band. To better quantify the change in chemistry suggested by the XRF maps, the information in Figure 3.10 was averaged and normalized across vertical lines for the range between 634 and 926 nm to produce intensity profiles across the shear band. The error bars of these intensity profiles represent the standard deviation of each vertical data column. Figure 3.11 summarizes these intensity profiles for Ni, Zr, and Ti, where the profiles have been shifted from a starting point of y = 1 to lower values in order to enhance the readability of the graph. These traces clearly suggest an elemental depletion of all three chemical species, which in the order of Ni, Zr and Ti are 1.7%, 2.1% and 2.4%, respectively. Larger error bars are observed for Zr and Ti in comparison to Ni, which finds its origin in the low XRF yield from the Zr L-edge, whereas Ti has the smallest percentage in the studied MG-alloy.

While the XRF maps and their normalized average intensity profiles indicate a chemical change within the shear band relative to the adjacent matrix, it is instructive to construct intensity ratios. This is motivated by the fact that local structural volumetric changes (dilatation or contraction) should lead to a uniform chemical signal across the XRF maps. This is indeed the case, as shown in Figures 3.10d-f, and consequently, the normalized average intensity ratio profiles (Figure 3.11) show no change in intensity across the shear-band location. This holds true for the

ratios Zr/Ni, Ti/Ni, and Ti/Zr. It is thus concluded that the change in the intensity profiles across the shear band seen in Figures 3.10a-c is purely due to the reduced density of the structure, which translates to a weak but resolvable intensity change in the XRF data. The density reduction for precisely the same shear-band segment can be obtained with HAADF-STEM under the assumption that the chemical composition is constant. This amounts to 5-7%, depending on position. It should be noted that both the XRF and the HAADF-STEM datasets rely fundamentally on signals that are sensitive to the number of atoms per probed unit volume and that differences in the detected signals from the two methods are expected due to numerous experimental factors, including the detector efficiencies, electron scattering and x-ray fluorescence yield, background corrections, etc. It is thus reasonable to find the same order of magnitude but numerically different values for the density change measured by HAADF-STEM and the chemical depletion quantified by NB-XRF on the same shear band.

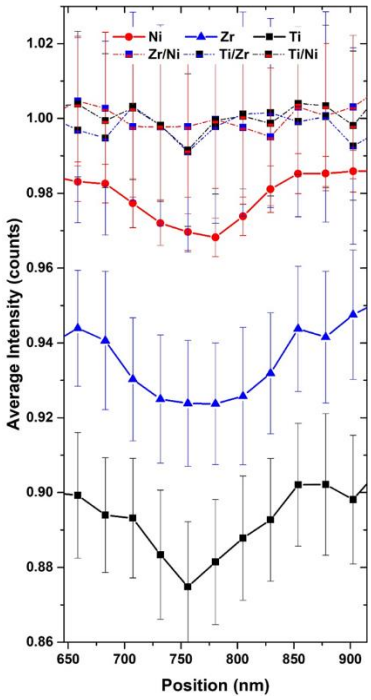

Figure 3.11. XRF intensity profiles averaged and normalized over all vertical columns for the range between 634 and 926 nm of the maps shown in Figure 3.10. To improve visualization, the different element-specific intensity profiles have also been shifted in the y-axis.

3.2.2 Structural dilatation of shear bands

In order to validate the finding that shear-band density reduction measured by HAADF-STEM and NB-XRF was purely due to structural dilatation, SEND was performed across shear-band segments using a FEI Themis Z advanced probe aberration corrected analytical STEM. The electron beam energy was 300 kV, and the probe size (FWHM) was ~2 nm with a semi convergence angle of 0.65 mrad. The shear-band material and the matrix material were mapped separately via SEND by recording diffraction patterns across specific areas of size 15 nm (h) × 45 nm (v). Since the original TEM lamella used for HAADF-STEM was too thick for SEND, it was thinned further using FIB. This thinning step created a hole in the TEM foil at the location of the shear-band segment analyzed previously, so a new HAADF-STEM image was taken from an adjacent location, which is shown in Figure 3.12.

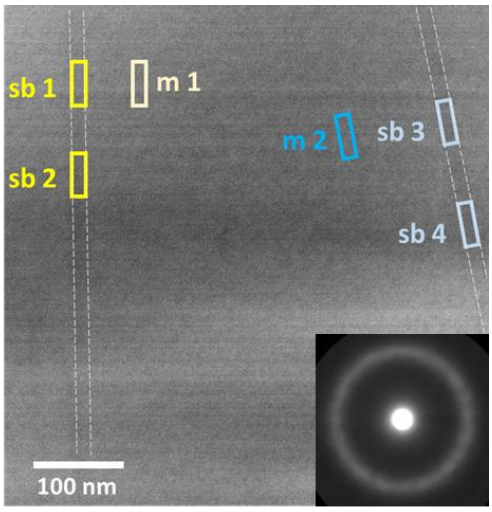

Figure 3.12. HAADF-STEM image with two shear bands that are highlighted with dashed lines. Areas mapped using SEND are indicated with boxes. The diffraction pattern is the sum of all diffraction patterns taken from the "sb 1" region.

Two shear-band segments are indicated with dashed lines in Figure 3.12, both of which were investigated with SEND at two different locations, marked with "sb1-sb4", where "sb" stands for shear band. The matrix, "m", was probed across the areas "m1" and "m2". A total of 75

diffraction patterns were recorded across each 15 nm × 45 nm scanned area marked by "sb1-sb4" and "m1-m2". An inset in Fig. 4a displays a diffraction pattern, which represents the sum of all 75 nano-beam diffraction patterns from the "sb1" region. Similar integrated diffraction patterns were obtained across the other regions marked in Figure 3.12, showing that crystallization did not occur in either the shear-band or the matrix.

Integrating the summed diffraction pattern along the full azimuth (360°) resulted in the q-dependent intensity profiles shown in Figure 3.13. At low q-values the high-intensity signal of the direct beam is seen, and the peak at $q \approx 2.6$ Å^{-1} is the first peak of the structure factor (q_1), which agrees with other x-ray diffraction and neutron diffraction data [179, 180]. It should be mentioned that in TEM, diffraction peaks are conventionally reported in k instead of q, where $k = q/(2\pi)$, and k_1 is around 4.2 nm^{-1} for a CuZr MG [213]. The inset of Figure 3.13 highlights the diffraction peaks from the MG, with the dashed lines representing those from the matrix material and the solid lines representing those from the shear-band material. After fitting the peaks with a Gaussian function in MATLAB, the q-peak positions for m1 and m2 are 2.623 Å^{-1} and 2.621 Å^{-1}, and those for sb1-sb4 are 2.619 Å^{-1}, 2.609 Å^{-1}, 2.603 Å^{-1}, and 2.603 Å^{-1}, respectively. Thus, the q-peak positions for the shear-band material are consistently smaller, which indicates an increased mean distance between scattering centers. This is qualitatively in agreement with the structural dilatation revealed via HAADF-STEM. A scaling relationship between q_1 and the atomic volume ($v_a = M/(N_A\rho_m)$, where ρ_m is the mass density, N_A is Avogadro's number, and M is the molecular weight) was reported for metallic glasses as: $q_1 \cdot v_a^{0.443\pm0.007} = 9.3 \pm 0.2$ [179]. Using this relationship, one can calculate the decreased density in the shear bands compared to the matrix, which is -1.7%. The density difference between the shear band and the matrix shown in Figure 3.12 was additionally quantified with the HAADF-STEM method (Section 2.2.1), which yields ~3% density reduction

in the shear band, which aligns well with the calculated density change by the aforementioned scaling relationship, thus validating the structural dilatation probed by HAADF-STEM.

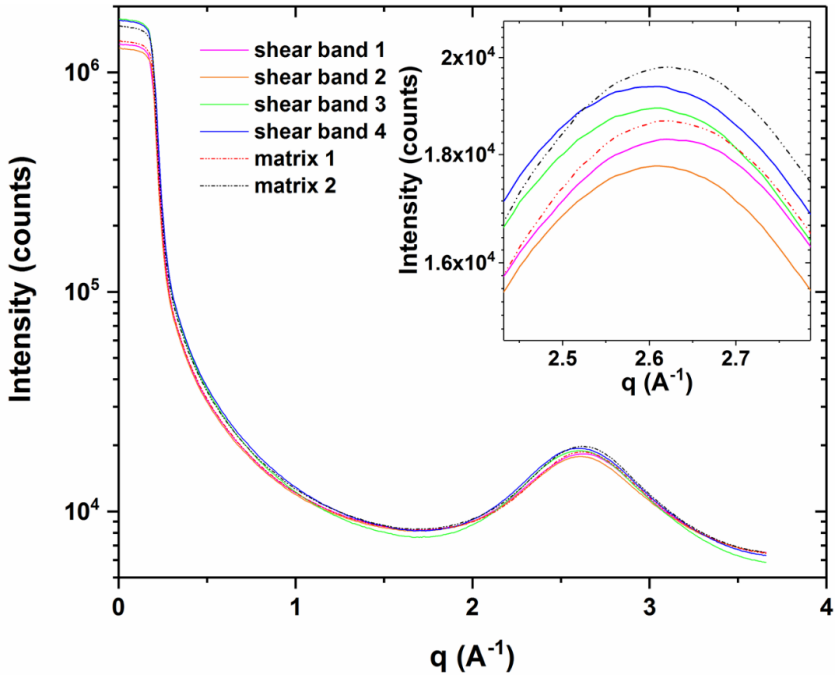

Figure 3.13. Integrated intensity profiles from all diffraction patterns obtained in the different regions marked in Figure 3.12. The inset is a zoom-in view of the first peak (q_1).

In summary, this work presents strong evidence that strain localization into shear bands in the Vit105 MG studied here does not cause any changes in local chemistry. This finding is limited to shear bands in which no shear-induced crystallization can be resolved. It is shown that local probing of the shear-band chemistry can result in signals that suggest a depletion of a given element, but this likely is due to the volume dilatation of the shear-band material. It is thus the reduced number of atoms per probed unit volume that causes the apparent elementary depletion. The combined XRF, EDX and SEND results presented in this section therefore corroborate the fact that the density reductions measured with HAADF-STEM, as also reported in Section 3.1, are unaffected by any change in the local shear-band chemistry.

3.2.3 Atomic-scale observation of the shear-band core

There are very few reports in the literature that experimentally studied the nano-scale shear-band core structure using the atomic-resolution APT technique. Marquis and coworkers have recently shown that the density reduction of the shear band relative to the matrix led to an inverted density contrast due to the different evaporation fields for the shear band and the matrix [125], which means that a positive density change measured with APT can actually be a negative change. This measurement therefore supports qualitatively the density decrease in the shear band but does not allow quantitative insights due to problems associated with the reconstruction of the evaporated material. It is important to note that the density of the specimen could also be affected by ion-trajectory aberrations and local magnification effects. Thus any apparent density change in the shear band measured by APT may not be accurate. Such artifacts produced in the APT could make the detection of shear bands ambiguous using the APT technique alone. Therefore, correlative TEM and APT work was necessary to study the density variation and chemical changes in shear bands and the MG matrix, which was the experimental plan for this work. Additionally, in contrast to the chemical segregation detected by TEM-based EDX (Section 3.2.1 and References [95, 174], most APT experiments have so far not shown chemical differences between the shear band and the matrix [123-125] with an exception of Reference [126]. The reports mentioned above have in common that they did not relate the structural state of the shear band with the amount of global or local plastic strain mediated by the shear band, which can possibly affect the glassy structure and chemistry in the shear band. This work thus attempted to link the macroscopic engineering strain and local shear strain with the shear-band structure probed by correlating the HAADF-STEM and APT methods.

The first batch of samples consisted of three bulk $Zr_{65}Cu_{25}Al_{10}$ MG rods that were uniaxially compressed to 1%, 2%, and 4% macroscopic plastic strains, unloaded prior to fracture, and polished to a cuboid shape for a smooth surface for FIB lift-out of APT specimens along the shear-band path, as outlined in Section 2.1.4. The bulk MG rods are shown in Figure 3.14, all of which have been confirmed as amorphous using XRD. The 1% plastic strain sample did not show cavities along the shear-band path after polishing; the 2% plastic strain sample showed no more than two visible cavities after polishing; and the 4% plastic strain sample had three visible cavities after polishing. The cavities served as indicators of the shear band for the 2% and 4% plastic strain samples and eased the FIB lift-out process when trying to target the location of the nano-scale shear-band core. For the 1% plastic strain sample, it was unclear if the nano-scale shear band has been included in the lift-out wedge, since the wedge lift-out method did not provide much room for error and the nano-scale shear band could not be seen during the FIB lift-out process. Then the wedge-shape lift-out samples were mounted onto individual W wires supported by Cu wrap and directly sharpened into typical needle-shape APT specimens. At least four APT specimens were made from each bulk MG rod, since multiple APT specimens could be created from each wedge lift-out.

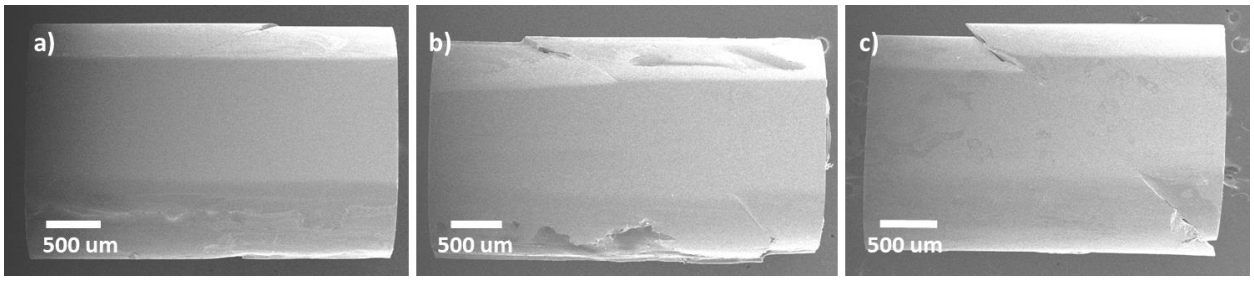

Figure 3.14. a)-c) $Zr_{65}Cu_{25}Al_{10}$ MG rods uniaxially compressed to 1%, 2%, and 4% macroscopic plastic strain, respectively, and polished to a cuboid shape for FIB lift-out.

The APT specimens were first imaged using HAADF-STEM and then evaporated for APT. The reason to image the APT specimens in the TEM was twofold. i) Check if there is a shear band in the APT specimen, and if so, what is the exact location of it? Is it close enough to the tip of the specimen so that it can be evaporated for data collection before the needle gets increasingly blunted during the evaporation process? ii) What is the density change ($\Delta\rho$) of the shear band measured by HAADF-STEM? Will it correspond to the compositional change measured using APT?

A HAADF-STEM image of one of the APT specimens made from the 2% plastic strain rod is shown in Figure 3.15a, and the corresponding atomic reconstruction after evaporation using the APT is shown in Figure 3.15b. The brightness and contrast of the HAADF-STEM image in Figure 3.15a has been adjusted to enhance the visibility of the features, and the calculation was done using the original intensity values. Each colored dot in 3.x2b corresponds to an evaporated ionized atom that each has an x-, y-, and z-position in 3D space and an elemental identity, where purple indicates Zr, orange indicates Cu, and blue indicates Al. It can be clearly seen that the APT needle in both Figure 3.15a and 3.15b is mostly homogenous, except a few dark regions (reduced density compared to the matrix shown by HAADF-STEM) in Figure 3.15a 100-400 nm below the tip of the needle. Those regions are likely nano-scale shear bands. The region with a change in composition in Figure 3.15b 300-400 nm below the tip of the needle (shaded area with an arrow) is probably the same shear band indicated by an arrow in Figure 3.15a. Quantification of the density change of this shear band with respect to the surrounding matrix using the HAADF-STEM image shown in Figure 3.15a and Equation 2.9, without taking any compositional change into account, yields a density reduction of ~14%, which is in the same order of magnitude as some of the Vit105 shear bands with large density reduction values reported earlier in Section 3.1 and shown in Figure 3.3. Note that this density reduction measured with HAADF-STEM can come

from either purely structural dilatation, purely compositional change, or a combination of both. To determine the origin of the density reduction for this particular shear band, compositional analysis via APT was used.

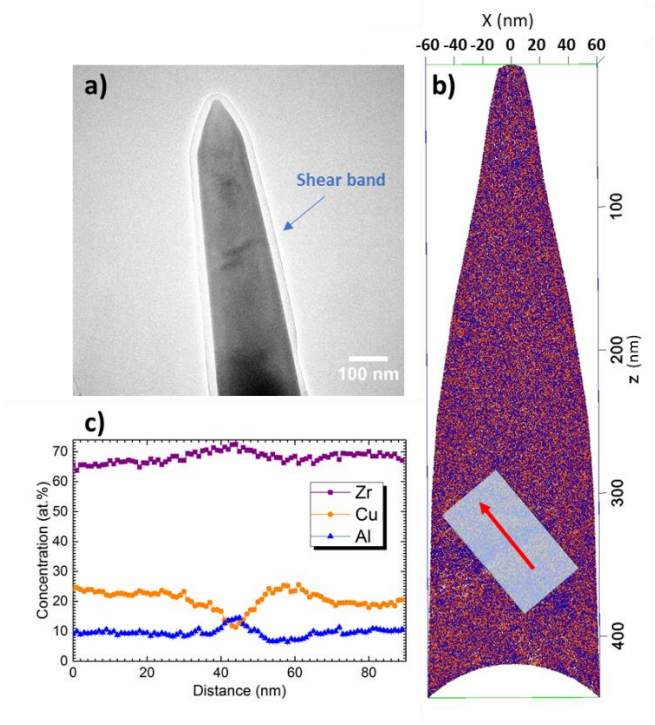

Figure 3.15. a) Brightness and contrast adjusted HAADF-STEM image of an APT specimen made from the 2% plastic strain bulk $Zr_{65}Cu_{25}Al_{10}$ MG rod, showing darker regions 100-400 nm below the tip of the needle that likely emerged from nano-scale shear-band segments. b) APT reconstruction of the specimen shown in a), showing compositional difference in the 300-400 nm region below the tip of the specimen. The shaded region with the arrow indicates the location analyzed to produce the compositional profiles shown in c). No crystallization was found anywhere from this APT specimen.

Figure 3.15c shows the 2D composition profiles (at.%) of each element that were averaged over the shaded region shown in Figure 3.15b, with the arrow indicating the x-axis direction of Figure 3.15c. The composition profiles confirm the chemical composition of the APT specimen aligns very well with the nominal $Zr_{65}Cu_{25}Al_{10}$ composition of the bulk sample and also shows a ~20 nm thick region that has clear changes in composition, with increased Zr and Al contents and a decreased Cu content. It is interesting to note that the compositional change in this $Zr_{65}Cu_{25}Al_{10}$ shear band is different from the compositional changes in a Vit105 shear band reported previously

in Section 3.2.1, where all the resolvable elements reduced in content in the shear band. For this $Zr_{65}Cu_{25}Al_{10}$ shear band, only Cu content reduced by a maximum of ~15% at the center of the shear band, and the Zr and Al contents increased by maximums of ~10% and ~5%, respectively, at the center of the shear band. Using the composition at the center of the shear band, namely, $Zr_{75}Cu_{10}Al_{15}$, and the matrix composition, with the measured HAADF-STEM intensities at the shear band and the matrix (I_{SB} and I_M), the density change was calculated again using Equation 2.8. This calculation no longer assumed $x_k^M = x_k^{SB}$, which was affected by the compositional change, but still reasonably used $t_M = t_{SB}$. Although the compositional change was incorporated, the calculated $\Delta\rho$ was again around -14%, which correlated well with the $\Delta\rho$ measured only with HAADF-STEM, thus validating that the clear chemical segregation in this shear band did not affect the $\Delta\rho$ measured with HAADF-STEM.

Ideally, it would be great to collect at least one set of successful correlative HAADF-STEM and APT results, like the set discussed above for the 2% plastic strain sample, for the other two bulk samples so that the shear-band structural evolution could be mapped as a function of the macroscopic plastic strain. However, it was experimentally impossible to do so. The 1% plastic strain sample, as mentioned before, did not have visible surface cavities that could point to the exact shear-band location, so no determination could be made if a shear band was included in the FIB lift-out wedge. None of the APT specimens showed any signature of shear bands in HAADF-STEM and after APT evaporation. In other words, all the APT specimens made from the 1% plastic strain bulk sample showed homogeneous elemental distribution as the nominal matrix composition in the APT reconstruction, and no intensity differences could be identified in the HAADF-STEM images. It was thus possible that the absence of shear-band signature was either a result of the

small amount of plastic strain mediated by the shear band or a result of missing the shear band during the FIB lift-out process.

In contrast to the reconstructed $Zr_{65}Cu_{25}Al_{10}$ APT specimens discussed above and the Vit105 TEM lamella used for HAADF-STEM work (Section 3.1 and 3.3), two APT specimens made from the 4% plastic strain bulk sample were the only ones that showed crystallization in the shear-band region in this thesis work. Figures 3.16a-d are the HAADF-STEM image of the APT needle before evaporation, the reconstructed APT specimen, a zoom-in view of the reconstructed APT specimen, and two zoom-in views of the crystalline lattice structure from the atomic positions of the reconstructed APT specimen, respectively. The region containing crystalline phases expanded from the tip of the reconstructed APT needle to ~400 nm below it, with a clear boundary between the top region incorporating crystals and the bottom glassy matrix region, as shown in Figurs 3.16a-b. The size of the crystal-containing region exceeded the largest shear-band thickness of ~220 nm observed in a Vit105 MG uniaxially compressed to 6% plastic strain, as reported previously in Section 3.1 (Figure 3.3). While one could argue that the crystallization might be induced by Ga ion implantation or ion-beam damage in the FIB sharpening specimen-preparation process, Ga ion content was very low in all these APT specimens, showing no signature of ion implantation. Also, if such crystallization were caused by the specimen-preparation process, then the APT specimens from the 1% and 2% plastic strain samples should also show crystallization, but none of them contained any crystals. Although the bulk sample compressed to 4% plastic strain was XRD amorphous, two more TEM lamellae were later made after obtaining the APT results to do TEM-based selected-area diffraction in search of crystallization both in the shear-band path and far away from it. Away from the shear band, no crystallization was seen in both lamellae, excluding the possibility of having a partially crystallized as-cast sample, while TEM-based diffraction

proved crystallization in the nano-scale shear-band core close to a cavity. The additional tests and comparison with the data from the 2% plastic strain sample suggested that the shear-band crystallization in the 4% plastic strain sample might be induced by deformation.

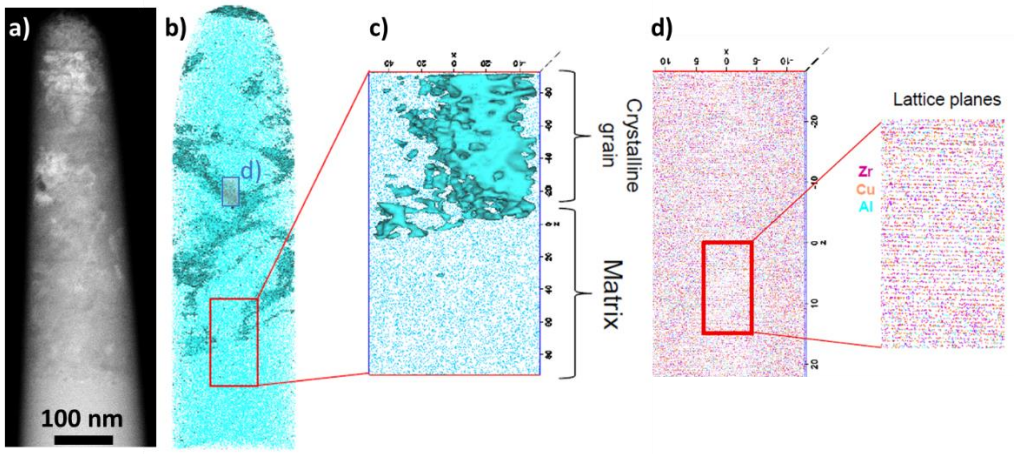

Figure 3.16. a) HAADF-STEM image of an APT specimen extracted along the shear-band path of the $Zr_{65}Cu_{25}Al_{10}$ MG rod uniaxially compressed to 4% plastic strain. b) The APT reconstruction of the specimen shown in a), with a red box indicating the zoom-in view location of c) and a shaded box indicating the zoom-in view location of d). c) Chunks and bits of crystals shown as solid regions, and the atomic positions of the glassy matrix are shown with all atomic species in the same color. d) Zoom-in views of a crystalline region indicated in b), showing periodic lattice planes consisting of Zr, Cu, and Al atoms shown in different colors.

Shear-band crystallization has been reported in the literature for several MG compositions under different deformation modes, such as $Al_{90}Fe_5Gd_5$, $Al_{90}Fe_5Ce_5$, and $Al_{87}Ni_{8.7}Y_{4.3}$ in bending [127, 128], $Al_{88}Y_7Fe_5$ in tension [129], and $Zr_{60}Al_{15}Ni_{25}$ after cold rolling [130]. Chen et al. suggested that there is a compositional dependence of shear-band crystallization [127], since they did not find crystals in an $Al_{85}Ni_{10}Ce_5$ MG after the same bending experiments that produced shear-band crystallization for some other Al-based MGs. Jiang and Atzmon reported that nanocrystallites were observed in shear bands on the compressive side of a bent $Al_{90}Fe_5Gd_5$ MG, while no shear-band crystallization was found on the tensile side [128], and suggesting a dependency on the stress state. Although making a comparison of this work with reports in the literature may imply that there is a strain-dependent tendency for shear-band crystallization, no

conclusion or generalization could be made so far due to the limited sampling in both MG composition and strain states.

To reduce the difficulty in locating shear bands on a polished bulk sample surface, a second batch of APT specimens were made from a bent Vit105 bar, where the shear bands were readily seen as surface offsets, as described previously in Sections 2.1.3 and 2.1.4. Changing to a Vit105 MG would allow sampling of another composition, and probing shear bands from a bent sample would allow sampling of a different plastic strain regime. For the new batch of APT specimens, a more careful method to locate the shear band was used, as described in Section 2.1.4, where part of a FIB lift-out was thinned for TEM observation first to check the presence and location of the nano-scale shear band before sharpening the other part of the lift-out into an APT needle, as shown in Figure 2.8b. While the thinned TEM parts from all the FIB lift-outs showed shear bands with HAADF-STEM imaging, it was surprising that none of APT reconstructions from the same FIB lift-outs (but an adjacent section on the lift-out because the thin TEM lamella part could not be made into a usable APT needle) showed any regions of detectable compositional or structural changes that could indicate the existence of a shear band. It was reasonable to first suspect that none of the APT needles had included any shear bands, although the adjacent TEM part should have improved the process for targeting the exact shear-band location. However, after careful analysis of the HAADF-STEM images that led to quantifiable density changes of the shear bands with respect to the matrix material for this batch of samples, perhaps another explanation was shown to be more reasonable. The analysis of these HAADF-STEM images and the calculated shear-band density changes are presented in the next section (Section 3.3). For the purpose of concluding on this section, a preview of the results from Section 3.3 should be discussed here. It was found that the absolute values of shear-band density reduction from this batch of specimens

made from a bent Vit105 sample was an order of magnitude smaller than the ones measured from shear bands on the compressed Vit105 rods, which brought the density reduction values to less than 1% compared to the matrix. The thickness values of the shear bands in the bent sample were also on the lower end (<80 nm). The combination of low density reduction magnitudes and low thickness values could make the shear bands difficult to detect using the APT method, due to the problems with ion trajectory and local evaporation effects, as mentioned in the beginning of this subsection.

In summary, atomic-scale structural observation of shear bands in MGs using the APT technique is still at a very early stage, and more improvements are needed on both the technique side and the sample-preparation end. With the current challenges and ambiguities from both ends and the limited number of specimens, the APT experiments in this work did not generate fruitful results that could lead to conclusive discussions.

3.3 Shear-strain-dependent nano-scale shear-band structure

Several advanced characterization methods have recently been used to quantify the nano-scale shear-band core structure, including HAADF-STEM (Section 3.1) [95, 96, 98], NB-XRT (Section 3.2.1) [174], fluctuation microscopy [214], and APT (Section 3.2.3) [125, 126]. These efforts revealed how the density and chemistry in nano-scale shear-bands may change relative to the surrounding matrix. Both volumetric expansion and contraction of the shear-band have been reported [95, 96, 98], as well as changes [126] and no changes [125, 174] of shear-band chemistry have been revealed. The precise details that govern such varying outcomes remain unclear and require further efforts that in particular should generate a statistically more robust data set. An additional complexity with the available data is the fact that measurements are made on shear-

band segments that not necessarily have any reported link to a macroscopic and quantifiable observable, obscuring a well-defined reference point for measured structural changes.

This work is based on the hypothesis that the shear strain admitted by a shear band will determine its change in structure relative to the matrix material. It is thus instructive to consider the case of a compression specimen that admitted all macroscopic measurable strain via the operation of one single shear band, as described in Sections 2.1.2 and 3.1 and also in References [98, 181, 215]. The local shear strain of the shear band can easily be determined under the assumption of a given average shear-band thickness. Even though large variations of shear-band thickness values can be found along a shear band, an approximate value of 50 nm yields an excess of 10000 in shear strain for a typical macroscopic compressive engineering strain in the range of 5-10%. With this at hand, the most logic step is to create a variation of the admitted shear-band shear strain in order to interrogate if the hypothesis is valid. This, however, turns out to be experimentally not feasible due to the difficulty in finding the shear-band location after cross sectioning, as described in Section 2.1.3, and the complex internal shear-band structure around regions of shear-band cavitation, as discussed in Section 3.1 and References [97, 98]. To overcome this barrier, sample deformation in a 3-point bending geometry was used instead of the uniaxial compression method, both described in Section 2.1.2.

The 3-point bending setup (Figure 2.3a) is now schematically displayed in Figure 3.17a for the deformation of a Vit105 MG bar, where shear bands are illustrated on the tensile and compressive sides. A regular shear-band pattern forms on the surface, and the height of the surface step decreases from a maximum at the outer-most edge to essentially zero at the end of the shear band, as shown previously in Figure 2.3b. TEM lamellae were extracted at chosen locations along the shear-band trace, allowing the local connection of a given surface step height (h) to a shear-

band thickness (w). From here, the local shear strain (γ) was calculated using $\gamma = h/w$. The shear-band density-change, $\Delta\rho$, was also measured using the HAADF-STEM technique described in Section 2.2.1.

HAADF-STEM data were taken with a JEOL 2010f STEM using a camera length of 15cm from different TEM lamellae extracted from the Vit105 bending bar shown in Figure 2.3. All samples have been prepared with the FIB lift-out method described in Section 2.1.3. Figure 3.17b shows a surface step filled with the Pt protection layer and a dashed line that indicates the location of the shear band extending from the surface step. Note that the Pt protection layer was necessary to be left on the TEM lamella during FIB thinning because it allowed the measurement of the surface step height. Without the Pt layer, it was impossible to know if the surface step had changed its height due to FIB milling. A zoom-in HAADF-STEM image on the shear-band segment indicated in Figure 3.17b is shown in Figure 3.17c, where the shear band is darker and therefore less dense than the surrounding matrix material. The bright part on the upper left edge in Figure 3.17c is Pt.

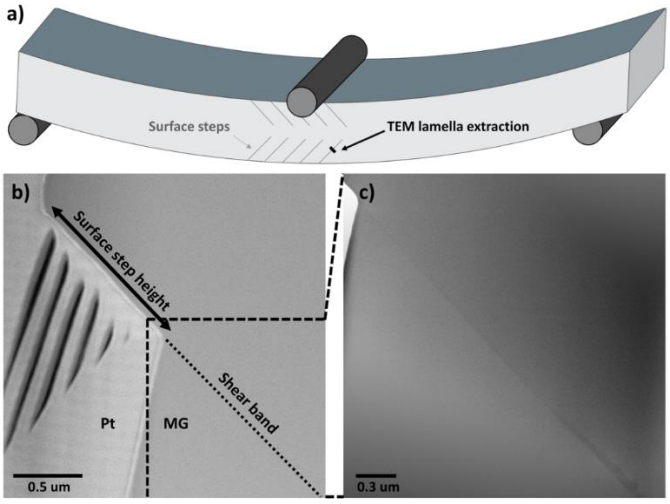

Figure 3.17. a) Schematic of the 3-point bending geometry used, also exemplifying a location of TEM lamella extraction. b) HAADF-STEM image displaying a surface step, from which a shear band extends into the sample. The Pt protection layer is also seen. The shear-band indicated with a dotted line in b) is highlighted in c) with a zoom-in HAADF-STEM image.

In Figure 3.17b, it is evident that the shear band is angled relative to the sample surface, meaning that the normal vector of the shear-band plane is not perpendicular to the normal vector of the surface of the specimen, unlike the ideal case illustrated in Figure 2.4c. This means that the shear band shown in Figure 3.17c was not from an edge-on imaging condition and may include a significant projection error, which directly affects the shear-band thickness measurement and the intensity values used to calculate $\Delta\rho$. Therefore, all the TEM lamellae were first imaged under different tilting conditions, and the maximum contrast between the shear-band core and the surrounding matrix material was identified as taken from the edge-on imaging condition, as discussed in Section 2.2.2. For example, Figure 2.19 shows a variation of the position-dependent $\Delta\rho$ as a function of the shear-band thickness for different tilting conditions. It illustrates the fact that the increasing misalignment between the incoming electron beam and the shear-band plane causes an increase of w and a decrease of $|\Delta\rho|$. The error bars also increase significantly with such misalignment. This reflects the expected trend, since a tilted shear band relative to the viewing axis will widen and the HAADF-STEM contrast will blur out due to the incorporation of the higher-density matrix material. A blurred contrast yields a less well-defined shear band and therefore larger error bars for w. In the particular case depicted in Figure 2.19, a 0° tilt angle was found as the optimum edge-on imaging condition. However, it should be noted that this does not mean that the shear band was edge-on in the TEM lamella at extraction, since mounting the lamella onto a grid introduces an additional geometry change, which may or may not correct for the tilt upon TEM lamella extraction.

A total of 14 TEM lamellae were extracted from different locations along shear-band segments extending from the tensile surface of the Vit105 MG bending-bar sample towards the neutral axis of the bending beam. Ten of those TEM lamellae had an adjacent thick part left

intentionally for producing APT specimens and have all been used for APT experiments, as discussed in Section 3.2.3. HAADF-STEM images were taken for all the TEM lamellae and analyzed using the method and tilt tests described in Sections 2.2.1 and 2.2.2 to collect shear-band $\Delta\rho$ and w values at the tilt conditions that were closest to the idea edge-on view. The extracted data in terms of $\Delta\rho$ and w is summarized in Figure 3.18, which displays the $\Delta\rho$-w correlation. Each color represents a given shear-band segment from a particular TEM lamella. Each shear-band segment is analyzed in a position-dependent manner described in Section 2.2.1, therefore yielding variations within each colored set of data.

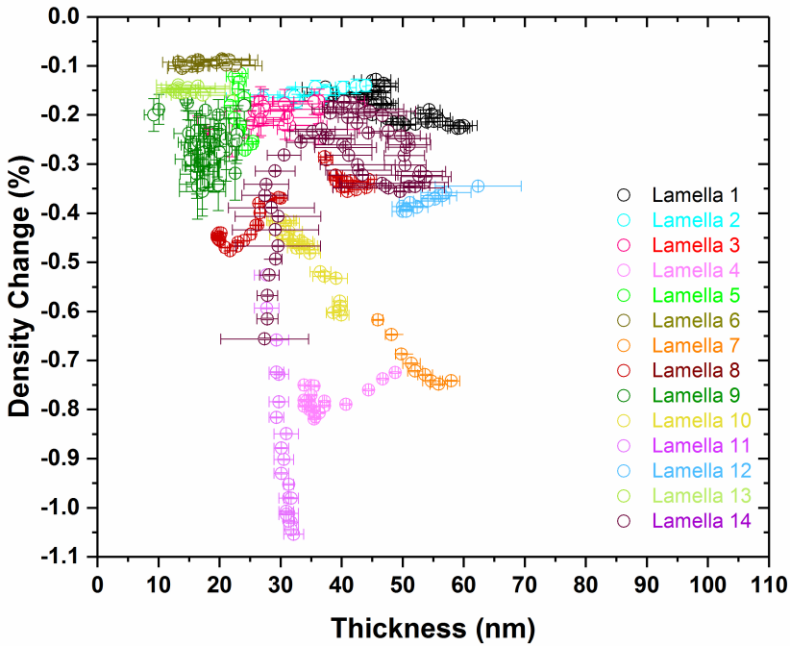

Figure 3.18. Density change as a function of shear-band thickness calculated from shear-band segments present on 14 different TEM lamellae extracted from a Vit105 MG bar plastically deformed using 3-point bending geometry.

The variations in $\Delta\rho$ are significantly smaller than observed earlier in both cold rolled [95, 96] and uniaxially deformed (Section 3.1) [98] MG specimens. In fact, the determined density changes here are approximately one order of magnitude smaller than in the strongly deformed materials discussed in Section 3.1 and References [95, 96], and cover a somewhat smaller range

in shear-band thickness, as well. No particular trend can be deduced from the scattered data in Figure 3.18. Combining the data in Figure 3.18 from the bending bar experiments with the data obtained from compression samples of the same Vit105 MG reinforces the almost separate regimes of $\Delta\rho$, as shown in Figure 3.19.

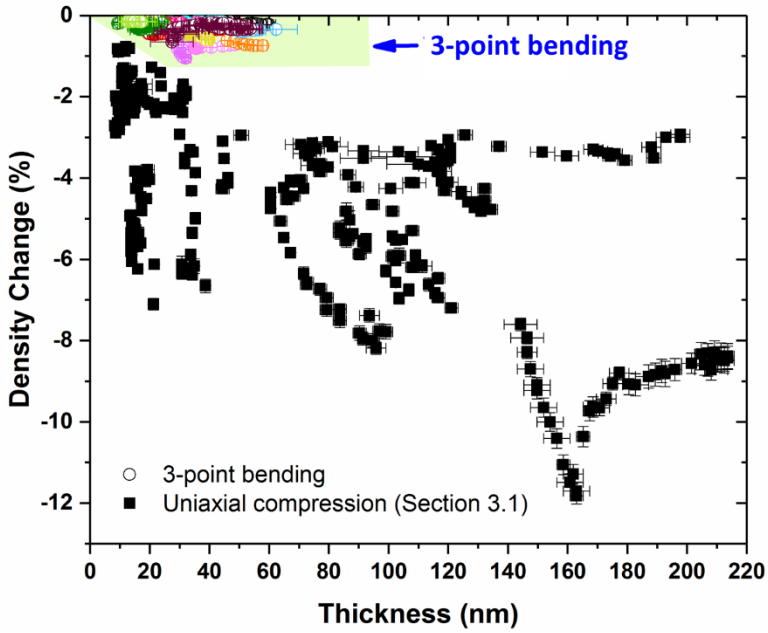

Figure 3.19. The data from Figure 3.18 compared to the same type of data obtained from a uniaxially compressed Vit105 MG rod, which is also presented in Figure 3.3c.

In a histogram representation shown in Figure 3.20a, it is seen that the shear-band thickness peaks at around 20-40 nm in the case of the bending bar samples, whereas large counts are present for the smallest size bin up to 20 nm, as well as around 100-120 nm, in the case of the compression rod samples. The non-negligible tail of w from the compression rod samples covers thickness values that are a factor of 2.8 higher than for the bending bar samples. On the other hand, following the discussion around Figure 3.19, the separation between the $\Delta\rho$ data sets is expectedly sharp, as seen in Figure 3.20b, where overlap is only present in the -1% to -2% bins. The extensive tail in

$\Delta\rho$ to -12% from the compression rod samples is in agreement with earlier data from both cold-rolled $Al_{88}Y_7Fe_5$ MG [95, 96] and in-situ acoustic emission (AE) testing on Vit105 MG [122].

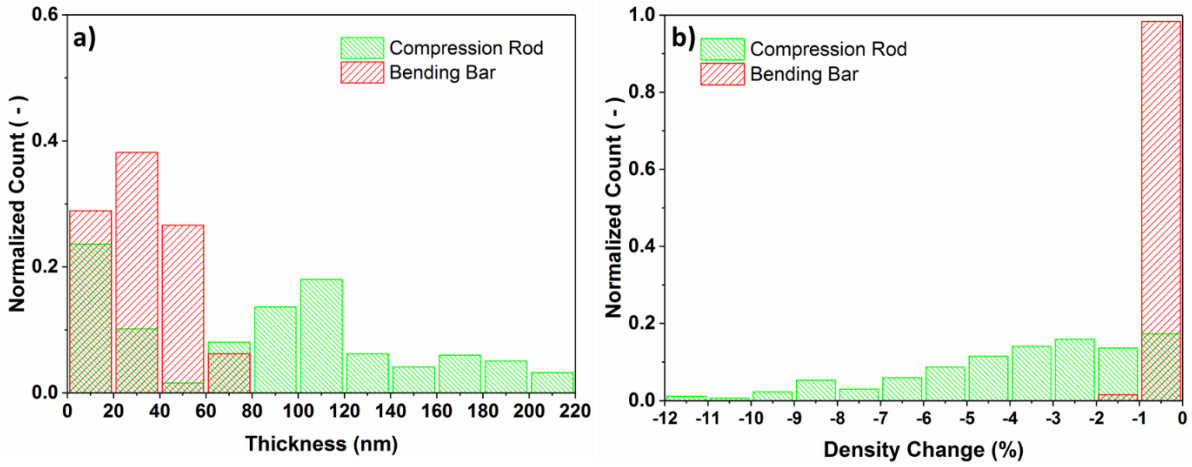

Figure 3.20. a) and b) are histogram representations of shear-band thickness and density change, respectively, summarizing the data presented in Figure 3.19 from both the bending bar and the uniaxially compressed rod.

The separation of magnitude ranges in both w and $\Delta\rho$ leads to the question: what drives this difference between the two data sets from the same Vit105 alloy? It is argued here that this difference is a manifestation of shear-strain-dependent damage accumulation in a shear band. In the case of the bending bar, it is possible to estimate the local shear strain (γ) admitted by the shear band by dividing the surface-offset height (h) by the locally measured shear-band thickness (w). Since the surface steps rarely exceed 1 µm, and the smaller values of w are approximately 10 nm, an upper bound of local shear strain of 100 is obtained for the bending bar. Using the total shear offset in the case of the compression rods, γ-values of several 10000s are found. Figure 3.21 displays the $\Delta\rho$-γ scatter plot, including data from compression samples that revealed a single isolated shear band (represented as circular marks in Figure 3.3c). The use of data from single isolated shear bands in the compression rod sample ensured that the shear strain calculation from the shear-band thickness values in this sample was not affected by internal stress relief near cavities.

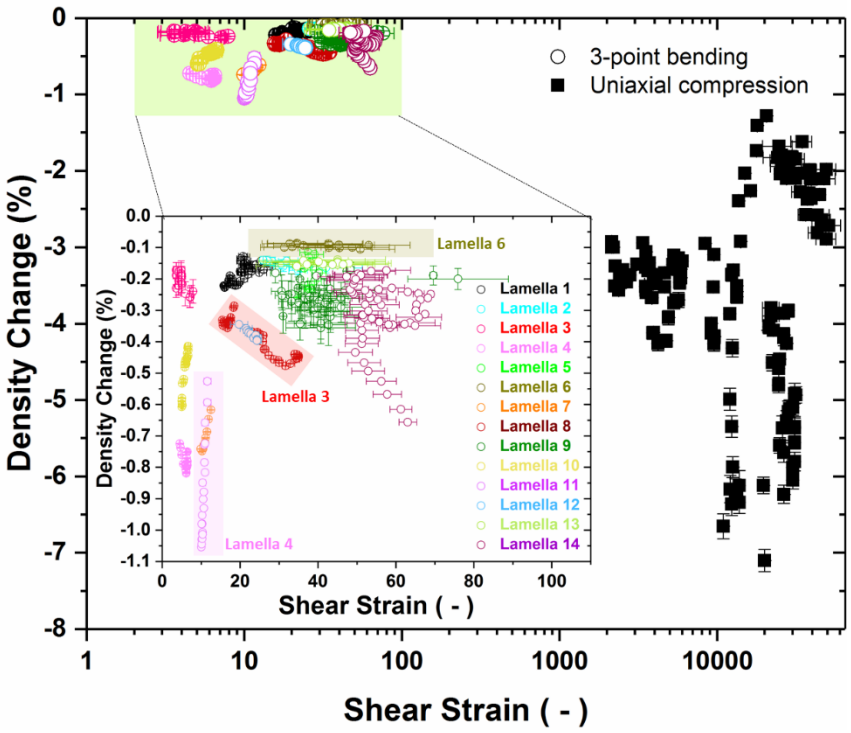

Figure 3.21. Density change as a function of shear strain for both TEM data extracted from the 3-point bending sample and compression rod. The inset highlights the data for the bending sample.

Separated by a minimum of one order of magnitude and spanning a range of at least four orders of magnitude in γ, distinctly different regimes in $\Delta\rho$ are covered by the two data sets. Despite the scatter within each sample type, the overall conclusion is thus that shear strain seems to drive the total amount of density change in a shear band, which proves the hypothesis for conducting this thesis work, as discussed in one of the research objectives in Section 1.3.1. This conclusion cannot be made by individual data sets (the inset in Figure 3.21), which can be exemplified by comparing the $|\Delta\rho|$-γ trends of lamellae 3, 4, and 6. The data from lamella 4 is practically constant in $|\Delta\rho|$ for all γ. The opposite trend is seen for lamella 6. In the case of lamella 3, $|\Delta\rho|$-γ exhibits a positive correlation as the overall data set. The reason for such non-trivial variations can only be speculated upon at this stage. If the general conclusion of a shear-dependent volumetric structural expansion is correct, this must hold true just after the shear band has come to an arrest. However,

subsequent structural relaxation in combination with local residual shear-band stress-fields is expected to alter the structural signature from shear deformation. In addition, one cannot exclude subtle influences from the TEM sample preparation that might not uniformly affect our obtained data set.

Despite these unknowns and the fundamental discrepancies between time- and length-scales, recent atomistic simulation approaches are in good qualitative agreement with our findings. For example, both References [216, 217] demonstrated shear-band broadening as a function of strain, where Hassani and co-workers also highlight the strong fluctuations of physical properties along the shear band. Alix-williams and Falk also pointed towards a shear-band widening limit based on a competition between athermal configurational disordering and thermal relaxation. This limit is not yet seen in experimental evidence. It is, however, instructive to consider the limit of the probed shear-band dilatation as a function of accumulated shear strain. At some point, the shear dilatation will separate atoms to the degree that the cohesion energy is overcome and bond rupture occurs. This must mark the onset of what previously has been reported as nano-void formation via free volume accumulation [128, 131] or a larger length scales is referred to the formation of shear-band cavities [11, 175, 218]. Since any so far revealed shear-band property is strongly dependent on position along the shear band, bond rupture and therefore cavity formation may initiate at different locations and shear strains on the shear-band plane.

In summary, it was investigated experimentally here if any evidence of structural shear-band damage may depend on shear strain. To this end, 14 TEM specimen were extracted from a 3-point bending bar and analyzed in terms of shear-band width and density change. Together with the data from compression samples (Section 3.1), a widely scattered data set with a general positive correlation between volume expansion and shear strain is revealed. It can be concluded that the

structure within the shear-band core depends on shear strain, implying that shear-driven disordering dominates over thermally-activated relaxation during flow at the testing temperature of T/T_g=0.45 here and over the probed shear-strain regime.

3.4 Micro-scale shear-band cavities and apparent strain hardening

Large micron-scale regions of shear-band cavities, or internal micro-cracks lying on the shear-band plane, were previously reported on cross-sectional surfaces of deformed but macroscopically intact compression samples [97, 202, 215]. It should be noted that the chosen terminology of "shear-band cavity" simply refers to a hollow region located on the shear-band plane and does not refer to the physically well-defined cavitation mechanism [219]. Having so far relied on classical metallography (mechanical polishing to reveal the internal cavities), the purpose of this project is to expand the current knowledge on shear-band cavities by reconstructing a full 3D view of the internal cavity structure of deformed specimens that were unloaded during serrated flow and prior to fracture.

3.4.1 3D reconstruction of shear-band cavities

In total, four uniaxially compressed MG rods (one Vit105 and three $Zr_{65}Cu_{25}Al_{10}$), each containing a major system-spanning shear band, were scanned using the phase-contrast XRT method described in Section 2.3.2. The first one, the Vit105 MG rod compressed to 8% total strain (~6% plastic strain) that was used for HAADF-STEM, NB-XRF and SEND work was also used for XRT. It serve as a tester sample that was used to provide evidence of the shear-band cavities [98] and was not fully scanned, as shown in the schematic in Figure 3.22a. The other three $Zr_{65}Cu_{25}Al_{10}$ rods were fully scanned, as shown in Figure 3.22b, and their reconstructions of

cavities were analyzed in more detail and revealed significant quantity of cavities [175]. Both datasets are presented in this section, but note that the x-, y-, and z-axes in the Vit105 dataset are different from those in the $Zr_{65}Cu_{25}Al_{10}$ dataset.

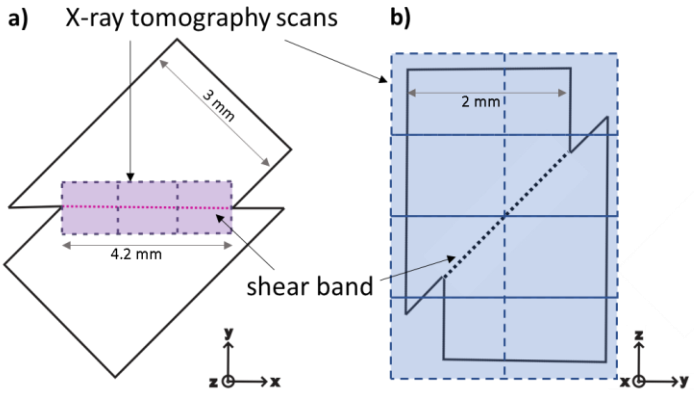

Figure 3.22. a) Schematic of XRT scan geometry for the Vit105 sample. b) Schematic of XRT scan geometry for the three $Zr_{65}Cu_{25}Al_{10}$ samples.

For the XRT scan of the Vit105 sample, since the sample was larger than the collimated beam size, three individual tomographic scans were conducted through a series of 0.2^{o} step rotations over 360°, where the centers of rotation were 1.35 mm apart. Figure 3.22a shows schematically the region around the shear band that was scanned. The shear-band plane was positioned parallel to the z-direction and normal to the y-direction. The three tomographic scans were stitched together by the APS beamline scientist Dr. Peter Kenesei. The stitched scans were then reconstructed into 1152 slices of 2D images normal to the y-direction using the GRIDREC algorithm [191, 192]. Examples of the reconstructed 2D images are shown in Figures 3.23a-d in Section 3.4. After receiving the 2D images from the APS, the 3D volume of 4.2 mm × 0.8 mm × 1.73 mm (x-, y- and z-directions, respectively) was created by stacking the 2D images along the y-direction. Each slice of image contains the integration of intensity over a range of 0.7 μm in the y-direction, and these images were smoothed using a Gaussian filter in MATLAB to reveal the

features of interest before reconstructing into 3D. 3D reconstruction was done using either MATLAB or Vaa3D [220].

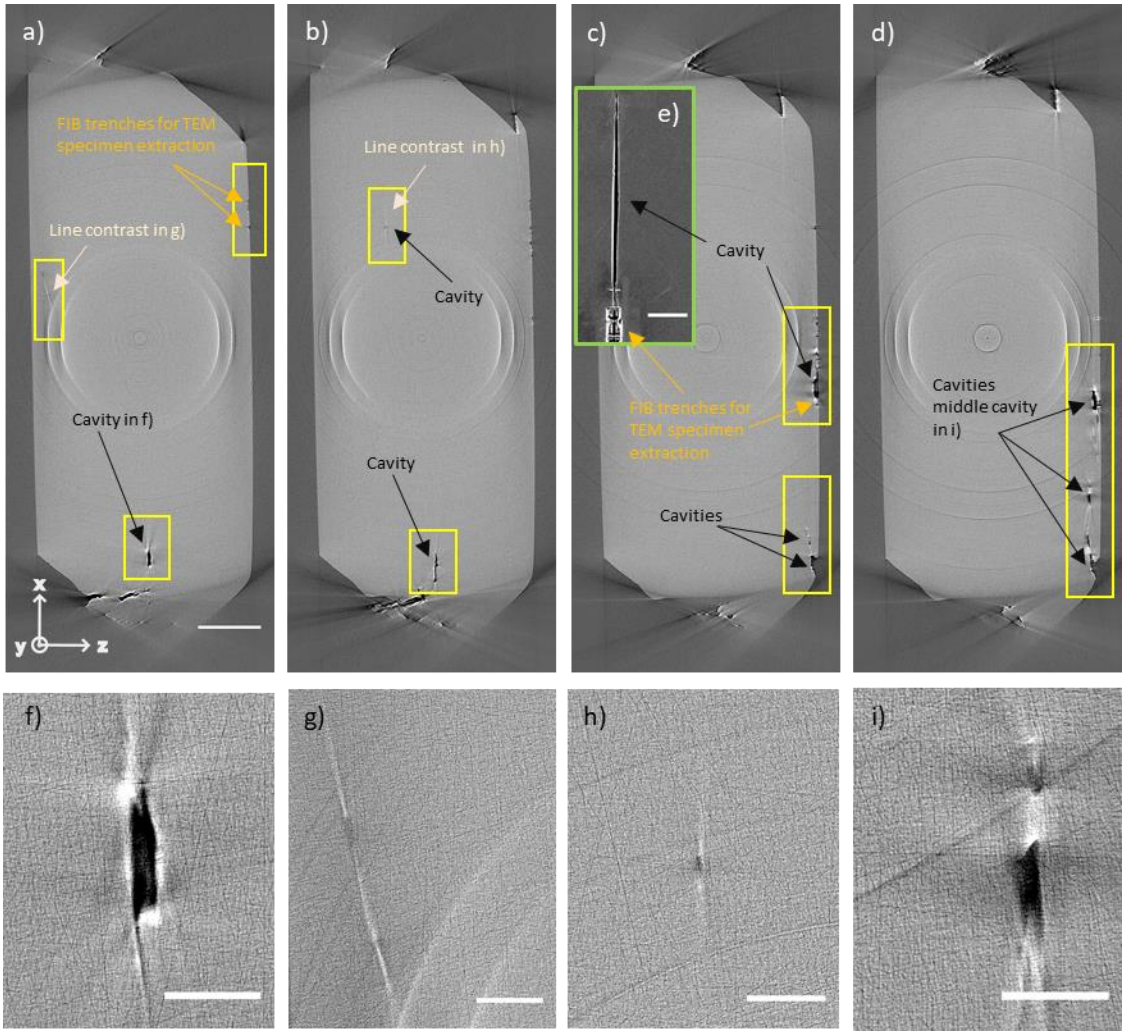

Figure 3.23. a) - d) Reconstructed XRT 2D slices along the y-direction, showing distinct features within the bulk sample. The axis directions correspond to those in Figure 3.22a. e) SEM image viewing from the z-direction at a cavity along the shear band. Such cavities appear on the sample surface after polishing and reveal the location of the shear band, which guides the FIB lift-out location for extracting TEM specimens. f) - i) Zoomed in views on selected features on the shear band. Scale bars: a) - d) 0.5 mm, d) 20 µm, f) - i) 100 µm.

Since the shear band was not perfectly parallel to the z-direction or normal to the y-direction due to slight misalignment during sample positioning and its non-planar morphology (introduced in Section 1.2.3 with Reference [97]), the shear-band plane revealed itself in about 140 images, extending ~100 µm in the y-direction. These images contained distinct features, such

as dark cavities, light line contrasts, and FIB trenches from the aforementioned TEM work, all of which allow tracing of the shear-band plane. Four typical phase-contrast images are shown in Figure 3.23a-d, and different features are enclosed in rectangular boxes pointed out by arrows. The concentric ring artifacts on each image are due to the nonlinear detector response from scintillator distortions and are not physical features in the sample. The dark gray outer bound is the background in air. In Figure 3.23a, the upper right box indicates FIB trenches where TEM specimens were extracted for the HAADF-STEM work discussed in Section 3.1. Similarly, moving further down in the y-direction (that is from slice to slice and therefore along the normal direction to the approximate shear-band plane), Figures 3.23b-d also have FIB trenches on the right-side edge. The FIB trenches serve as good indicators of the shear-band plane, since they are directly on top of the macroscopic shear-band line on the surface of the sample. In Figure 3.23a, the lower box indicates an example of a cavity ~120 μm × 30 μm. This cavity appears in eight consecutive slices, extending ~6 μm in the y-direction. A zoomed-in view of this cavity is shown in Figure 3.23f. Another cavity adjacent to the one in Figure 3.23a is highlighted at the lower end of Figure 3.23b, which is 9.8 μm below Figure 3.23a in the y-direction. This cavity is ~230 μm × 20 μm and extends ~27 μm in the y-direction.

Two large surface cavities are enclosed in the boxes in Figure 3.23c. Note that the sample was polished flat for nanoindentation, SEM, FIB liftout and XRT, which means that the cavities that appear on the surface were previously inside the deformed sample volume. An SEM image of a cavity in Figure 3.23c is shown in Figure 3.23e. In the SEM, the depth of this surface cavity cannot be measured in the z-direction without destructively polishing the surface away layer-by-layer. In Figure 3.23c, this surface cavity in the upper box has a depth of 35 μm in the z-direction. The TEM lamella extracted at the lower end of this cavity shows a large shear-band thickness of

~140 nm to 210 nm, as presented in Section 3.1. The shear-band thickness data from this TEM lamella are shown in Figure 3.3c in the lower right corner, having the largest thickness and density change.

Furthermore, Figure 3.23d is a slice 5.6 µm below the one in Figure 3.23c in the y-direction, and the same cavities remain in both slices with a slight extension in the z-direction. These cavities are thus extended more than 5 µm in the direction normal to the shear band. The lower box in Figure 3.23c shows another cavity of ~130 µm extension in the x-direction, which is linked to smaller cavities to its upper left region by a faint line of lighter contrast. Such line contrasts are also shown in Figures 3.23a, b and d. These lighter lines are shown more clearly in the zoom-in views in Figures 3.23f-i and indicate an interference of the phase contrast method. Such a bright line-contrast is paired with a darker feature in an adjacent image slice, excluding the possible interpretation of a local region with higher density. It is reasonable to assume that these lines mark regions of delamination at the resolution limit of the XRT technique, and we note that their length cannot be taken as an indication of the physical size of the underlying cavities.

Image filters were applied to each slice of 2D reconstruction to reduce the file size and to remove the circular reconstruction artifacts and TEM lamella extraction sites, in order to exclusively reveal regions of shear-band cavities. After stacking the 2D images in the y-direction using the Vaa3D software [220], the cavities were reconstructed in 3D. Three different views of rotation are shown in Figure 3.24. To improve readability and visualization of Figure 3.24, the extent of the sample in the y-direction has been multiplied by a factor of four. Numerous local cavities (110 in total) were found in this compressed Vit105 sample, and these cavities presumably define the shear plane. Since parts of the sample have been polished away, the data in Figures 3.23 and 3.24 only display ~70% of the total shear-band plane. An edge-on view along the x-axis and

normal to the y-z-plane in Figure 3.24c reveals that the shear-band plane, as indicated by the arrangement of the cavities, is not planar, and that closely located cavities can have large angular misorientations that cause local shear-plane curvatures. Figure 3.24c highlights such a situation, where two adjacent cavities have a misorientation angle of 40°. The data also shows that all cavities seem to align well with the x-z-plane to the left of the box in Figure 3.24c indicating local curvature, whereas the shear-band plane is generally curved at higher z-values. Overall, the XRT data reveals a pronounced shear-plane roughness and a significant amount of micron-size cavities, the latter of which do introduce complex stress states and stress gradients at their circumference as they effectively act as internal notches that are the determining structural features triggering a run-away crack.

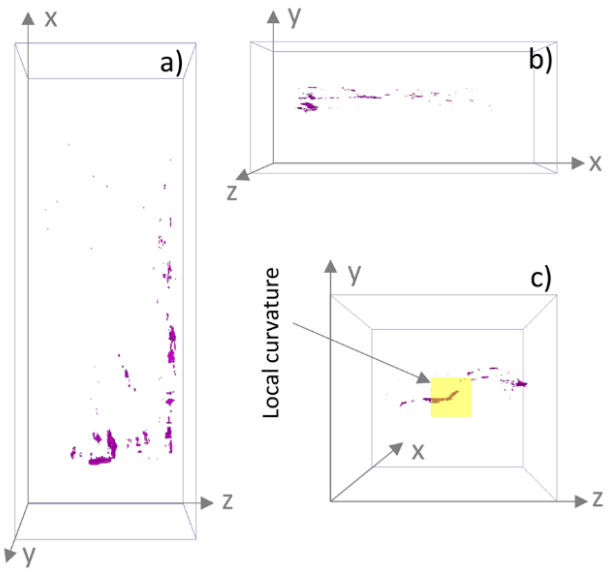

Figure 3.24. a) - c) Three different views from the XRT 3D reconstruction of the Vit105 sample showing cavities. Volume size: 5.26 mm × 0.49 mm × 2.12 mm in x-, y- and z-directions, respectively. The total reconstructed cavity volume contains ~1.46×10^{10} pixels and is viewed here using the Vaa3D software. Only features above the noise threshold are displayed.

These 110 cavities shown in Figure 3.24 serve as an indication of the shear-band plane, as they are expected to nucleate from nano-scale voids where the material has locally exceeded the

cavitation stress during shear-band propagation [221]. It can be expected that the number of cavities will depend both on the accumulated shear strain, the shear-plane topography that is defined at the moment of shear-band formation, and the loading mode. These influencing factors add additional complexity to the proper structural description of a shear band and may be best disentangled using coarse-grained atomistic [135] or continuum simulations [222]. From the observation of optical microscopy or SEM imaging, system-spanning shear-bands appear often as straight lines on the surface, (e.g. Figures 1.10b and 2.2b), irrespective of loading mode, which may be taken as an indication for a planar defect. The data obtained by XRT indicates the opposite. Of particular interest is the strong fluctuation of y-values (position normal to the global shear-plane) amongst nearby (in x- and z-coordinates) located cavities. Figure 3.25 displays this spread by projecting all cavities onto the x-y-plane in the z-direction, with real sample dimensions. In such a representation, it is seen that cavities scatter within the y-range of ~100 µm in the direction normal to the shear-band plane. Local jumps in the y-direction between adjacent cavities can be as large as 40 µm, with an in-plane (x-z-plane) distance of ~80 µm.

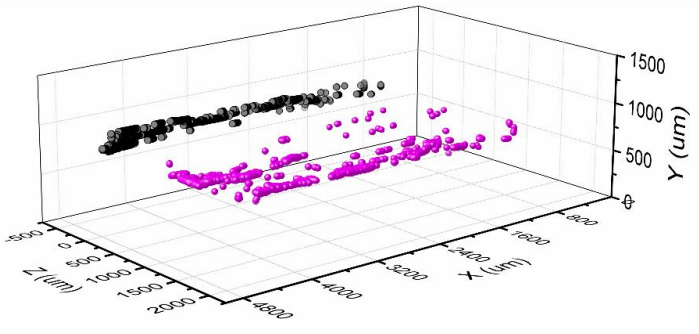

Figure 3.25. Cavities in 3D shown in purple are projected on the x-y-plane in the z-direction as black dots, showing the spread of shear-band cavities in ~ 80 µm in the y-direction. The cavities plotted here use the same pixels as in Figures 3.22a, 3.23 and 3.24.

With the successful reconstruction of shear-band cavities in the Vit105 MG sample described above, a more detailed XRT work that compares the shear-band cavity structure and

distribution among three $Zr_{65}Cu_{25}Al_{10}$ samples were conducted. The reasons for repeating the XRT experiment on the additional samples were: i) to observe cavities in another MG alloy composition and ii) to explore the effect of plastic strain dependency on cavity distribution. The $Zr_{65}Cu_{25}Al_{10}$ rods all have a diameter of 2 mm and were produced by suction casting into a Cu-mold, as described in Section 2.1.1. In order to constrain strain localization to one macroscopic and system-spanning shear band, the samples were notched via electric discharge machining prior to compression, which was described in Section 2.1.2 and in Reference [181]. The three notched $Zr_{65}Cu_{25}Al_{10}$ samples with initial lengths of 3.7 mm, 4.0 mm, and 3.8 mm were uniaxially compressed with a strain rate of ~10^{-3} s^{-1} and unloaded prior to failure at plastic engineering strains of 0.141, 0.138, and 0.117, respectively. They are named samples 1, 2 and 3, respectively. SEM images of the three compressed samples are shown in Figure 3.26. The image for sample 3 was taken before reloading it. The engineering stress-strain curves (corrected for machine compliance) of the three samples are shown in Figure 3.27. In numbering order, the samples experienced a resolved shear displacement (shear offset) of 744 µm, 781 µm, and 629 µm, prior to unloading (and prior to reloading in the case of sample 3), where the change in this order in comparison to the plastic strain at unloading originates from different initial lengths of the compressed specimens.

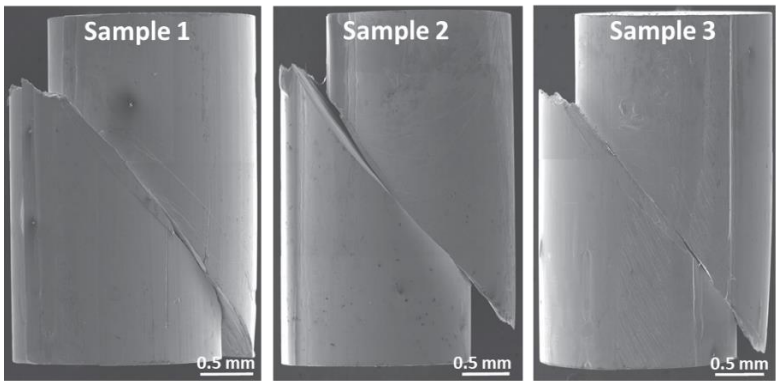

Figure 3.26. SEM images of the three uniaxially compressed $Zr_{65}Cu_{25}Al_{10}$ samples used for XRT, showing that essentially all plastic engineering strain was mediated by only one major shear band in each sample. All of them were unloaded prior to failure and still remained intact at the time of SEM imaging. Sample 3 was reloaded after imaging.

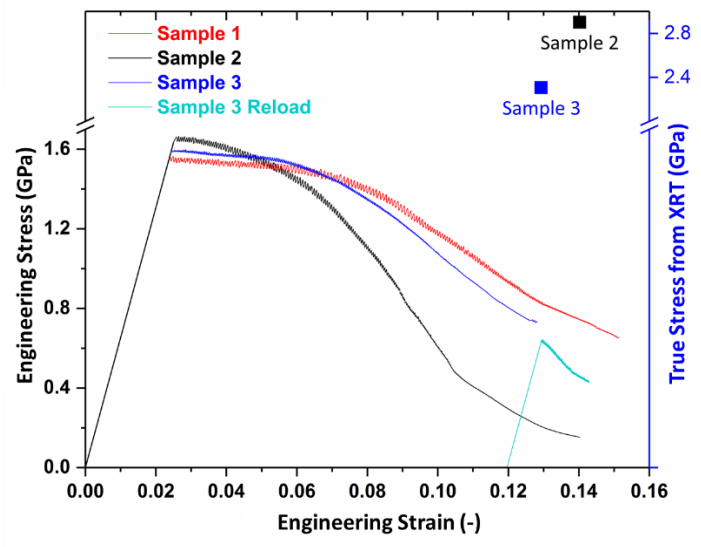

Figure 3.27. Engineering stress-strain curves of the $Zr_{65}Cu_{25}Al_{10}$ samples 1, 2 and 3. True stress values based on the XRT data are also displayed (right y-axis).

Unlike the Vit105 sample, the three $Zr_{65}Cu_{25}Al_{10}$ samples were placed upright with the cylindrical axis normal to the incident X-ray beam, as shown in Figure 3.22b. Two horizontal tomographic scans were performed through a series of 0.2° rotational steps over a full 360° turn, where the centers of rotation were placed 1.3 mm apart. The sample stage was then moved in the direction of the cylindrical axis with a step size of 0.7 mm so that the two horizontal scans were repeated three more times in the vertical direction to cover the entire shear-band region. A total of eight scans were later stitched together [193] by Dr. Peter Kenesei and reconstructed into 1152 slices of 2D images for each sample using the GRIDREC algorithm [191, 192]. Similar to the Vit105 sample, the 2D images of the three $Zr_{65}Cu_{25}Al_{10}$ samples were smoothed using a Gaussian filter in MATLAB to reduce noise and remove artifacts, and only the cavities were selected from each image for the 3D reconstruction. Note again that the x-, y-, and z-axis notations are not the same for the Vit105 and the three $Zr_{65}Cu_{25}Al_{10}$ samples, as shown in Figure 3.22.

3D reconstructions of the shear-band cavities in all three $Zr_{65}Cu_{25}Al_{10}$ samples are shown in Figure 3.28. The blue areas in Figures 3.28 represent the cavity morphology obtained with XRT

and are thus representative of the sample history that includes the stress-strain data shown in Figure 3.27 and the elapsed time until the XRT measurements. The transparent cylinders in Figure 3.28 indicate schematically the geometry of the samples, omitting the shear offset created during deformation, and the loading direction is along the z-axis. Note that the cavity morphology depicted in Figure 3.28 comes from only ~90% of the overlapping shear plane, due to the removal of the outmost annulus, which was done in MATLAB for data processing purposes and better in-bulk characterization. It can be seen that the upper shearing sample part has disconnected from the lower part over large fractions of the actual shear plane in all three specimens, especially in sample 2, which only features a few small regions that are still connected. Expressed in surface area fraction, samples 1 through 3 exhibit shear-band cavities of about 0.50, 0.94, and 0.56, respectively. This is generally in agreement with Figure 3.27, where the stress at the first unloading is significantly lower for sample 2 than for the other two samples.

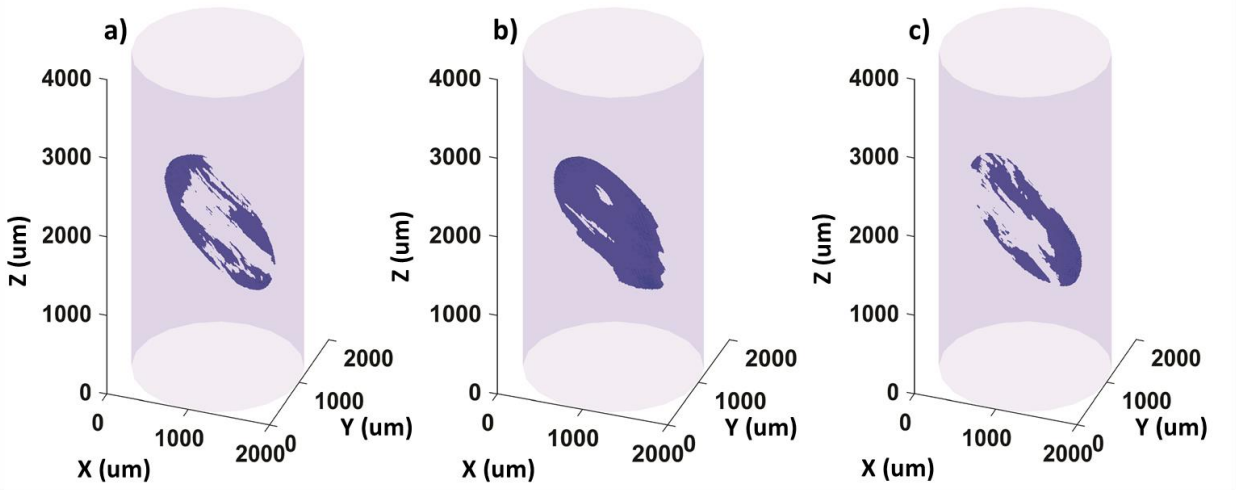

Figure 3.28 a)-c) 3D reconstruction of shear-band cavities in samples 1, 2 and 3, respectively. Colored regions are indications of shear-band cavities.

Although these three samples have the same chemical composition, the surface area fraction of the cavities differ largely because the formation of the shear-band cavities strongly

depends on spatially varying local atomic-scale stresses that trigger bond-rupture and eventually lead to the observed features here [97, 219, 221]. It is expected that the locations at which local bond rupture occurs is specific to each tested sample. It can further be observed that all samples indicate large amounts of shear-band cavities around the circumference with the largest intact sample area inside the specimen (sample 1 and 3). Even though the nano-scale shear band cannot be resolved in the XRT experiment, we argue that the planar region of internal cavities defines the original shear-band plane on which void formation likely is initiated via processes revealed in atomistic and continuum simulations [219, 221]. This conclusion is based on the assumption that nano-scale voids that previously have been revealed with TEM to form within the shear band grow as a function of continued shear [128, 131, 132]. No other cavities or voids are found in regions different than the ones highlighted in Figure 3.28.

The fine structure of the shear-band cavity plane is displayed in Figure 3.29 with a top-down view normal to the shear plane, and the x-, y-, and z- axes are not the same as those in Figure 3.28. The detached areas are displayed as colored regions, and the white regions represent still-attached areas. The color scale along the z-axis, which is normal to the shear plane, indicates height values measured from the lowest point on each plane. In all three samples, the shear-band plane, as outlined by the cavities, has a significant topography, with height variations spanning up to ~80 μm, which is in good agreement with the cavity distribution range normal to the shear-band plane for the Vit105 sample, as shown in Figure 3.25. Determination of the root-mean square shear-plane roughness yields, in sample order, 58 μm, 64 μm and 45 μm. These values translate in order into a center-line-average (c.l.a.) roughness of 11 μm, 10 μm and 8 μm. This substantiates our earlier statement of the large roughness of shear-band planes, as derived from cross-sectional views and the tracing of angular deviations between individual cavities [97]. In 3D, it also becomes

clear that shear occurs on a wavy surface, with valleys and ridges being oriented in the sliding direction of the upper sample part (left to right in Figure 3.29).

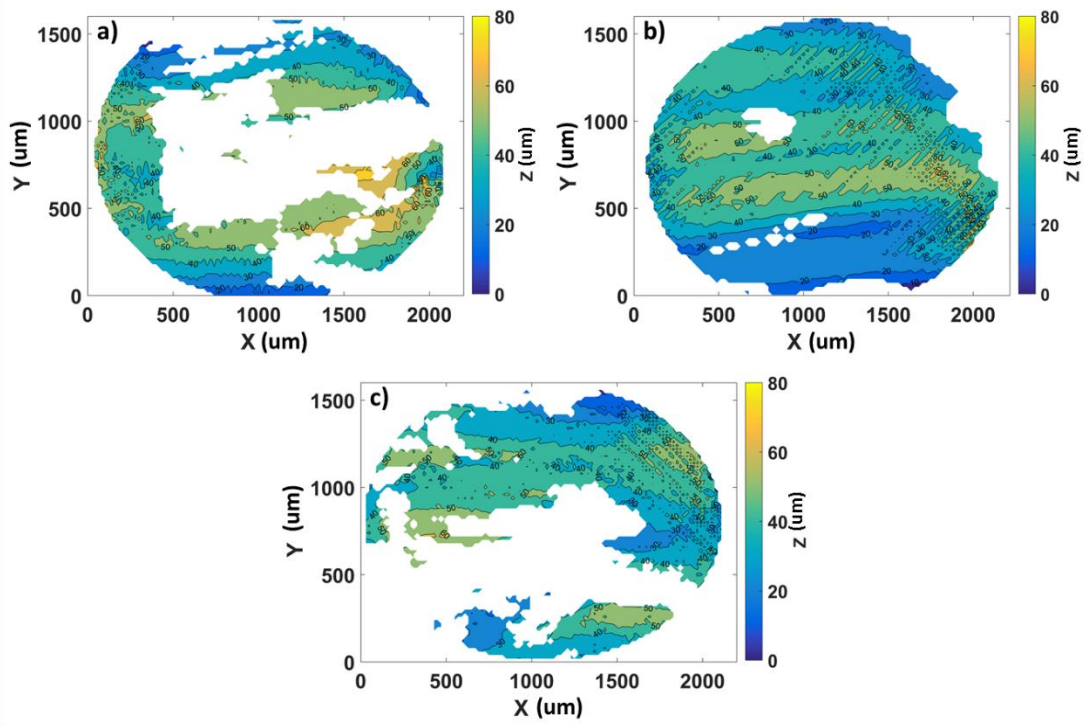

Figure 3.29. a) – c) Top-down view (normal to the shear-band plane) contour plots of shear-band cavities in sample 1, 2, and 3, respectively. The z-axis begins at the lowest point of each cavity morphology.

It should be noted that the cavity morphology shown in Figure 3.29 is a result of two parts sliding relative to each other, which means that adjacent attached regions aligned in the direction of shear have all undergone large local shear strains (~12000-16000; assuming a shear-band thickness of ~50 nm). As a result, it is expected that there is a significant evolution in the details seen in Figure 3.29 as shearing proceeds. Indeed, a pre-existing internal crack is known to develop local tensile stresses even under an overall far-field compression and will thus grow via locally maximizing mode I stress intensities [223]. Due to the limited spatial resolution, it is furthermore possible that parts of the still attached regions already have detached. Despite these uncertainties, it can be concluded at this stage that there must be a gradually increasing fraction of the shear-

band plane that during shear evolves into shear-band cavities, causing the system-spanning shear band to reduce in area at the expense of locally disconnected regions (cavities). An unlikely alternative to this conclusion is that all shear-band cavities form abruptly at some imparted shear strain prior to unloading. Challenging in-situ experiments would be required to provide a definite answer. The conclusion here suggests a framework in which the crack-growth rate is small at low strains, but diverges at failure, instead of shear-band plasticity followed by crack formation immediately prior to failure (global fracture). The latter offsets itself from a gradual internal cracking process by allowing continued shear with an intact and cohesive shear band in between the parts sliding relative to each other until fast run-away cracking is initiated.

After the XRT-experiments were completed, the still attached sample 3 was reloaded to verify the correctness of the earlier produced stress-strain data. Figure 3.27 shows that yield upon reloading reconnects well at the point of unloading of the first compression experiment, considering that MGs are sensitive to small differences in boundary conditions of subsequent tests which will affect the recorded yield stress. Furthermore, samples 1 and 2 were broken in halves using pliers to reveal their fracture surfaces without adding additional shear. The broken samples were imaged with a JEOL 6060 SEM, and the SEM images were later compared with the reconstructed shear-band cavities to confirm the correctness of XRT reconstruction and add any additional details not revealed by XRT. A SEM image of the fracture surface from the top half of sample 1 is shown in Figure 3.30a. On the left-hand side, the notch from electric discharging is seen, and on the opposite side displays a typical lip originating from a gap in the casting mold. The shear-plane fraction, as shown above via XRT (Figure 3.29a), is enclosed in the dotted yellow ellipse. Similarly, dotted contours within the ellipse indicate the main boundaries between shear-

band cavities and connected areas, as shown in Figure 3.30a. The following discussion will focus on two morphological features, enclosed in the areas highlighted in Figures 3.30b and 3.30c.

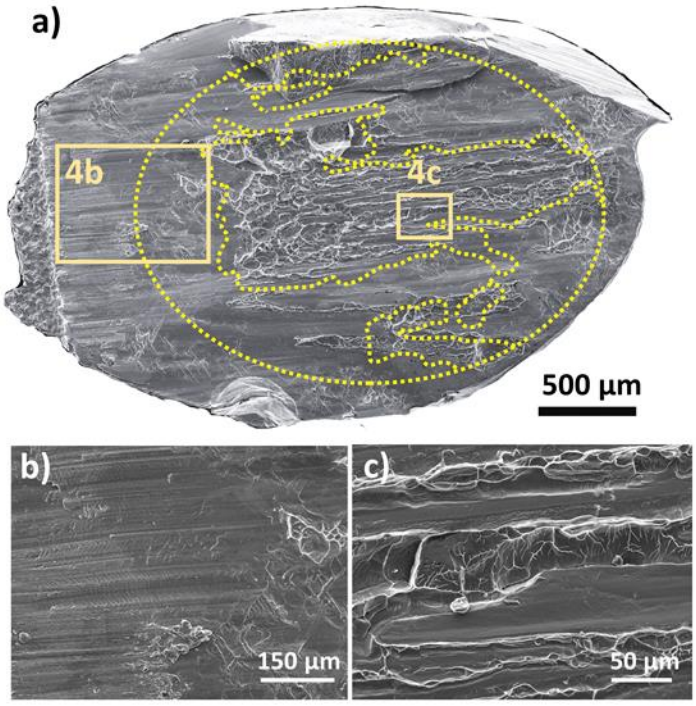

Figure 3.30. a) SEM image of the fracture surface from sample 1. Dashed lines indicate boundaries between connected and disconnected regions, as seen in Figure 3.29a. Boxes indicate the zoom-in locations for b) and c). b) Zoom-in of a detached region. c) Zoom-in of a region that was attached prior to breaking the sample in two parts.

Figure 3.30c shows the zoom-in onto the facture surface from the shear-plane fraction that was identified with XRT as being still connected, and it exhibits the typical corrugations and vein patterns known from fracture of ductile MGs, as discussed in Section 1.1.4 (Figure 1.12). On the contrary, the already separated region of the shear plane does not reveal any signature of vein patterns, as exemplified in Figure 3.30b. Instead, one sees very flat regions or regularly spaced striations that have a repeat length of ~7 µm. This length scale is in good agreement with the shear-offset magnitudes created during each serration, as reported in Reference [162]. While previous assessments of fracture surfaces from MGs always have left much room for interpretation, the combination of XRT and SEM used here allows a clear distinction between areas that underwent

abrupt fracture (vein patterns in Figure 3.30c), and those that gradually developed into a shear-band cavity (striations in Figure 3.30b). This fact has also been discussed on the basis of laboratory-based X-ray tomography experiments by Qu et al. [218, 224]. Since the amount of cavity area is different from specimen to specimen, it is expected that complex surface morphologies and patterns may be seen after fracture, where regions disconnected from the vein patterns indicate the presence of shear-band cavities.

Previous research, in particular efforts related to understanding local plastic dissipation during fracture, have paid close attention to damage void formation [128, 131, 169, 225]. In such studies, void sizes deduced from dimple morphologies or from direct void observation have been reported to be of the order of several hundred nanometers. The exception to this length scale is the work by Bouchaud et al. [226], who conducted a cross-correlation between the two facture surfaces via optical microscopy, thereby revealing a power-law scaling between damage cavity area and cavity perimeter. The data in Reference [226] includes cavity areas that suggest cavity diameters orders of magnitude larger than several hundred nanometers, and is thus in good agreement with the reported XRT data here.

The existence of a gradually increasing shear-band cavity-area while recording stress-strain curves raises questions regarding the meaning of a calculated engineering stress. Without the knowledge of the shear-band cavities revealed here, one could have argued that nano-scale voids in a shear band [128, 131, 169] do not need to be accounted for when determining stresses, and a true stress-strain curve could be derived on the basis of a changing cross-sectional area of the major shear band. Such true stress-strain curves are calculated for the $Zr_{65}Cu_{25}Al_{10}$ samples in the following subsection.

3.4.2 Calculation of true stress and explanation of apparent hardening

The macroscopic engineering stresses (σ) shown in Figure 3.27 for the three $Zr_{65}Cu_{25}Al_{10}$ MG samples were calculated simply using $\sigma = \frac{F}{A_0}$, where F is the applied uniaxial force and A_0 is the initial circular area of the cylindrical base, which remained the same throughout the compression process. However, engineering stress cannot be used to accurately determine the material property due to the unchanged initial base area. The macroscopic true stress must be calculated to assess the hardening or softening of a material during plastic deformation, where the instant load bearing area (A) replaces the initial base area (A_0). As illustrated below in Figure 3.31, the shaded area represents the instant load bearing area on the shear-band plane during compression, which keeps reducing as the top and bottom parts start shearing. According to Reference [227], this instant load bearing area is

$$A = 2r^2(\varphi - sin\varphi\ cos\varphi)\ , \tag{3.1}$$

and

$$\varphi = \cos^{-1}(\frac{l_e\varepsilon_p tan\theta}{2r})\ , \tag{3.2}$$

where r and l_e are the radius and length of the cylindrical sample at the elastic limit, ε_p is the plastic strain, and θ is the tilt angle of the shear band from the vertical axis of the cylinder shown in Figure 3.31. It was measured that $\theta \approx 45^o$ for all the compressed cylindrical samples in this work with -1° to -2° difference, so $\theta = 45^o$ was used in all the calculations.

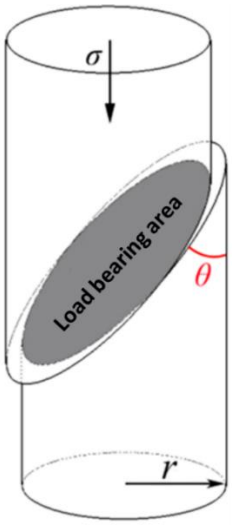

Figure 3.31. Schematic of the instant load bearing area on the shear-band plane that reduces during shearing.

The calculated true stresses based on Equations 3.1 and 3.2 are plotted together with the engineering stress-strain curves shown in Figure 3.32. Unlike the engineering stress-strain curves, which do not indicate any hardening, the calculated true stress-strain curves all show some hardening (true stress above the yield strength) of the MG samples in the very beginning of plastic deformation before softening (true stress below the yield strength). Since the true stresses shown in Figure 3.32 do not take the presumably evolving shear-band cavities into account, they are probably not a correct representation of the actual macroscopic true stresses during plastic deformation. Figures 3.28 and 3.29 indicate that the true stress at any strain may be significantly different.

The reconstruction of the cavities with XRT allowed the calculation of the actual load bearing area just before unloading. In this case, two of the three $Zr_{65}Cu_{25}Al_{10}$ samples were used for the corrected true stress calculation, as the upper shearing part of the third sample did hit the anvil during the compression test, which led to an increase in the final load that was not all carried by the final load bearing area on the shear plane. The estimation of the reduced true load bearing

area due to the inclusion of cavities was simply done by multiplying A at the final ε_p before unloading with the fraction of the still-connected area based on the top-view of the shear band plane, which is shown in Figure 3.29. Then the modified true stress before unloading was obtained using the reduced true load bearing area.

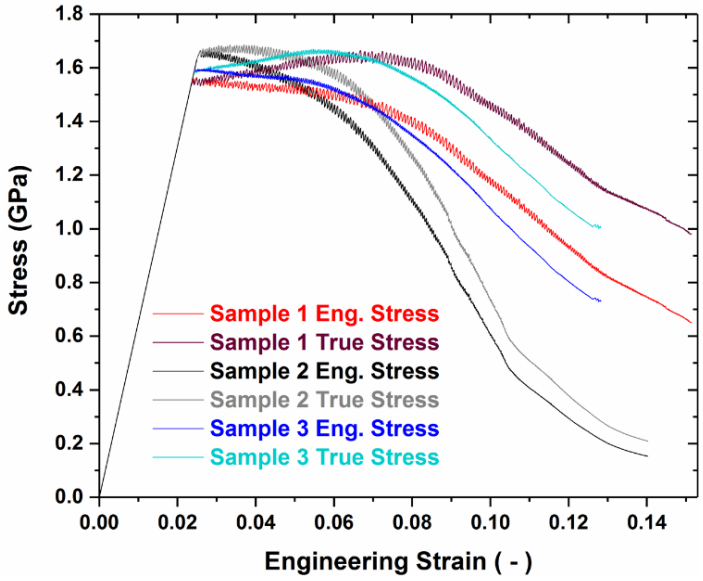

Figure 3.32. Engineering stress-strain curves and the calculated true stresses of the three $Zr_{65}Cu_{25}Al_{10}$ MG samples used for XRT. The true stress calculation did not take cavities into account.

When shear-band cavities form during serrated flow, as confirmed by acoustic emission experiments described in the following subsection, the cavity morphology shown in Figure 3.29 must be present at the point of unloading, which allows determining the reduced true load-bearing area, A_{tr}. Only samples 2 and 3 are considered here because the upper shearing part of sample 1 did hit the anvil during the compression test, as shown in Figure 3.26a. Estimating A_{tr} by multiplication with the fraction of the still connected shear-band area, yields a true stress at unloading for samples 2 and 3 of 1.7 GPa and 1.9 GPa, respectively. These values are conservative estimates, as they do treat the missing 10% of the shear-plane as still connected. Considering the same cavity fraction for the remaining 10% overlapping area, yields the more appropriate true

stress values of 2.9 GPa and 2.3 GPa for sample 2 and 3, which are shown in Figure 3.27. It should be noted that the latter values might change largely for different cavity fractions of the 10% overlapping shear area than derived from the data shown in Figure 3.39. Clearly, these stress values are distinctly larger than the yield strength of the material (~1.6 GPa) and suggests some hardening mechanism that is different than geometrical hardening [228, 229]. Two possible origins could explain this phenomenon:

(i) The shear band may harden itself, as proposed by Eckert and co-workers [227], who found a strain-hardening exponent n = 0.613 for a $Zr_{50}Cu_{44}Al_6$ alloy. Over the course of ~2.5% plastic engineering strain, this alloy hardened from 1750 MPa to 1975 MPa (~12.8%), which was explained with stress-driven densification of the shear-band material, as well as with an increase of icosahedral short-range order due to the applied pressure. A different mechanistic picture of shear-band hardening has argued for a competition between free-volume induced softening and an apparent hardening caused by an interaction stress between flow defects (possibly shear-transformation zones) close to a notch tip [230]. Both cases allude to an intrinsic hardening mechanism of the material within the shear band, which is inaccessible in our study. In fact, with the internal shear-band cavities identified in the present study, it is very likely that the stress values, and thus the hardening coefficient reported in the work by Wang et al. [227] needs to be adjusted to higher values.

(ii) The possibility of an increased resistance to shear is considered by the increase of a roughness dependent friction coefficient that becomes relevant as the internal cavity-formation process proceeds. Take into account the formation of two free surfaces that rub against each other and that have a roughness with a much larger length scale than the shear increment of an individual serration. With continued shear, it is therefore expected that the growing cavity fraction can

effectively cause an increased shear resistance due to friction. In a simplified 2D approach, as illustrated in Figure 3.33, consider an axial loading force, *F*, that causes a resolved shear force F_S and a force F_N normal to the shear plane. Resistance to shear is given by an effective drag force, F_D, that represents the required bond-breaking mechanism and viscous forces within the shear-band material to be overcome for shear without any dry friction component from the created free surfaces. Here, the magnitude of F_D is assumed constant, which means that no intrinsic hardening mechanism occurs during the shearing process. Under quasi-static loading conditions, the shear force can therefore be written as $F_S = F_D + \mu F_N$, where μF_N is the additional resistance to shear in the direction of F_D due to friction between two detached regions, and μ is the friction coefficient. With a shear-band tilt of ~ 45°, $\frac{F}{\sqrt{2}} = F_D + \mu F/\sqrt{2}$, and one can evaluate the bounds of *F* for different magnitudes of μ as F_1 and F_2. Since μ is unknown for surfaces of the MG alloy studied here with different roughness, the range reported for polished mild steel is adapted, which in the regime of low sliding velocities ($v < 1$ m/s, where shear-band propagation at room temperature has peak velocities of the order of 10^{-3} m/s [162] has shown to range between 0.07 (0.02 µm c.l.a. roughness) and 0.58 (0.6 µm c.l.a. roughness) [231]. This variation allows us to approximate a change in loading force, , $\frac{\Delta F}{F} = \frac{F_2 - F_1}{F_1}$, with $0 \leq \mu_1 < \mu_2 \leq 1$, as given by:

$$\frac{\Delta F}{F} = \frac{1-\mu_1}{1-\mu_2} - 1 > 0. \tag{3.3}$$

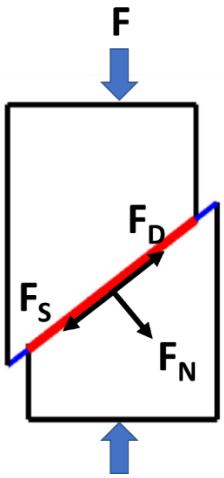

Figure 3.33. Schematic of a simplified 2D free-body diagram to illustrate the forces exerted on a shear band during uniaxial compression.

Therefore, an increase in force is needed to deform the sample, so apparent hardening may simply arise from the additional shear resistance due to dry friction from the created free surface that has increased during straining. Consequently, the apparent hardening observed after taking the cavities into account does not constitute an intrinsic structural hardening mechanism. Evaluation of Equation 3.3 yields $\frac{\Delta F}{F} = 0.075$, for $\mu_1 = 0; \mu_2 = 0.07$, and $\mu_1 = 0; \mu_2 = 0.58$ gives $\frac{\Delta F}{F} = 1.38$, where the latter is considered as the highest change in axial force based on the available values of μ (force increase by 138%). Other combinations of μ result in force increases that fall in between those two bounds (0.07 – 1.38). Using the appropriate true stress values of 2.9 GPa and 2.3 GPa for samples 2 and 3 and their corresponding load-bearing areas taken cavities into account, the μ_2 values for the two samples are estimated using Equation 3.3 and $\mu_1 = 0$. The estimated values for μ_2 for sample 2 and 3 are 0.31 and 0.26, which falls within the μ_2 range taken from the steel values as shown above. Although the friction coefficients are currently unavailable for the MGs studied here and this estimate does not consider any potential dependence of μ on F, the backward calculation results of μ_2 supports the explanation of the apparent

hardening based on friction. The approach here thus offers a straightforward pathway to understanding the observed apparent strain hardening of the MG alloy. It should be emphasized that shear-surface roughening due to internal shear-band cavities was observed in all studied samples, which suggests that this phenomenon may be rather general for MGs deformed in compression.

3.4.3 Verifying cavity formation with acoustic emission

When considering the formation of shear-band cavities, the possibility that shear-band cavities might form after the actual mechanical test cannot be excluded, because a stress-relief mechanism inside the sample after plastic deformation might lead to cracking. In order to investigate this possibility, another $Zr_{65}Cu_{25}Al_{10}$ sample was loaded with the same strain rate into the plastic regime and after every ~5 serrations, the sample was unloaded to ~30 MPa (100 N) to maintain contact with the anvils (constant load or hold segments). This stress was maintained for 48 hours, after which another ~5 serrations were accumulated by reloading. The sample was deformed to a total plastic engineering strain of ~7%, yielding an overall deformation curve very much as those from the three $Zr_{65}Cu_{25}Al_{10}$ samples shown in Figure 3.27. In conjunction with the iterative load cycles, an acoustic emission (AE) sensor was attached to the sample, and Amlan Das conducted the AE experiments following the methodology outlined in his work [101]. The goal of this approach was to investigate if any AE pulses indicative of plastic dissipative processes could be detected during the hold segments at very low stresses. Such AE pulses would indicate that shear-band cavities may also form after unloading.

The results of this in-situ AE test are summarized in Figure 3.34. A typical raw AE-pulse (named as a “hit” signal) from a shear-banding event and an event during the hold segment

identified as transient noise are displayed in Figure 3.34a. Without further detailed analysis, the comparison between both AE traces of Figure 3.34a immediately reveals a large discrepancy in amplitude, as well as much smaller frequency components in the noise-fluctuations, and both raw-pulses are displayed with identical time-axis. The in-time extended AE pulse in Figure 3.34a has been shown earlier to correspond to the plastic dissipation process of shear-band formation in MGs [66, 134, 232]. Likewise, fracture of MGs yields such pulses, which differ from shear-band formation signals by having amplitudes 2-3 orders of magnitude higher and durations of a few milliseconds as compared to the sub-millisecond regime for shear band initiation [101, 232-234]. Lastly, in terms of frequency, shear-banding pulses for the alloy studied here have characteristic frequencies in the range of 300-700 kHz, whereas fracture covers the range up to 1.5 MHz. None of the recorded AE pulses show any characteristics of those known for fracture, so the last task left is to verify that plastic processes, which emit waves similar to shear-banding, are not present during the constant load segments. Taking shear-banding pulses as an indication for a plastic process is based on the fact that inhomogeneous plasticity is expected at ambient conditions, which must begin with the formation of a shear band. Figure 3.34b shows a selection of representative AE pulses (hits) acquired throughout the serrated flow and also the constant near-zero load segments. All hold (constant load) segments contain in total 16 AE events that were not simple noise and required a more detailed analysis to confirm or refute a similarity to shear-banding pulses. The pulses displayed in Figure 3.34b show the time-integrated and normalized frequency spectrum for typical shear-band initiation events (labelled ‘S’) and also for non-noise events recorded during the constant-load holds (labelled ‘H’). A continuous wavelet analysis was used to obtain the frequency components as a function of pulse duration. The characteristic frequencies for shear banding are all well aligned within a frequency band between 600-800 kHz and exhibit sometimes

low frequency components below 400 kHz. In contrast, non-noise waves recorded during a static hold fall consistently between 400-500 kHz, being thus distinctly different from plastic processes related to shear banding. Three exceptions were identified in total, being represented by the frequency trace of hit 15 in Figure 3.34b. While these three exceptions would suggest a plastic source mechanism similar to shear banding, it is found that the absolute amplitude and the duration fall distinctly outside the values for shear-banding pulses. In fact, all non-noise pulses during hold segments are exceptionally low in amplitude and do not coincide with data-clusters obtained from shear-banding pulses.

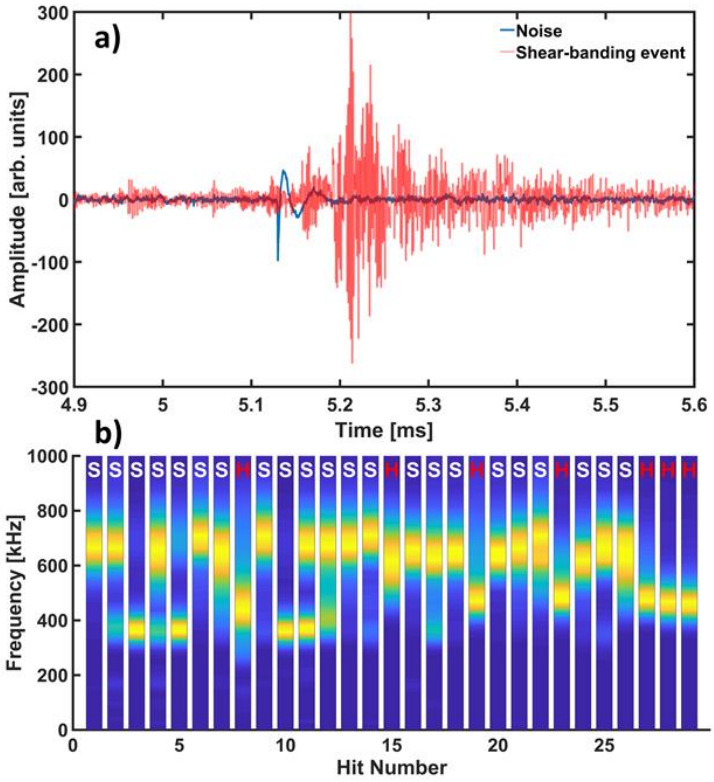

Figure 3.34. a) Representative AE pulses from a shear-banding event (red) and noise (blue). b) Frequency domains from a continuous wavelet analysis for a selected number of representative AE-hits during low-stress static hold segments. 'S' indicates events from shear banding during plastic flow, and 'H' indicates events from hold segments. (Courtesy: Amlan Das)

After the AE test, the sample was mechanically polished, and like samples 1-3, internal shear-band cavities were revealed, as shown in Figure 3.35. This analysis enables us, within the abilities of the AE method, to conclude that internal cracking or other plastic processes that normally must begin with shear banding do not occur during the hold segments. Thus, shear-band cavity formation is expected to occur in conjunction with serrated flow and not past unloading. This is in agreement with the fact that mechanical reloading long time (~3 years) after the first compression cycle and the XRT measurements does result in an engineering yield stress that reconnects well at the engineering unloading stress of the initial deformation, as seen in Figure 3.27.



Figure 3.35. Stitched SEM images showing plate-shape shear-band cavities (marked with arrows) revealed after polishing the $Zr_{65}Cu_{25}Al_{10}$ sample used for the AE test. The faint vertical contrast lines come from stitching multiple SEM images together. The thick, horizontal, and dark lines on the left and right ends of the image are cracks that indicate the shear-band surface offsets on either side of the sample.

In summary, the XRT results in this section revealed a complex structure of micron-sized cavities that shows the structural heterogeneity of shear bands in a larger length scale than the nano-scale structural fluctuations discussed in Sections 3.1-3.3. Apparent strain hardening was calculated with adjusted load-bearing area by taking the shear-band cavities into account. The hardening was ascribed to an increased resistance to shear due to roughness-dependent frictional force between sliding layers of detached shear-band material. The findings here suggest that the extensive formation of shear-band cavities has proceeded gradually during plastic deformation, adding complication to stress determination in MGs from conventionally-used external dimensions.

CHAPTER 4: CONCLUSIONS

This dissertation work is based on the hypothesis that shear-band structure in MGs would evolve with macroscopically measurable plastic strain. In search for such structural changes, three main research objectives were established, as outlined in Section 1.3. Those questions have been addressed experimentally as follows:

- *Is the structure of the nano-scale shear-band core dependent on shear strain?*

To answer this question, the initial plan was to sample nano-scale shear-band structures from a series of MG specimens uniaxially compressed to different amount of plastic strain values prior to failure. Since each specimen contained a single system-spanning shear band that mediated all the plastic strain, which could be converted to local shear strain, a comparison of shear-band structures among the series of specimens would ideally reveal the correlation between the structure of the nano-scale shear-band core and its mediated shear strain.

With this in mind, the foundational work started by first quantifying the shear-band thickness and density change compared to the surrounding matrix material in a Vit105 MG specimen uniaxially compressed to ~6% plastic strain (~10^3-10^4 in local shear strain). TEM lamellae were extracted from various locations along the path of its major system-spanning shear band. To our surprise, significant complexity was found when sampling the shear-band structure from this bulk specimen. A single system-spanning shear band revealed a large distribution of shear-band thickness values, ranging from 10 nm to 210 nm, contrary to commonly cited shear-band thickness values of ~20 nm. The shear-band density change values with respect to the matrix material, determined with HAADF-STEM, also have a large distribution from -1% to -12%. Both shear-band thickness and density change are structural properties that are strongly position

dependent for one and the same system-spanning shear band. The large scatter of shear-band thickness and density change values from the first specimen made it inefficient to continue sampling over compression specimens that produced shear bands with huge amount of shear strain.

To enlarge the shear-strain regime, a Vit105 MG bar was bent to produce shear bands with much smaller local shear strains (less than 10^2). After analyzing more than ten shear bands produced on the bent bar and also using the shear bands extracted from the compressed specimen, a strong indication was found that the shear-band thickness and density change magnitude may increase with increasing shear strain. However, it is important to note that the thickness and density change datasets throughout the large shear-strain regime show significant scatters along any single shear band. It thus turned out to be experimentally very difficult to fully answer this question of strain dependency without viewing a global trend that tolerates statistical variations. Overall, along with revealing huge local variations of the flow defect, this work supports our original hypothesis that the shear-band structure would evolve during plastic straining and suggests that damage accumulation is a predominantly a shear-driven disordering process over the tested shear-strain regime at low homologous temperatures.

- *What is the origin of density change in the nano-scale shear-band core?*

Significant density reduction in the nano-scale shear-band core has been quantified using the HAADF-STEM technique. To probe the origin of such density reduction, correlative analytical methods, including TEM-based EDX and SEND, synchrotron-based NB-XRF, and APT, were used for high-resolution compositional and structural analysis of the shear-band core. It was first shown using a Vit105 MG specimen that the elemental content in the shear band depleted proportionally, suggesting no change in shear-band composition in comparison with the

surrounding matrix. Shear-band volume dilatation was subsequently calculated with increased average interatomic spacing, further supporting that the density reduction was caused purely by structural dilatation instead of chemical segregation. In contrast to the results from the Vit105 specimen, a shear band from a different MG alloy ($Zr_{65}Cu_{25}Al_{10}$) also showed significant density reduction but did not exhibit proportional depletion of elements. Instead, it had increased Zr and Al contents and decreased Cu content, which suggested that its density reduction could result from a concurrence of chemical segregation and structural dilatation. Through the correlative chemical and structural studies on shear bands from the Vit105 and $Zr_{65}Cu_{25}Al_{10}$ MG alloys, it is clear that the origin of shear-band density change may be different from alloy to alloy. Therefore, no general conclusion can be made so far.

- *Are there any other damage signatures in the long-range shear-band region?*

Since shear bands ultimately lead to fracture in MGs through a proposed but not experimentally observed shear-band-to-crack-transition mechanism, it is of fundamental research importance to probe the shear-band evolution at a larger length scale than the nano-scale shear-band core, which, surprisingly, has not yet become a popular area of study in this field. To this end, synchrotron-based XRT was used to search for and reconstruct any micron-size cavities in the shear-band region for plastically deformed but intact Vit105 and $Zr_{65}Cu_{25}Al_{10}$ MG specimens. Substantial amount of micron-size shear-band cavities were reconstructed in 3D. Their spatial distribution indicated a significant shear-band plane roughness for each sample, suggesting that the shear-band plane in MGs is non-planar. Based on the existence of shear-band cavities in samples unloaded at different plastic strains prior to fracture, we also proposed that a gradually increasing fraction of the shear-band plane must evolve into shear-band cavities during

compression, suggesting a framework in which the crack-growth rate should be small at low plastic strains but diverges at global fracture, instead of crack formation immediately prior to failure for these MGs. Furthermore, determination of the true stress taking the cavities into account revealed apparent hardening, in contrast to the well-known shear-band softening phenomenon. Instead of ascribing an intrinsic strain-hardening mechanism to the high true stress prior to unloading, a simple model using roughness-dependent friction was proposed to account for the high axial stresses for those samples. Although in-situ observation of shear-band cavities during deformation has yet to be conducted, the findings here have started to pave a path for understanding the structural evolution of shear bands towards failure.

In conclusion, this dissertation work reports considerable amount of structural heterogeneities in MGs induced by strain localization via shear bands in both their nano-scale core and the long-range shear-band region. The former is evidenced by the large distribution of thickness and density change values within the same bulk sample and even within one nano-scale shear-band core, which may have a dependency on shear strain. The latter is evidenced by the varying spatial distribution of shear-band cavities, which must evolve gradually during plastic deformation. Such heterogeneities corroborate most recent works in the literature that indicate large structural variation in shear bands, as highlighted in Reference [11]. Further research will need to address the exact mechanism for the evolution of shear bands from the nano-scale core to the micron-size zone containing cavities, and, particularly, how to suppress the shear-band-to-crack transition in a monolithic MG. Although continued experimental characterization of structural evolution for shear bands as a function of strain will unavoidably face tremendous challenges when dealing with the fluctuations spanning over largely different length scales, it will

guide us in designing MGs that can sustain large amounts of stable plastic flow. Despite the experimental difficulties, these structural heterogeneities should eventually allow quantitative definition of structure-property relationships via measurable length scales in MGs, which is an approach that has provided valuable insight for promoting structural applications of crystalline metals.

PUBLICATIONS

C. Liu, V. Roddatis, P. Kenesei, R. Maass. Shear-band thickness and shear-band cavities in a Zr-based metallic glass, Acta Materialia 140 (2017) 206-216.

S. Küchemann, C. Liu, E.M. Dufresne, J. Shin, R. Maass. Shear banding leads to accelerated aging dynamics in a metallic glass, Physical Review B 97 (2018) 014204.

C. Liu, R. Maass. Elastic fluctuations and structural heterogeneities in metallic glasses, Advanced Functional Materials 28 (2018) 1800388.

S. Küchemann, P.M. Derlet, C. Liu, D. Rosenthal, G. Sparks, W.S. Larson, R. Maass. Energy storage in metallic glasses via flash annealing, Advanced Functional Materials 28 (2018) 1805385.

C. Liu, Z. Cai, X. Xia, V. Roddatis, R. Yuan, J. M. Zuo, R. Maass. Shear-band structure and chemistry in a Zr-based metallic glass probed with nano-beam x-ray fluorescence and transmission electron microscopy, Scripta Materialia 169 (2019) 23-27.

C. Liu, A. Das, W. Wang, S. Küchemann, P. Kenesei, R. Maass. Shear-band cavities and strain hardening in a metallic glass revealed with phase-contrast x-ray tomography, Scripta Materialia 170 (2019) 29-33.

A. Das, P.M. Derlet, C. Liu, E. Dufresne, R. Maass. Stress breaks universal aging behavior in a metallic glass, Nature Communications 10 (2019) 5006.

C. Liu, R. Maass. Strain-dependent shear-band structure in a Zr-based bulk metallic glass, to be submitted.

REFERENCES

[1] W. Klement, R.H. Willens, P. Duwez. Non-crystalline structure in solidified gold-silicon alloys, Nature 187 (1960) 869-870.

[2] W.H. Wang, C. Dong, C.H. Shek. Bulk metallic glasses, Materials Science and Engineering R 44 (2004) 45-89.

[3] M.F. Ashby, A.L. Greer. Metallic glasses as structural materials, Scripta Materialia 54 (2006) 321-326.

[4] C. Schuh, T. Hufnagel, U. Ramamurty. Mechanical behavior of amorphous alloys, Acta Materialia 55 (2007) 4067-4109.

[5] M. Telford. The case for bulk metallic glass, Materials Today 7 (2004) 36-43.

[6] M.M. Khan, A. Nemati, Z.U. Rahman, U.H. Shah, H. Asgar, W. Haider. Recent advancements in bulk metallic glasses and their applications: A review, Critical Reviews in Solid State and Materials Sciences 43 (2018) 233-268.

[7] A. Wiest, J.S. Harmon, M.D. Demetriou, R. Dale Conner, W.L. Johnson. Injection molding metallic glass, Scripta Materialia 60 (2009) 160-163.

[8] D. Weaire, M.F. Ashby, J. Logan, M.J. Weins. On the use of pair potentials to calculate the properties of amorphous metals, Acta Metallurgica 19 (1971) 779-788.

[9] D.B. Miracle. The density and packing fraction of binary metallic glasses, Acta Materialia 61 (2013) 3157-3171.

[10] G. Schoeck. Dislocation Theory of Plasticity of Metals, Advances in Applied Mechanics 4 (1956) 229-279.

[11] C. Liu, R. Maass. Elastic fluctuations and structural heterogeneities in metallic glasses, Advanced Functional Materials 28 (2018) 1800388.

[12] Y.Q. Cheng, E. Ma. Atomic-level structure and structure–property relationship in metallic glasses, Progress in Materials Science 56 (2011) 379-473.

[13] D. Turnbull. Under what conditions can a glass be formed?, Contemporary Physics 10 (1969) 473-488.

[14] A. Inoue. High-strength bulk amorphous-alloys with low critical cooling rates, Materials Transactions, JIM 36 (1995) 866-875.

[15] A. Inoue. Stabilization of metallic supercooled liquid and bulk amorphous alloys, Acta Materialia 48 (2000) 279-306.

[16] A. Inoue. Bulk amorphous and nanocrystalline alloys with high functional properties, Materials Science and Engineering A 304 (2001) 1-10.

[17] A. Inoue, N. Nishiyama. Extremely low critical cooling rates of new Pd-Cu-P base amorphous alloys, Materials Science and Engineering A 226-228 (1997) 401-405.

[18] A.Q. Tool, C.G. Eicitlin. Variations caused in the heating curves of glass by heat treatment, Journal of the American Ceramic Society 14 (1931) 276-308.

[19] A.E. Geissberger, F.L. Galeener. Raman studies of vitreous SiO_2 versus fictive temperature, Physical Review B 28 (1983) 3266-3271.

[20] G. Kumar, P. Neibecker, Y.H. Liu, J. Schroers. Critical fictive temperature for plasticity in metallic glasses, Nature Communications 4 (2013) 1536.

[21] Y. Zhang, D.Q. Zhao, R.J. Wang, W.H. Wang. Formation and properties of $Zr_{48}Nb_8Cu_{14}Ni_{12}Be_{18}$ bulk metallic glass, Acta Materialia 51 (2003) 1971-1979.

[22] U. Harms, O. Jin, R.B. Schwarz. Effects of plastic deformation on the elastic modulus and density of bulk amorphous $Pd_{40}Ni_{10}Cu_{30}P_{20}$, Journal of Non-Crystalline Solids 317 (2003) 200-205.

[23] D. Xu, G. Duan, W.L. Johnson, C. Garland. Formation and properties of new Ni-based amorphous alloys with critical casting thickness up to 5 mm, Acta Materialia 52 (2004) 3493-3497.

[24] D. Xu, G. Duan, W.L. Johnson. Unusual glass-forming ability of bulk amorphous alloys based on ordinary metal copper, Physical Review Letters 92 (2004) 245504.

[25] H.S. Chen, J.T. Krause, E. Coleman. Elastic constants, hardness and their implications to flow properties of metallic glasses, Journal of Non-Crystalline Solids 18 (1975) 157-171.

[26] E. Ma. Tuning order in disorder, Nature Materials 14 (2015) 547-552.

[27] J.D. Bernal. The structure of liquids, Proceedings of the Royal Society of London A, Mathematical and Physical Sciences 280 (1964) 299-322.

[28] J. Ding, S. Patinet, M.L. Falk, Y. Cheng, E. Ma. Soft spots and their structural signature in a metallic glass, Proceedings of the National Academy of Sciences 111 (2014) 14052.

[29] Y.Q. Cheng, E. Ma, H.W. Sheng. Alloying strongly influences the structure, dynamics, and glass forming ability of metallic supercooled liquids, Applied Physics Letters 93 (2008) 111913.

[30] Y.Q. Cheng, A.J. Cao, H.W. Sheng, E. Ma. Local order influences initiation of plastic flow in metallic glass: Effects of alloy composition and sample cooling history, Acta Materialia 56 (2008) 5263-5275.

[31] Y.Q. Cheng, E. Ma. Indicators of internal structural states for metallic glasses: Local order, free volume, and configurational potential energy, Applied Physics Letters 93 (2008) 051910.

[32] D.B. Miracle. A structural model for metallic glasses, Nature Materials 3 (2004) 697-702.

[33] D.B. Miracle. The efficient cluster packing model – An atomic structural model for metallic glasses, Acta Materialia 54 (2006) 4317-4336.

[34] J. Hwang, P.M. Voyles. Variable resolution fluctuation electron microscopy on Cu-Zr metallic glass using a wide range of coherent STEM probe size, Microscopy and Microanalysis 17 (2010) 67-74.

[35] Y.H. Liu, D. Wang, K. Nakajima, W. Zhang, A. Hirata, T. Nishi, A. Inoue, M.W. Chen. Characterization of nanoscale mechanical heterogeneity in a metallic glass by dynamic force microscopy, Physical Review Letters 106 (2011) 125504.

[36] F. Zhu, H.K. Nguyen, S.X. Song, D.P.B. Aji, A. Hirata, H. Wang, K. Nakajima, M.W. Chen. Intrinsic correlation between β-relaxation and spatial heterogeneity in a metallic glass, Nature Communications 7 (2016) 11516.

[37] P. Ross, S. Küchemann, P.M. Derlet, H. Yu, W. Arnold, P. Liaw, K. Samwer, R. Maass. Linking macroscopic rejuvenation to nano-elastic fluctuations in a metallic glass, Acta Materialia 138 (2017) 111-118.

[38] H. Wagner, D. Bedorf, S. Küchemann, M. Schwabe, B. Zhang, W. Arnold, K. Samwer. Local elastic properties of a metallic glass, Nature Materials 10 (2011) 439-442.

[39] P. Tsai, K. Kranjc, K.M. Flores. Hierarchical heterogeneity and an elastic microstructure observed in a metallic glass alloy, Acta Materialia 139 (2017) 11-20.

[40] D. Tönnies, K. Samwer, P.M. Derlet, C.A. Volkert, R. Maass. Rate-dependent shear-band initiation in a metallic glass, Applied Physics Letters 106 (2015) 171907.

[41] H.U. Künzi. Mechanical properties of metallic glasses, in: H. Beck, H.-J. Güntherodt, Glassy Metal II: Atomic Structure and Dynamics, Electronic Structure, Magnetic Properties, Springer (1983), 169-216.

[42] G. Knuyt, L.D. Schepper, L.M. Stals. Calculation of elastic constants for an amorphous metal and the influence of relaxation, Journal of Physics F: Metal Physics 16 (1986) 1989-2006.

[43] W.H. Wang. The elastic properties, elastic models and elastic perspectives of metallic glasses, Progress in Materials Science 57 (2012) 487-656.

[44] T.C. Hufnagel, C.A. Schuh, M.L. Falk. Deformation of metallic glasses: Recent developments in theory, simulations, and experiments, Acta Materialia 109 (2016) 375-393.

[45] W.L. Johnson, K. Samwer. A universal criterion for plastic yielding of metallic glasses with a $(T/T_g)^{2/3}$ temperature dependence, Physical Review Letters 95 (2005) 195501.

[46] L. Tian, Y.-Q. Cheng, Z.-W. Shan, J. Li, C.-C. Wang, X.-D. Han, J. Sun, E. Ma. Approaching the ideal elastic limit of metallic glasses, Nature Communications 3 (2012) 609.

[47] A. Inoue, N. Nishiyama. New bulk metallic glasses for applications as magnetic-sensing, chemical, and structural materials, MRS Bulletin 32 (2011) 651-658.

[48] D. Gritti, T. Gyger, V. Von Niederhausern.Method for shaping a barrel spring made of metallic glass. (2014) US 8720246

[49] N. Nishiyama, K. Amiya, A. Inoue. Recent progress of bulk metallic glasses for strain-sensing devices, Materials Science and Engineering A 449-451 (2007) 79-83.

[50] W.L. Johnson, D.S. Lee, M.D. Demetriou, J.H. Na, G. Garrettt.Golf club fabricated from bulk metallic glasses with high toughness and high stiffness. (2014) US 20140213384

[51] A.S. Argon. Plastic deformation in metallic glasses, Acta Metallurgica 27 (1979) 47-58.

[52] F. Spaepen. A microscopic mechanism for steady state inhomogeneous flow in metallic glasses, Acta Metallurgica 25 (1977) 407-415.

[53] J. Schroers, T. Nguyen, S. O'Keeffe, A. Desai. Thermoplastic forming of bulk metallic glass—Applications for MEMS and microstructure fabrication, Materials Science and Engineering A 449-451 (2007) 898-902.

[54] N. Li, W. Chen, L. Liu. Thermoplastic micro-forming of bulk metallic glasses: a review, JOM 68 (2016) 1246-1261.

[55] T.G. Nieh, J. Wadsworth. Homogeneous deformation of bulk metallic glasses, Scripta Materialia 54 (2006) 387-392.

[56] M.A. Meyers, K.K. Chawla. Mechanical Behavior of Materials, 2nd Edition, Cambridge University Press (2009).

[57] W. Cai, V.V. Bulatov, J. Chang, J. Li, S. Yip. Dislocation core effects on mobility, Dislocations in solids 12 (2004) 1-80.

[58] E. Bouchbinder, J.S. Langer, I. Procaccia. Athermal shear-transformation-zone theory of amorphous plastic deformation. I. Basic principles, Physical Review E 75 (2007) 036107.

[59] M.L. Falk, J.S. Langer. Dynamics of viscoplastic deformation in amorphous solids, Physical Review E 57 (1998) 7192-7205.

[60] D. Rodney, C. Schuh. Distribution of thermally activated plastic events in a flowing glass, Physical Review Letters 102 (2009) 235503.

[61] S.G. Mayr. Activation energy of shear transformation zones: a key for understanding rheology of glasses and liquids, Physical Review Letters 97 (2006) 195501.

[62] J. Frenkel. Zur Theorie der Elastizitätsgrenze und der Festigkeit kristallinischer Körper, Zeitschrift für Physik 37 (1926) 572-609.

[63] P.M. Derlet, R. Maass. Linking high- and low-temperature plasticity in bulk metallic glasses: thermal activation, extreme value statistics and kinetic freezing, Philosophical Magazine 93 (2013) 4232-4263.

[64] J. Lu, G. Ravichandran, W.L. Johnson. Deformation behavior of the $Zr_{41.2}Ti_{13.8}Cu_{12.5}Ni_{10}Be_{22.5}$ bulk metallic glass over a wide range of strain-rates and temperatures, Acta Materialia 51 (2003) 3429-3443.

[65] A.L. Greer, Y.Q. Cheng, E. Ma. Shear bands in metallic glasses, Materials Science and Engineering R 74 (2013) 71-132.

[66] R. Maass, J.F. Löffler. Shear-band dynamics in metallic glasses, Advanced Functional Materials 25 (2015) 2353-2368.

[67] R.D. Conner, W.L. Johnson, N.E. Paton, W.D. Nix. Shear bands and cracking of metallic glass plates in bending, Journal of Applied Physics 94 (2003) 904-911.

[68] Z.F. Zhang, J. Eckert, L. Schultz. Difference in compressive and tensile fracture mechanisms of $Zr_{59}Cu_{20}Al_{10}Ni_8Ti_3$ bulk metallic glass, Acta Materialia 51 (2003) 1167-1179.

[69] C. Ma, H. Soejima, S. Ishihara, K. Amiya, N. Nishiyama, A. Inoue. New Ti-based bulk glassy alloys with high glass-forming ability and superior mechanical properties, Materials Transactions 45 (2004) 3223-3227.

[70] H. Li, C. Fan, K. Tao, H. Choo, P.K. Liaw. Compressive behavior of a Zr-based metallic glass at cryogenic temperatures, Advanced Materials 18 (2006) 752-754.

[71] J. Yi, S.M. Seifi, W. Wang, J.J. Lewandowski. A damage-tolerant bulk metallic glass at liquid-nitrogen temperature, Journal of Materials Science & Technology 30 (2014) 627-630.

[72] D. Pan, H. Guo, W. Zhang, A. Inoue, M.W. Chen. Temperature-induced anomalous brittle-to-ductile transition of bulk metallic glasses, Applied Physics Letters 99 (2011) 241907.

[73] Z. Han, W.F. Wu, Y. Li, Y.J. Wei, H.J. Gao. An instability index of shear band for plasticity in metallic glasses, Acta Materialia 57 (2009) 1367-1372.

[74] F.F. Wu, Z.F. Zhang, S.X. Mao. Size-dependent shear fracture and global tensile plasticity of metallic glasses, Acta Materialia 57 (2009) 257-266.

[75] Y. Wu, H.X. Li, Z.Y. Liu, G.L. Chen, Z.P. Lu. Interpreting size effects of bulk metallic glasses based on a size-independent critical energy density, Intermetallics 18 (2010) 157-160.

[76] F.F. Wu, Z.F. Zhang, S.X. Mao, J. Eckert. Effect of sample size on ductility of metallic glass, Philosophical Magazine Letters 89 (2009) 178-184.

[77] X.J. Gu, A.G. McDermott, S.J. Poon, G.J. Shiflet. Critical Poisson's ratio for plasticity in Fe–Mo–C–B–Ln bulk amorphous steel, Applied Physics Letters 88 (2006) 211905.

[78] A. Castellero, D.I. Uhlenhaut, B. Moser, J.F. Löffler. Critical Poisson ratio for room-temperature embrittlement of amorphous $Mg_{85}Cu_5Y_{10}$, Philosophical Magazine Letters 87 (2007) 383-392.

[79] S.J. Poon, A. Zhu, G.J. Shiflet. Poisson's Ratio and intrinsic plasticity of metallic glasses, Applied Physics Letters 92 (2008) 261902.

[80] J.J. Lewandowski, W.H. Wang, A.L. Greer. Intrinsic plasticity or brittleness of metallic glasses, Philosophical Magazine Letters 85 (2005) 77-87.

[81] Z.Q. Liu, Z.F. Zhang. Strengthening and toughening metallic glasses: The elastic perspectives and opportunities, Journal of Applied Physics 115 (2014) 163505.

[82] H.-E.d. Tresca. Sur l'écoulement des corps solides soumis à une forte pression, Gauthier-Villars, Paris (1867).

[83] R.v. Mises. Mechanik der festen Körper im plastisch-deformablen Zustand, Nachrichten von der Gesellschaft der Wissenschaften zu Göttingen, Mathematisch-Physikalische Klasse 1913 (1913) 582-592.

[84] P.E. Donovan. A yield criterion for $Pd_{40}Ni_{40}P_{20}$ metallic glass, Acta Metallurgica 37 (1989) 445-456.

[85] A.C. Lund, C.A. Schuh. The Mohr–Coulomb criterion from unit shear processes in metallic glass, Intermetallics 12 (2004) 1159-1165.

[86] P.B. Bowden, J.A. Jukes. The plastic flow of isotropic polymers, Journal of Materials Science 7 (1972) 52-63.

[87] R.E. Means, J.V. Parcher. Physical Properties of Soils, C. E. Merrill Books (1963).

[88] M.S. Paterson. Experimental Rock Deformation: The Brittle Field, Springer (1978).

[89] P.W. Rowe, G.I. Taylor. The stress-dilatancy relation for static equilibrium of an assembly of particles in contact, Proceedings of the Royal Society of London A, Mathematical and Physical Sciences 269 (1962) 500-527.

[90] M. Zhao, M. Li. Interpreting the change in shear band inclination angle in metallic glasses, Applied Physics Letters 93 (2008) 241906.

[91] M. Zhao, M. Li. A constitutive theory and modeling on deviation of shear band inclination angles in bulk metallic glasses, Journal of Materials Research 24 (2011) 2688-2696.

[92] Y.F. Gao, L. Wang, H. Bei, T.G. Nieh. On the shear-band direction in metallic glasses, Acta Materialia 59 (2011) 4159-4167.

[93] C.T. Liu, L. Heatherly, J.A. Horton, D.S. Easton, C.A. Carmichael, J.L. Wright, J.H. Schneibel, M.H. Yoo, C.H. Chen, A. Inoue. Test environments and mechanical properties of Zr-base bulk amorphous alloys, Metallurgical and Materials Transactions A 29 (1998) 1811-1820.

[94] J.J. Lewandowski, P. Lowhaphandu. Effects of hydrostatic pressure on the flow and fracture of a bulk amorphous metal, Philosophical Magazine A 82 (2002) 3427-3441.

[95] H. Rosner, M. Peterlechner, C. Kubel, V. Schmidt, G. Wilde. Density changes in shear bands of a metallic glass determined by correlative analytical transmission electron microscopy, Ultramicroscopy 142 (2014) 1-9.

[96] V. Schmidt, H. Rosner, M. Peterlechner, G. Wilde, P.M. Voyles. Quantitative measurement of density in a shear band of metallic glass monitored along its propagation direction, Physical Review Letters 115 (2015) 035501.

[97] R. Maass, P. Birckigt, C. Borchers, K. Samwer, C.A. Volkert. Long range stress fields and cavitation along a shear band in a metallic glass: The local origin of fracture, Acta Materialia 98 (2015) 94-102.

[98] C. Liu, V. Roddatis, P. Kenesei, R. Maass. Shear-band thickness and shear-band cavities in a Zr-based metallic glass, Acta Materialia 140 (2017) 206-216.

[99] J. Pan, Q. Chen, L. Liu, Y. Li. Softening and dilatation in a single shear band, Acta Materialia 59 (2011) 5146-5158.

[100] J.J. Lewandowski, A.L. Greer. Temperature rise at shear bands in metallic glasses, Nature Materials 5 (2006) 15-18.

[101] A. Das, P. Kagebein, S. Kuchemann, R. Maass. Temperature rise from fracture in a Zr-based metallic glass, Applied Physics Letters 112 (2018) 261905

[102] B.A. Sun, W.H. Wang. The fracture of bulk metallic glasses, Progress in Materials Science 74 (2015) 211-307.

[103] R. Narasimhan, P. Tandaiya, I. Singh, R.L. Narayan, U. Ramamurty. Fracture in metallic glasses: mechanics and mechanisms, International Journal of Fracture 191 (2015) 53-75.

[104] D.L. Henann, L. Anand. Fracture of metallic glasses at notches: Effects of notch-root radius and the ratio of the elastic shear modulus to the bulk modulus on toughness, Acta Materialia 57 (2009) 6057-6074.

[105] J. Xu, U. Ramamurty, E. Ma. The fracture toughness of bulk metallic glasses, JOM 62 (2010) 10-18.

[106] B. Gludovatz, S.E. Naleway, R.O. Ritchie, J.J. Kruzic. Size-dependent fracture toughness of bulk metallic glasses, Acta Materialia 70 (2014) 198-207.

[107] J. Schroers, W.L. Johnson. Ductile bulk metallic glass, Physical Review Letters 93 (2004) 255506.

[108] C.J. Gilbert, R.O. Ritchie, W.L. Johnson. Fracture toughness and fatigue-crack propagation in a Zr–Ti–Ni–Cu–Be bulk metallic glass, Applied Physics Letters 71 (1997) 476-478.

[109] D.G. Pan, H.F. Zhang, A.M. Wang, Z.G. Wang, Z.Q. Hu. Fracture instability in brittle Mg-based bulk metallic glasses, Journal of Alloys and Compounds 438 (2007) 145-149.

[110] Y.T. Wang, X.K. Xi, G. Wang, X.X. Xia, W.H. Wang. Understanding of nanoscale periodic stripes on fracture surface of metallic glasses, Journal of Applied Physics 106 (2009) 113528.

[111] S.F. Pugh. XCII. Relations between the elastic moduli and the plastic properties of polycrystalline pure metals, The London, Edinburgh, and Dublin Philosophical Magazine and Journal of Science 45 (1954) 823-843.

[112] B.A. Sun, J. Tan, S. Pauly, U. Kühn, J. Eckert. Stable fracture of a malleable Zr-based bulk metallic glass, Journal of Applied Physics 112 (2012) 103533.

[113] D. Hull. Fractography: Observing, Measuring and Interpreting Fracture Surface Topography, Cambridge University Press (1999).

[114] Z.F. Zhang, F.F. Wu, W. Gao, J. Tan, Z.G. Wang, M. Stoica, J. Das, J. Eckert, B.L. Shen, A. Inoue. Wavy cleavage fracture of bulk metallic glass, Applied Physics Letters 89 (2006) 251917.

[115] R.L. Narayan, P. Tandaiya, R. Narasimhan, U. Ramamurty. Wallner lines, crack velocity and mechanisms of crack nucleation and growth in a brittle bulk metallic glass, Acta Materialia 80 (2014) 407-420.

[116] A.S. Argon, M. Salama. The mechanism of fracture in glassy materials capable of some inelastic deformation, Materials Science and Engineering 23 (1976) 219-230.

[117] P. Murali, U. Ramamurty. Embrittlement of a bulk metallic glass due to sub-Tg annealing, Acta Materialia 53 (2005) 1467-1478.

[118] H. Choi-Yim, W.L. Johnson. Bulk metallic glass matrix composites, Applied Physics Letters 71 (1997) 3808-3810.

[119] T. Masumoto, R. Maddin. The mechanical properties of palladium 20 a/o silicon alloy quenched from the liquid state, Acta Metallurgica 19 (1971) 725-741.

[120] Y. Zhang, A.L. Greer. Thickness of shear bands in metallic glasses, Applied Physics Letters 89 (2006) 071907.

[121] C.A. Pampillo, H.S. Chen. Comprehensive plastic-deformation of a bulk metallic glass Materials Science and Engineering 13 (1974) 181-188.

[122] D. Klaumünzer, A. Lazarev, R. Maass, F.H. Dalla Torre, A. Vinogradov, J.F. Loffler. Probing shear-band initiation in metallic glasses, Physical Review Letters 107 (2011) 185502.

[123] Y.M. Chen, T. Ohkubo, T. Mukai, K. Hono. Structure of shear bands in $Pd_{40}Ni_{40}P_{20}$ bulk metallic glass, Journal of Materials Research 24 (2011) 1-9.

[124] W. Guo, B. Gan, J.M. Molina-Aldareguia, J.D. Poplawsky, D. Raabe. Structure and dynamics of shear bands in amorphous–crystalline nanolaminates, Scripta Materialia 110 (2016) 28-32.

[125] A.H. Hunter, V. Araullo-Peters, M. Gibbons, O.D. Restrepo, S.R. Niezgoda, W. Windl, K.M. Flores, D.C. Hofmann, E.A. Marquis. Three-dimensional imaging of shear bands in bulk metallic glass composites, Journal of Microscopy 264 (2016) 304-310.

[126] S. Balachandran, J. Orava, M. Kohler, A.J. Breen, I. Kaban, D. Raabe, M. Herbig. Elemental re-distribution inside shear bands revealed by correlative atom-probe tomography and electron microscopy in a deformed metallic glass, Scripta Materialia 168 (2019) 14-18.

[127] H. Chen, Y. He, G.J. Shiflet, S.J. Poon. Deformation-induced nanocrystal formation in shear bands of amorphous alloys, Nature 367 (1994) 541-543.

[128] W. Jiang, M. Atzmon. Mechanically-assisted nanocrystallization and defects in amorphous alloys: A high-resolution transmission electron microscopy study, Scripta Materialia 54 (2006) 333-336.

[129] G. Wilde, H. Rösner. Nanocrystallization in a shear band: An in situ investigation, Applied Physics Letters 98 (2011) 251904.

[130] Z. Yan, K. Song, Y. Hu, F. Dai, Z. Chu, J. Eckert. Localized crystallization in shear bands of a metallic glass, Scientific Reports 6 (2016) 19358.

[131] J. Li, F. Spaepen, T.C. Hufnagel. Nanometre-scale defects in shear bands in a metallic glass, Philosophical Magazine A 82 (2002) 2623-2630.

[132] Y. Shao, G.-N. Yang, K.-F. Yao, X. Liu. Direct experimental evidence of nano-voids formation and coalescence within shear bands, Applied Physics Letters 105 (2014) 181909.

[133] A.C.Y. Liu, D.M. Paganin, L. Bourgeois, P.N.H. Nakashima, R.T. Ott, M.J. Kramer. Quantitative microscopic measurement of void distribution in shear bands in $Zr_{66.7}Cu_{33.3}$ metallic glass, Physical Review B 84 (2011) 094201.

[134] W.J. Wright, T.C. Hufnagel, W.D. Nix. Free volume coalescence and void formation in shear bands in metallic glass, Journal of Applied Physics 93 (2003) 1432-1437.

[135] A.R. Hinkle, C.H. Rycroft, M.D. Shields, M.L. Falk. Coarse graining atomistic simulations of plastically deforming amorphous solids, Physical Review E 95 (2017) 053001.

[136] P.E. Donovan, W.M. Stobbs. The structure of shear bands in metallic glasses, Acta Metallurgica 29 (1981) 1419-1436.

[137] E. Pekarskaya, C.P. Kim, W.L. Johnson. In situ transmission electron microscopy studies of shear bands in a bulk metallic glass based composite, Journal of Materials Research 16 (2011) 2513-2518.

[138] H.S. Shahabi, S. Scudino, I. Kaban, M. Stoica, B. Escher, S. Menzel, G.B.M. Vaughan, U. Kühn, J. Eckert. Mapping of residual strains around a shear band in bulk metallic glass by nanobeam X-ray diffraction, Acta Materialia 111 (2016) 187-193.

[139] S. Scudino, R.N. Shahid, B. Escher, M. Stoica, B.S. Li, J.J. Kruzic. Mapping the cyclic plastic zone to elucidate the mechanisms of crack tip deformation in bulk metallic glasses, Applied Physics Letters 110 (2017) 081903.

[140] A. Vinogradov, M. Seleznev, I.S. Yasnikov. Dislocation characteristics of shear bands in metallic glasses, Scripta Materialia 130 (2017) 138-142.

[141] I. Binkowski, S. Schlottbom, J. Leuthold, S. Ostendorp, S.V. Divinski, G. Wilde. Sub-micron strain analysis of local stick-slip motion of individual shear bands in a bulk metallic glass, Applied Physics Letters 107 (2015) 221902.

[142] H. Bei, S. Xie, E.P. George. Softening caused by profuse shear banding in a bulk metallic glass, Physical Review Letters 96 (2006) 105503.

[143] R. Bhowmick, R. Raghavan, K. Chattopadhyay, U. Ramamurty. Plastic flow softening in a bulk metallic glass, Acta Materialia 54 (2006) 4221-4228.

[144] L. Wang, H. Bei, Y.F. Gao, Z.P. Lu, T.G. Nieh. Effect of residual stresses on the onset of yielding in a Zr-based metallic glass, Acta Materialia 59 (2011) 7627-7633.

[145] T.Y. Tsui, W.C. Oliver, G.M. Pharr. Influences of stress on the measurement of mechanical properties using nanoindentation: Part I. Experimental studies in an aluminum alloy, Journal of Materials Research 11 (2011) 752-759.

[146] N. Hu, J.F. Molinari. Shear bands in dense metallic granular materials, Journal of the Mechanics and Physics of Solids 52 (2004) 499-531.

[147] Q. Wei, D. Jia, K.T. Ramesh, E. Ma. Evolution and microstructure of shear bands in nanostructured Fe, Applied Physics Letters 81 (2002) 1240-1242.

[148] R.N. Haward. The Physics of Glassy Polymers, Springer Science & Business Media (2012).

[149] H. Kimura, T. Masumoto. A model of the mechanics of shear-crack propagation in tearing for amorphous metals I. Critical shear stress for inhomogeneous flow, Philosophical Magazine A 44 (1981) 1005-1020.

[150] H. Kimura, T. Masumoto. A model of the mechanics of shear-crack propagation in tearing for amorphous metals II. Kinetics of inhomogeneous flow, Philosophical Magazine A 44 (1981) 1021-1030.

[151] H. Kimura, T. Masumoto. A model of the mechanics of serrated flow in an amorphous alloy, Acta Metallurgica 31 (1983) 231-240.

[152] D. Klaumünzer, R. Maass, J.F. Löffler. Stick-slip dynamics and recent insights into shear banding in metallic glasses, Journal of Materials Research 26 (2011) 1453-1463.

[153] A. Dubach, F.H. Dalla Torre, J.F. Löffler. Constitutive model for inhomogeneous flow in bulk metallic glasses, Acta Materialia 57 (2009) 881-892.

[154] S. Ogata, F. Shimizu, J. Li, M. Wakeda, Y. Shibutani. Atomistic simulation of shear localization in Cu–Zr bulk metallic glass, Intermetallics 14 (2006) 1033-1037.

[155] F. Shimizu, S. Ogata, J. Li. Yield point of metallic glass, Acta Materialia 54 (2006) 4293-4298.

[156] B. Yang, M.L. Morrison, P.K. Liaw, R.A. Buchanan, G. Wang, C.T. Liu, M. Denda. Dynamic evolution of nanoscale shear bands in a bulk-metallic glass, Applied Physics Letters 86 (2005) 141904.

[157] B. Yang, C.T. Liu, T.G. Nieh, M.L. Morrison, P.K. Liaw, R.A. Buchanan. Localized heating and fracture criterion for bulk metallic glasses, Journal of Materials Research 21 (2006) 915-922.

[158] E.R. Homer. Examining the initial stages of shear localization in amorphous metals, Acta Materialia 63 (2014) 44-53.

[159] Y.Q. Cheng, Z. Han, Y. Li, E. Ma. Cold versus hot shear banding in bulk metallic glass, Physical Review B 80 (2009) 134115.

[160] A.J. Cao, Y.Q. Cheng, E. Ma. Structural processes that initiate shear localization in metallic glass, Acta Materialia 57 (2009) 5146-5155.

[161] D.B. Miracle, A. Concustell, Y. Zhang, A.R. Yavari, A.L. Greer. Shear bands in metallic glasses: Size effects on thermal profiles, Acta Materialia 59 (2011) 2831-2840.

[162] R. Maass, D. Klaumünzer, J.F. Löffler. Propagation dynamics of individual shear bands during inhomogeneous flow in a Zr-based bulk metallic glass, Acta Materialia 59 (2011) 3205-3213.

[163] W.J. Wright, R.R. Byer, X. Gu. High–speed imaging of a bulk metallic glass during uniaxial compression, Applied Physics Letters 102 (2013) 241920.

[164] S.X. Song, X.L. Wang, T.G. Nieh. Capturing shear band propagation in a Zr-based metallic glass using a high-speed camera, Scripta Materialia 62 (2010) 847-850.

[165] P. Thurnheer, R. Maass, S. Pogatscher, J.F. Loffler. Compositional dependence of shear-band dynamics in the Zr-Cu-Al bulk metallic glass system, Applied Physics Letters 104 (2014) 101910.

[166] E.G. Daub, D. Klaumünzer, J.F. Löffler. Effective temperature dynamics of shear bands in metallic glasses, Physical Review E 90 (2014) 062405.

[167] J. Ding, Y.-Q. Cheng, E. Ma. Full icosahedra dominate local order in $Cu_{64}Zr_{34}$ metallic glass and supercooled liquid, Acta Materialia 69 (2014) 343-354.

[168] P.D. Miller, J.M. Gibson. Connecting small-angle diffraction with real-space images by quantitative transmission electron microscopy of amorphous thin-films, Ultramicroscopy 74 (1998) 221-235.

[169] S. Pauly, M.H. Lee, D.H. Kim, K.B. Kim, D.J. Sordelet, J. Eckert. Crack evolution in bulk metallic glasses, Journal of Applied Physics 106 (2009) 103518.

[170] P. Tandaiya, R. Narasimhan, U. Ramamurty. On the mechanism and the length scales involved in the ductile fracture of a bulk metallic glass, Acta Materialia 61 (2013) 1558-1570.

[171] R.T. Qu, M. Stoica, J. Eckert, Z.F. Zhang. Tensile fracture morphologies of bulk metallic glass, Journal of Applied Physics 108 (2010) 063509.

[172] I. Singh, R. Narasimhan, U. Ramamurty. Cavitation-induced fracture causes nanocorrugations in brittle metallic glasses, Physical Review Letters 117 (2016) 044302.

[173] D. Klaumünzer, R. Maass, F.H.D. Torre, J.F. Löffler. Temperature-dependent shear band dynamics in a Zr-based bulk metallic glass, Applied Physics Letters 96 (2010) 061901.

[174] C. Liu, Z. Cai, X. Xia, V. Roddatis, R. Yuan, J.M. Zuo, R. Maass. Shear-band structure and chemistry in a Zr-based metallic glass probed with nano-beam x-ray fluorescence and transmission electron microscopy, Scripta Materialia 169 (2019) 23-27.

[175] C. Liu, A. Das, W. Wang, S. Kuchemann, P. Kenesei, R. Maass. Shear-band cavities and strain hardening in a metallic glass revealed with phase-contrast x-ray tomography, Scripta Materialia 170 (2019) 29-33.

[176] P. Thurnheer. Dynamics and temperature of shear banding in metallic glasses, Department of Materials, ETH Zurich (2015).

[177] T. Zhang, A. Inoue, T. Masumoto. Amorphous Zr-Al-TM (TM=Co, Ni, Cu) alloys with significant supercooled liquid region of over 100 K, Materials Transactions, JIM 32 (1991) 1005-1010.

[178] P. Walker, W.H. Tarn. Handbook of Metal Etchants, (1991) 859.

[179] D. Ma, A.D. Stoica, X.L. Wang. Power-law scaling and fractal nature of medium-range order in metallic glasses, Nature Materials 8 (2009) 30-34.

[180] D. Ma, A.D. Stoica, L. Yang, X.L. Wang, Z.P. Lu, J. Neuefeind, M.J. Kramer, J.W. Richardson, T. Proffen. Nearest-neighbor coordination and chemical ordering in multicomponent bulk metallic glasses, Applied Physics Letters 90 (2007) 211908.

[181] R. Maass, D. Klaumunzer, E.I. Preiss, P.M. Derlet, J.F. Loffler. Single shear-band plasticity in a bulk metallic glass at cryogenic temperatures, Scripta Materialia 66 (2012) 231-234.

[182] M.K. Miller, K.F. Russell, K. Thompson, R. Alvis, D.J. Larson. Review of atom probe FIB-Based specimen preparation methods, Microscopy and Microanalysis 13 (2007) 428-436.

[183] M. Tsuchiya, Y. Orai, T. Sato, X. Man, J. Katane, T. Onishi. High-accuracy sample preparation for three dimensional atom probe tomography using orthogonal column layout FIB-SEM and its STEM function, Microscopy and Microanalysis 24 (2018) 830-831.

[184] C.B. Carter, D.B. Williams. Transmission Electron Microscopy: A Textbook for Materials Science, Springer (2009).

[185] L. Reimer, H. Kohl. Transmission Electron Microscopy: Physics of Image Formation, Springer (2008).

[186] W.H. Bragg, W.L. Bragg. The reflection of X-rays by crystals, Proceedings of the Royal Society of London A, Mathematical and Physical Sciences 88 (1913) 428-438.

[187] A. Iida. Synchrotron Radiation X-Ray Fluorescence Spectrometry, Encyclopedia of Analytical Chemistry (2013) 1-23.

[188] R. Fitzgerald. Phase-sensitive x-ray imaging, Physics Today 53 (2000) 23-26.

[189] S.R. Stock. Recent advances in X-ray microtomography applied to materials, International Materials Reviews 53 (2008) 129-181.

[190] S.R. Stock. X-ray microtomography of materials, International Materials Reviews 44 (1999) 141-164.

[191] B.A. Dowd, G.H. Campbell, R.B. Marr, V. Nagarkar, S. Tipnis, L. Axe, D.P. Siddons. Developments in synchrotron x-ray computed microtomography at the National Synchrotron Light Source, Developments in X-Ray Tomography 3772 (1999) 224-236.

[192] Y.X. Wang, F. De Carlo, I. Foster, J. Insley, C. Kesselman, P. Lane, G. von Laszewski, D. Mancini, I. McNulty, M.H. Su, B. Tieman. A quasi-realtime x-ray microtomography system at the Advanced Photon Source, Developments in X-Ray Tomography 3772 (1999) 318-327.

[193] A. Khounsary, P. Kenesei, J. Collins, G. Navrotski, J. Nudell. High energy X-ray micro-tomography for the characterization of thermally fatigued GlidCop specimen, Journal of Physics: Conference Series 425 (2013) 212015.

[194] J.L. Shui, J.S. Okasinski, P. Kenesei, H.A. Dobbs, D. Zhao, J.D. Almer, D.J. Liu. Reversibility of anodic lithium in rechargeable lithium-oxygen batteries, Nature Communications 4 (2013) 2255.

[195] D.J. Larson. Local Electrode Atom Probe Tomography: A User's Guide, Springer (2013).

[196] T.F. Kelly, M.K. Miller. Invited review article: Atom probe tomography, Review of Scientific Instruments 78 (2007).

[197] M.J. Southon. Field emission and field ionization, in: J.J. Hren, S. Ranganathan, Field-Ion Microscopy, Springer (1968), 6-27.

[198] M.K. Miller. Atom probe tomography for studying phase transformations in steels, in: E. Pereloma, D.V. Edmonds, Phase Transformations in Steels, Woodhead Publishing (2012), 532-556.

[199] M.K. Miller, R.G. Forbes. Atom probe tomography, Materials Characterization 60 (2009) 461-469.

[200] C. Liu, R. Maass. Strain-dependent shear-band structure in a Zr-based bulk metallic glass, to be submitted.

[201] P. Tandaiya, U. Ramamurty, R. Narasimhan. Mixed mode (I and II) crack tip fields in bulk metallic glasses, Journal of the Mechanics and Physics of Solids 57 (2009) 1880-1897.

[202] S. Küchemann, C. Liu, E.M. Dufresne, J. Shin, R. Maass. Shear banding leads to accelerated aging dynamics in a metallic glass, Physical Review B 97 (2018).

[203] B.L. Zheng, Y.Z. Zhou, S.N. Mathaudhu, R.Z. Valiev, C.Y.A. Tsao, J.M. Schoenung, E.J. Lavernia. Multiple and extended shear band formation in MgCuGd metallic glass during high-pressure torsion, Scripta Materialia 86 (2014) 24-27.

[204] Y.S. Wang, Z.X. Guo, R. Ma, G.J. Hao, Y. Zhang, J.P. Lin, M.L. Sui. Investigation of the microcrack evolution in a Ti-based bulk metallic glass matrix composite, Progress in Natural Science-Materials International 24 (2014) 121-127.

[205] Y. Zhang, N.A. Stelmashenko, Z.H. Barber, W.H. Wang, J.J. Lewandowski, A.L. Greer. Local temperature rises during mechanical testing of metallic glasses, Journal of Materials Research 22 (2011) 419-427.

[206] M.Q. Jiang, G. Wilde, L.H. Dai. Shear band dilatation in amorphous alloys, Scripta Materialia 127 (2017) 54-57.

[207] A. Dubach, F.H. Dalla Torre, J.F. Löffler. Deformation kinetics in Zr-based bulk metallic glasses and its dependence on temperature and strain-rate sensitivity, Philosophical Magazine Letters 87 (2007) 695-704.

[208] S.X. Song, T.G. Nieh. Flow serration and shear-band viscosity during inhomogeneous deformation of a Zr-based bulk metallic glass, Intermetallics 17 (2009) 762-767.

[209] C.A. Volkert, A. Donohue, F. Spaepen. Effect of sample size on deformation in amorphous metals, Journal of Applied Physics 103 (2008) 083539.

[210] D.C. Jang, J.R. Greer. Transition from a strong-yet-brittle to a stronger-and-ductile state by size reduction of metallic glasses, Nature Materials 9 (2010) 215-219.

[211] S. Mukherjee, J. Schroers, Z. Zhou, W.L. Johnson, W.K. Rhim. Viscosity and specific volume of bulk metallic glass-forming alloys and their correlation with glass forming ability, Acta Materialia 52 (2004) 3689-3695.

[212] X.K. Xi, D.Q. Zhao, M.X. Pan, W.H. Wang, Y. Wu, J.J. Lewandowski. Fracture of brittle metallic glasses: brittleness or plasticity, Physical Review Letters 94 (2005) 125510.

[213] C. Gammer, C. Ophus, T.C. Pekin, J. Eckert, A.M. Minor. Local nanoscale strain mapping of a metallic glass during in situ testing, Applied Physics Letters 112 (2018) 171905.

[214] S. Hilke, H. Rosner, D. Geissler, A. Gebert, M. Peterlechner, G. Wilde. The influence of deformation on the medium-range order of a Zr-based bulk metallic glass characterized by variable resolution fluctuation electron microscopy, Acta Materialia 171 (2019) 275-281.

[215] R. Maass, K. Samwer, W. Arnold, C.A. Volkert. A single shear band in a metallic glass: Local core and wide soft zone, Applied Physics Letters 105 (2014) 171902.

[216] D.D. Alix-Williams, M.L. Falk. Shear band broadening in simulated glasses, Physical Review E 98 (2018).

[217] M. Hassani, A.E. Lagogianni, F. Varnik. Probing the degree of heterogeneity within a shear band of a model glass, Physical Review Letters 123 (2019).

[218] R.T. Qu, S.G. Wang, X.D. Wang, Z.Q. Liu, Z.F. Zhang. Revealing the shear band cracking mechanism in metallic glass by X-ray tomography, Scripta Materialia 133 (2017) 24-28.

[219] P. Murali, T.F. Guo, Y.W. Zhang, R. Narasimhan, Y. Li, H.J. Gao. Atomic scale fluctuations govern brittle fracture and cavitation behavior in metallic glasses, Physical Review Letters 107 (2011) 215501.

[220] H.C. Peng, Z.C. Ruan, F.H. Long, J.H. Simpson, E.W. Myers. V3D enables real-time 3D visualization and quantitative analysis of large-scale biological image data sets, Nature Biotechnology 28 (2010) 348-U375.

[221] P. Guan, S. Lu, M.J. Spector, P.K. Valavala, M.L. Falk. Cavitation in amorphous solids, Physical Review Letters 110 (2013) 185502.

[222] C.H. Rycroft, E. Bouchbinder. Fracture toughness of metallic glasses: annealing-induced embrittlement, Physical Review Letters 109 (2012) 194301.

[223] E.Z. Wang, N.G. Shrive. Brittle-fracture in compression: mechanisms, models and criteria, Engineering Fracture Mechanics 52 (1995) 1107-1126.

[224] S.J. Wu, X.D. Wang, R.T. Qu, Z.W. Zhu, Z.Q. Liu, H.F. Zhang, Z.F. Zhang. Gradual shear band cracking and apparent softening of metallic glass under low temperature compression, Intermetallics 87 (2017) 45-54.

[225] J.Y. Suh, R.D. Conner, C.P. Kim, M.D. Demetriou, W.L. Johnson. Correlation between fracture surface morphology and toughness in Zr-based bulk metallic glasses, Journal of Materials Research 25 (2010) 982-990.

[226] E. Bouchaud, D. Boivin, J.L. Pouchou, D. Bonamy, B. Poon, G. Ravichandran. Fracture through cavitation in a metallic glass, Epl 83 (2008).

[227] J.G. Wang, Y.C. Hu, P.F. Guan, K.K. Song, L. Wang, G. Wang, Y. Pan, B. Sarac, J. Eckert. Hardening of shear band in metallic glass, Scientific Reports 7 (2017) 7076.

[228] W.F. Wu, Y. Li, C.A. Schuh. Strength, plasticity and brittleness of bulk metallic glasses under compression: statistical and geometric effects, Philosophical Magazine 88 (2008) 71-89.

[229] K. Mondal, K. Hono. Geometry constrained plasticity of bulk metallic glass, Materials Transactions 50 (2009) 152-157.

[230] I. Singh, R. Narasimhan. Notch sensitivity in nanoscale metallic glass specimens: Insights from continuum simulations, Journal of the Mechanics and Physics of Solids 86 (2016) 53-69.

[231] S.C. Lim, M.F. Ashby, J.H. Brunton. The effects of sliding conditions on the dry friction of metals, Acta Metallurgica 37 (1989) 767-772.

[232] A. Vinogradov. On shear band velocity and the detectability of acoustic emission in metallic glasses, Scripta Materialia 63 (2010) 89-92.

[233] A.Y. Vinogradov, V.A. Khonik. Kinetics of shear banding in a bulk metallic glass monitored by acoustic emission measurements, Philosophical Magazine 84 (2004) 2147-2166.

[234] A. Lazarev, A. Vinogradov, S. Hashimoto. Comparative analysis of inhomogeneous plastic flow in bulk and ribbon metallic glasses monitored by acoustic emission, Journal of Alloys and Compounds 504 (2010) S60-S64.

APPENDIX A: CALCULATION OF CONTRAST THICKNESS

The contrast thickness (x_k), which is defined with Equation 2.6 in Section 2.2.1 as $\frac{1}{x_k} = \frac{4}{Zx_{el}}\left[\frac{Z-1}{4\left[1+\left(\frac{\alpha_0}{\theta_0}\right)^2\right]} + ln\sqrt{1+\left(\frac{\theta_0}{\alpha_0}\right)^2}\right]$, is calculated using the constants listed in Table A.1, where Z is the average atomic number of the probed Vit105 MG, x_{el} is the elastic contrast thickness, θ_0 is the characteristic angle of the scattered electrons (electron trajectory change due to elastic interaction with the nucleus), and α_0 is the minimum scattering angle for the inner ring of the HAADF detector at a given camera length. The values of x_{el} and θ_0 for the 200 keV imaging condition are interpolated from the Ge data listed in Table A.2, which is adapted from Table 6.1 in Reference [185], because the Z value for Vit105 MG is very close to that of Ge. The value of α_0 depends on the specific TEM and camera length when the HAADF-STEM images are taken. In this case, a JEOL 2010F TEM with a 15 cm camera length is used. The calculated value of x_k is thus 650 μg/cm^2.

Table A.1. The constants used for the calculation of the contrast thickness.

Z	x_{el} (μg/cm^2)	θ_0 (mrad)	α_0 (mrad)
32.68	32.7	21.9	100

Table A.2. The elastic contrast thickness values and characteristic angle of the scattered electrons, adapted from Table 6.1 in Reference [185].

E (keV)	x_{el} (μg/cm^2)	θ_0 (mrad)
150	28.0	23.4
300	42.0	19.0

APPENDIX B: EXAMPLE HAADF-STEM IMAGE ANALYSIS CODE

The shear-band thickness and density change data presented in Section 3.1 and 3.3 were extracted from HAADF-STEM images using MATLAB. An example MATLAB script is presented with the commented code as follows:

```
%% Load image as m by n matrix (gray-scale image):

[A, map] = imread('3_probe7_15cm_tilt0_rot45.tif'); % load image
nmperpixel =2410/2048; % define nm per pixel according to image
shear_offset = 1230; % nm, defined for bending bar samples with measurable surface offset
minwidth = 0; % minimum shear-band thickness
maxwidth =100; % maximum shear-band thickness in the image measured in ImageJ (any thickness values above this will be removed)
imshow(A, [min(A(:)), max(A(:))]) % opens image in MATLAB


%% Shear-band thickness and density change data extraction along the shear-band path using a for loop:

t = [60:0.5:70]'; % defines a segment to analyze in the image

for n = 1:length(t)
t(n)

% Define a box that includes the shear band and the surrounding matrix:

yposmin = round(2048/80)*t(n);
yposmax = yposmin + round(2048/10); % height of box (rows) in pixels
yposition(n) = ((yposmax-yposmin)/2 +yposmin)* nmperpixel;
xposmin = 800;
xposmax = 1100; % width of box (columns) in pixels
imshow(A,[min(A(:)),max(A(:))])
hold on
rectangle('position', [xposmin yposmin xposmax-xposmin yposmax-yposmin]) % plots the defined box
saveas(gcf,
strcat('C:\Users\CLiu\Vit105_3pt_bending_bar\Lamella_J_tensile\3_tilt0_newcode\graph\Picture',num2str(n),'.png')) % saves the box position
hold off

% Analyze the intensity profile from each box:
```

```
x = 1:numel(box); % defines number of pixels (or number of columns) in the box, later translated to unit of nm
y = mean(A(yposmin:yposmax,xposmin:xposmax)); % list of average intensity value for each x position
p = polyfit(x,y,1); % linear fit of the sloped intensity profile, where the first value p(1) is the slope
y = y-x*p(1); % shift the sloped intensity curve horizontally and produces new y

% The following 4 parameters need testing for each HAADF-STEM image and may change slightly to give reasonable results. Change according to the generated graphs below.

sp = 0.1; % smooth parameter for ys = smooth(y, sp, 'lowess')
c1 = 1; % top-down restriction for finding average maximum intensity
c1min = 1; %top-down restriction for finding average minimum intensity
c2 = 3; % left-right restriction for finding FWHM

ys=smooth(y, sp, 'lowess'); % smooth data (sp is smooth parameter)

% To find shear-band thickness:

ymax = max(ys);
ymin = min(ys);
ymax = mean(ys(find(ys<=ymax+c1 & ys>=ymax-c1))); % average max intensity
ymin = mean(ys(find(ys<=ymin+c1min & ys>=ymin-c1min))); % average min intensity

yfwhm =(ymax-ymin)/2+ymin; % intensity at FWHM

sizex=size(x);
sizex=sizex(2);

plot(x*nmperpixel, y,'x',x*nmperpixel, ys,'r*', x*nmperpixel,yfwhm*ones(1,sizex), 'b-', x*nmperpixel, ymax*ones(1,sizex), 'c-', x*nmperpixel, ymin*ones(1,sizex), 'm-');
legend('Raw Data', 'Smoothed Data', 'Intensity at FWHM', 'Average Maximum Intensity', 'Average Minimum Intensity')
xlabel('X Position (nm)')
ylabel('Intensity (counts)')
saveas(gcf,strcat('C:\Users\CLiu\Vit105_3pt_bending_bar\Lamella_J_tensile\3_tilt0_newcode\graph\box',num2str(n),'.png')) % plots and saves the raw intensity profile data, the smoothed profile, and the average max, average min, and FWHM intensity values for visualization and setting the above 4 parameters

r = find(ys<=yfwhm+c2 & ys>=yfwhm-c2);
rleft = r(r< mean(r));
rright= r(r> mean(r));
fwhm = mean(rright)-mean(rleft); % finds the FWHM in pixels
width(n) = nmperpixel * fwhm; % shear-band thickness in nm
```

```
ewidth(n) = ((max(rleft) - min(rleft)) + (max(rright) - min(rright)))/2 * nmperpixel; % shear-band thickness error

% To find shear-band density change with respect to the matrix:

Isb = ymin;
Imatrix = ymax;
ddensity(n) = ((Isb/Imatrix) - 1)*100; % percent change in density
eddensity(n) = (abs(ddensity(n)) * (((min(ys) - min(y))/Isb)^2 + ((max(ys)-max(y))/Imatrix)^2)^0.5); % density change error


% Remove outlier data for shear-band thickness:

if any(width < maxwidth & width > minwidth)
   width_real_index=find(width < maxwidth & width > minwidth);
end

width = width(width_real_index);
ddensity = ddensity(width_real_index);
yposition = yposition(width_real_index);
ewidth = ewidth(width_real_index);
eddensity = eddensity(width_real_index);

% Shear strain calculation:

shear_strain = shear_offset./width;
shear_strain_error=shear_strain.*((ewidth./width).^2+(10./shear_offset).^2).^.5;


% Plot double-y-axis graph of ddensity and width along shear band:

fig = figure;
[AX,H1,H2] = plotyy(yposition, width, yposition,ddensity);
set(fig, 'CurrentAxes', AX(1));
set(gca,'FontSize',15,'FontWeight','bold')
xlabel('Position along Shear Band (nm)','FontSize',15,'FontWeight','bold')
ylabel(AX(1),'Shear Band Width (nm)','FontSize',15,'FontWeight','bold')
hold on;
scatter(AX(1),yposition,width,80,'bo')
errorbar(yposition, width, ewidth, 'b.');
set(fig, 'CurrentAxes', AX(2));
set(gca,'FontSize',15,'FontWeight','bold')
ylabel(AX(2),'Density Change (%)','FontSize',15,'FontWeight','bold')
hold on;
scatter(AX(2),yposition,ddensity,80,'rd')
```

```
set(H2,'markers',12)
errorbar(yposition, ddensity, eddensity, 'r.');
set(H1,'LineStyle',':','Linewidth',1)
set(H2,'LineStyle','-.','Linewidth',1)
legend([H1;H2],'Width (nm)','Density Change (%)');
print('C:\Users\CLiu\Vit105_3pt_bending_bar\Lamella_J_tensile\3_tilt0_newcode\graph\ddensit
ywidth','-dpng')
close

% Plot density change vs width:

plot(width,ddensity,'ro','markers',12)
set(gca,'FontSize',15,'FontWeight','bold')
xlabel('Shear Band Width (nm)','FontSize',20,'FontWeight','bold')
ylabel('Density Change (%)','FontSize',20,'FontWeight','bold')
hold on
% errorbar(width,ddensity,eddensity,'.k')
% herrorbar(width,ddensity,ewidth,'.k')
print('C:\Users\CLiu\Vit105_3pt_bending_bar\Lamella_J_tensile\3_tilt0_newcode\graph\wd','-
dpng')
hold off

% Export data into Excel:

T = table;
T.YPosition = yposition';
T.DensityChange = ddensity';
T.ErrorDensityChange = eddensity';
T.Width = width';
T.ErrorWidth = ewidth';
T.ShearStrain = shear_strain';
T.ErrorShearStrain = shear_strain_error';

writetable(T,'C:\Users\CLiu\Vit105_3pt_bending_bar\Lamella_J_tensile\3_tilt0_newcode\graph\
data.xlsx');

end
```

APPENDIX C: UNUSED X-RAY TRANSMISSION AND DIFFRACTION DATA

It is mentioned in Section 3.2.1 that, besides the NB-XRF data collected at Beamline 26-ID at the APS, the transmitted signal and the diffraction pattern through the shear-band-containing TEM specimen were also collected simultaneously for each pixel of the scanned area shown in Figure 3.8. However, the transmitted signal and the diffraction patterns are not presented in Section 3.2.1 due to the low signal-to-noise ratio. This appendix section records the analysis procedure of the two unused datasets.

The transmitted beam intensity should be different for different material density values after normalizing by the incoming beam intensity. Figure C.1a shows the Ni fluorescence map before drift correction (the drift-corrected Ni map is shown in Figure 3.10a), where the dark curve indicates the shear band, and Figure C.1b shows the transmitted intensity map for the same pixels (i.e., same scanned area) as in Figure C.1a. Since the TEM specimen used for this experiment is ~100 nm thin, the signal-to-noise ratio of the transmitted beam intensity is probably too low to distinguish the lower-density shear-band region from the higher-density matrix material. Thus the location of the shear band is not clear in Figure C.1b. Another way to detect the shear band using the transmitted data is by finding the boundary between the shear band and the matrix. The transmitted beam at the boundary will shift its center of mass (centroid) in either the x-direction or the y-direction due to the change in electron density from the matrix to the shear band. For each pixel of the scanned area, the center of mass in the x-direction ($d_{Centroid-X}$) is defined as the total moments in the x-direction divided by the total mass, where mass is equivalent to the intensity, as shown in Equation C.1:

$$d_{Centroid-X} = \frac{\sum_1^n d_i I_i}{\sum_1^n I_i}, \tag{C.1}$$

where d_i is the position in the x-direction, n is total number of data points in the x-direction, and I_i is the average intensity in the y-direction. Centroid Y is defined similarly but in the y-direction, which is less useful in this experiment because the scans were conducted horizontally in the x-direction across a relatively vertical shear band. After obtaining the Centroid-X and Centroid-Y values for each pixel of the scanned area, the Centroid-X and Centroid-Y maps are shown in Figures C.1c-d. Note that all of the data in Figures C.1a-d have been normalized by the incoming beam intensity (i.e., ion chamber count). The Ni XRF map in Figure C.1a shows a visible shear band, so it is drift corrected and further discussed in Section 3.2.1. The X-ray transmission maps in Figures C.1b-d are too noisy to generate useful conclusions and are thus not processed further.

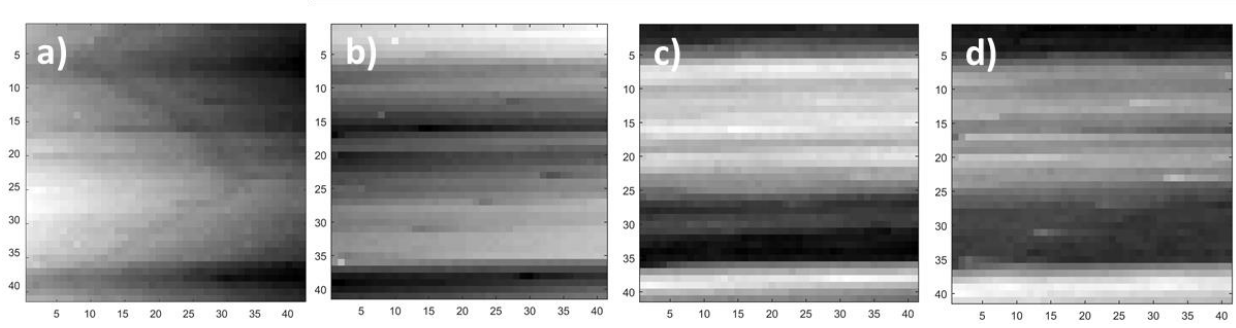

Figure C.1. a) NB-XRF map for Ni without drift correction, showing depletion of Ni in the shear band. b) Transmitted X-ray intensity map of the same scanned area shown in a). c) and d) are the Centroid-X and Centroid-Y maps, respectively, of the same scanned area shown in a). The numbers on the x-axis and y-axis are pixel numbers.

Additionally, X-ray diffraction patterns were recorded for each pixel of the scanned area shown in Figure C.1a with the purpose of finding the difference of q_1 values between the shear band and the matrix, as discussed in Section 3.2.2. Due to the setup geometry constraint, only a portion of the entire diffraction ring could be collected, with an example shown in Figure C.2a, where the high-intensity amorphous ring is from the Vit105 MG sample and the other faint rings are from polycrystalline metals contributed by other parts of the setup. The diffraction patterns were recorded with a q-range from 1.7 $Å^{-1}$ to 3.7 $Å^{-1}$ to include the q_1 value of 2.6 $Å^{-1}$ for the

Vit105 MG. After subtracting the background, the q_1 peak of each pixel was fit by an asymmetric Pearson fit function to find the peak value, and the fit q_1 peak values are plotted in Figure C.2b. Since only a small portion of the entire diffraction ring was used to find the q_1 peak, the peak values may not be accurate. Therefore, the q_1 map in Figure C.2b does not show any distinguishable difference between the shear band and the matrix. This set of diffraction data is not presented in the main text. Instead, SEND was used to successfully detect the q_1 peak difference between the shear band and the matrix, as discussed in Section 3.2.2.

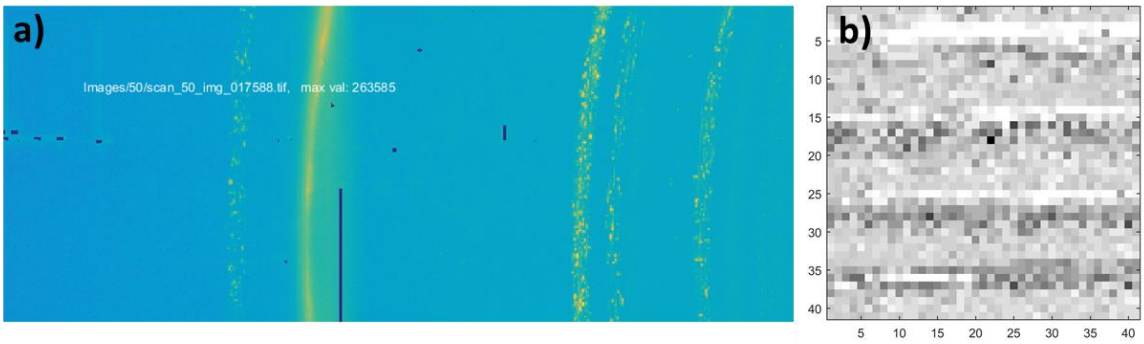

Figure C.2. a) Representative diffraction pattern of a pixel in the scanned area shown in Figure 3.8. b) Map of q_1 peak values for the scanned area, showing the same pixel locations as those in Figure C.1.